In Search Of Binary Wolf-Rayet Central Stars Of Planetary Nebulae

Rajeev Manick

30^{th} of Oct. 2013

A project submitted in partial fulfilment of the requirements for the degree M.Sc. in the Department of Astronomy, as part of the National Astrophysics and Space Science Programme
UNIVERSITY OF CAPE TOWN

Supervisor: Dr. Brent Miszalski
Co-supervisor: Dr. Vanessa McBride

Abstract

Planetary Nebulae (PNe) are circumstellar gas envelopes ejected during Asymptotic Giant Branch (AGB) phase of the stars between $1M_{\odot}$ to $8M_{\odot}$. In around 3000 galactic PNe, 10 to 20 % are known to host a Wolf-Rayet type central star ([WR] CSPN). These [WR] CSPNe are known to be very hydrogen deficient (H-deficient), the mechanism behind which is not clearly understood. A binary central star (CS) or a merger scenario is very likely to be responsible for the H-deficiency. As an attempt to investigate the former, a radial velocity (RV) monitoring program of 7 [WR] CSPNe was conducted, which is the first systematic study of its kind. Spectroscopic observations were made at the SAAO 1.9m Telescope over 3 separate weeks in May 2012, June 2012 and July 2013. The spectra were reduced and analyzed with a cross-correlation method to determine RV shifts in the stellar and nebular lines. Together with a review of the major mechanisms involved in the formation and evolution [WR] CSPNe, the main results obtained in this work are discussed. An offset is found between the mean stellar and nebular lines, which might be due to the fact that most of the stellar emission lines are formed in the wind and are likely to be blue-shifted as in several Of-type central stars. No significant amplitude or periodic variations are seen in the stellar lines, as we would expect from a close binary system. However, small ($\sim 10-30$ km s^{-1}) stellar RV variations are seen and these are most likely due to wind variability. A χ^2 probability test reveals that the objects are only $30 - 40$ % variable and this variability is not high enough to be attributed to a binary CS. The main conclusions drawn are that these [WR] CSPNe might contain wide binaries with longer periods that would produce RV variations below our detection limit. Another feasible explanation might be that [WR] CSPNe are actually the result of post-CE mergers. We absolutely need RV monitoring using high resolution spectra (e.g. High Resolution Spectrograph on the South African Large Telescope) in the future to confirm the presented results.

Acknowledgements

I would like to extend the deepest appreciation to the National Research Foundation (NRF), Square Kilometre Array (SKA) for their financial support. Thanks to National Astrophysics and Space Science Programme (NASSP) for giving me the opportunity to pursue my studies in Astrophysics. Thanks to University of Cape Town and especially South African Astronomical Observatory for all the help including a placement for me to work and all other services they provided throughout my project.

A big thanks to my Supervisor Dr. Brent Miszalski who has shown the attitude and substance of a genius: he made sure that I understand all the steps in constructing a scientific echelon (from collecting observational data to analyzing and producing publishable results). He is undoubtedly the type of supervisor I would recommend any student. Thanks to my co-supervisor Dr. Vanessa McBride for providing me with corrections and very helpful comments.

I am grateful to the many people who have helped directly or indirectly throughout my thesis. This includes Fred Marang and Francois Van Wyk for brief assistance in my observing runs. My family who have always been there for me and providing me the support I needed. My friends, especially Savishna Pillai, Krishna Sungkur, Kavir Daya, Ulasini Pillay and Meheshree Pillay for their moral supports after an incident which is strongly linked to my Thesis. Without forgetting the Whatsapp groups Children of Milky Way and Sai Is My Power, which contributed a lot in keeping me away from daily stress! I will always be very grateful to Sulona Kandhai, for lending me her laptop lately for final corrections.

Thanks to Prof. Noam Soker and Dr. Orsola De Marco for their prompt answers to questions regarding my thesis.

Finally, a special thanks goes to Dr. Danielle Lucero for her help in proof reading my thesis.

Plagiarism Declaration

I, Rajeev Manick, know the meaning of plagiarism and declare that all of the work in the document, save for that which is properly acknowledged, is my own.

Contents

List of Figures

List of Tables

Chapter 1

Introduction

1.1 Evolution of AGB stars

Planetary nebulae (PNe) are circumstellar gas envelopes ejected during Asymptotic Giant Branch (AGB) phase of the stars between $1M_{\odot}$ to $8M_{\odot}$ (Fig. 1.1).

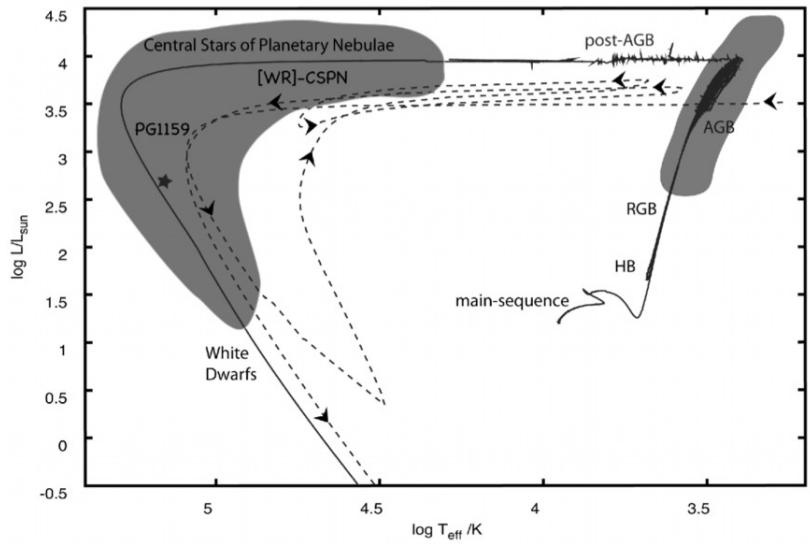

Figure 1.1: *Solid line*: Evolutionary track of a $2M_{\odot}$ star. It begins from a main sequence star, through the red giant branch (RGB) and then AGB to PN and ending as a white dwarf. *Dashed line*: A born again evolution of a star of the same mass which loops in a region of the HR diagram and is discussed later in section 1.4.4 (Figure reproduced from Werner & Herwig (2006)).

Prior to the AGB phase, low and intermediate-mass stars follow the evolutionary track shown by the solid line in the Hertzsprung-Russell diagram (HRD) in Fig. 1.1. Herwig (2005) reviewed the evolution of such a star. It is good to note that single star evolution is being referred here and that close binary interactions (i.e. common-envelope evolution) will be discussed in section 1.5.4.

The evolution starts after the star formation and the pre-main sequence evolution with the core H-burning phase. Nuclear energy release stops when all the H is burned into Helium (He) in the core and the latter resumes gravitational contraction. The He-core is now surrounded by a H burning shell and in the HRD, the star evolves quickly to the base of the RGB phase. The core contraction continues, the envelope of the giant star expands and there is increase in luminosity of the H-shell. The star then goes up to the RGB, it is cool and the envelope is convectively unstable. The ignition of core He burning is dependent on the initial mass. If the initial mass is less than $\sim 1.8\ M_{\odot}$, the He core becomes electron-degenerate when the star reaches the tip of the RGB. Otherwise, more-massive stars ignite He burning in the core and continue their evolution along the horizontal branch. A Carbon-Oxygen (CO) core is left behind, surrounded by both a He and H-burning shell. During the early AGB phase, nuclear production is dominated by the He shell, which burns outwards and reaches the H shell. The evolution then continues up the AGB with thermal pulses during the late AGB phase. There is an increase in mass loss which results into envelope ejection. The ejected atmosphere is ionized by the remnant core which is now a central star of a PN and eventually, producing the PN. In its final evolutionary stage, the star becomes a white dwarf.

1.2 Massive Wolf Rayet (WR) stars

At much greater masses, stars in the late stages of their evolution pass through the WR stage. Fig. 1.2 shows how stars of different masses evolve. High mass stars ($\sim 60.0\ M_{\odot}$) start from the main sequence evolve all the way through the Blue Super Giant (BSG)/Luminous Blue Variable (LBV) phase until they reach the WR phase, ending up as a Supernova.

Wolf-Rayet (WR) stars are mostly characterized by their strong, broad emission line features due to their powerful stellar winds (see Crowther 2007 for a thorough review). WR stars mostly come in two genres (the subtypes) namely the WN subtype, which contain strong He and N lines and the WC subtype, which have strong He, C and O emission lines in their spectra (Fig. 1.3) . Typical WR stars have very high masses of 10 to 25 $M_{\odot}$ and are descendants of O-type stars, but can reach up to 80 $M_{\odot}$ or even more for H-rich WN stars. Figer (2005) and Moffat (2008) reports an apparent stellar mass limit of $\sim 150\ M_{\odot}$ and stars of masses beyond that limit are thought to be binaries or mergers of lower mass stars. Nevertheless, a recent discussion by Crowther (2013) re-poses the question whether there is an upper mass limit for the very massive stars. The models predict that R136 (HD 38268), the central object of the 30 Doradus nebula, has a lower mass limit of $\sim 320\ M_{\odot}$.

WR stars are known for their very high mass loss rates. In the Milky Way, spectroscopically derived mass-loss rates of WN and WC subtypes stars are $10^{-5.6}$ to $10^{-4.4}\ M_{\odot}\ \mathrm{yr}^{-1}$ and $10^{-5.0}$ to $10^{-4.4}\ M_{\odot}\ \mathrm{yr}^{-1}$ respectively (Herald et al. 2001, Barniske et al. 2006).

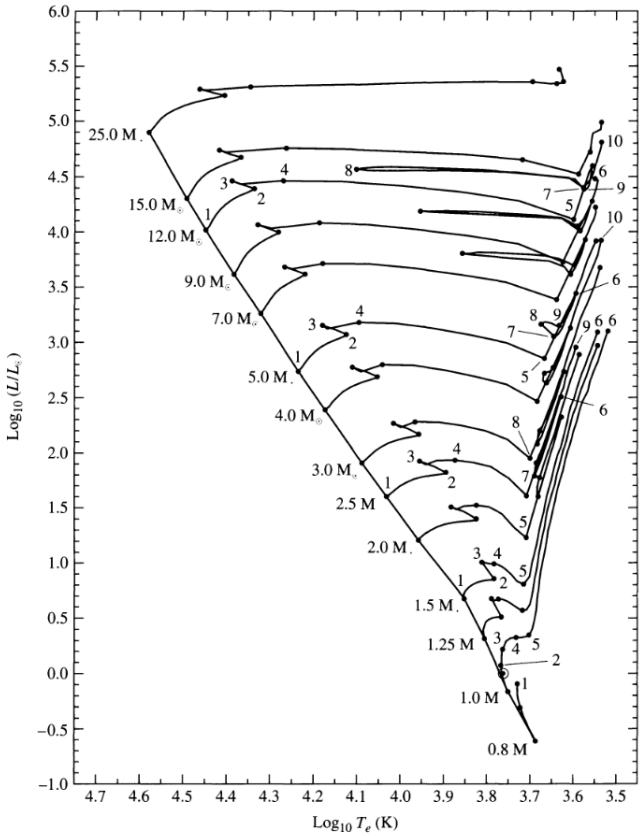

Figure 1.2: The difference between the evolution of a low, intermediate and high mass star in an HR diagram. Figure from Carroll & Ostlie (2006).

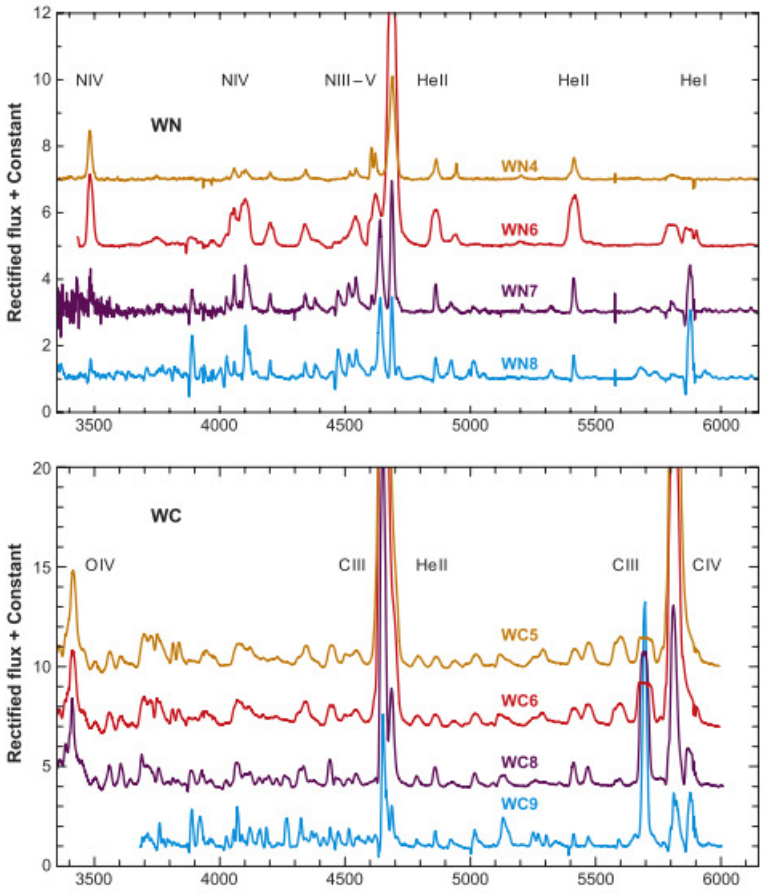

Figure 1.3: Representative spectra of WN and WC type Wolf-Rayet stars. (Crowther 2007)

1.2.1 Spectral properties and classification

The classification of WR stars is based on their emission line strength and line ratios (Smith 1968). WN types are classified by the line ratios of NIII-V and HeI-II. The early WN types (WNE) are the ones ranging from WN2 to WN5 (Smith et al. 1996) and the late WN types (WNL) lie in the WN7 to WN9 range (WN6 can either be early or late type). Smith, Crowther, & Prinja (1994) extended the WN sequence to very late WN types, introducing the new WN10 and WN11 types, in order to replace a group of emission line stars which were originally classified as Ofpe/WN9 (Bohannan & Walborn 1989). Crowther & Walborn (2011) give an updated classification of O If*/WN5-7 stars. Crowther & Walborn (2011) propose that the difference between O2-3.5 If*, O2-3.5 If*/WN5-7 and WN5-7 stars may be distinguished by the morphology of the Hβ line which is purely in absorption for O2-3.5 If* stars, P Cygni for O2-3.5 If*/WN5-7 stars and purely emission for WN types.

On the other hand, the WC types are classified by the emission-line equivalent width ratios (see e.g. Figure 6 of Crowther et al. (1998b)). See Crowther et al. (1998b) for a description of the classification scheme of the WC types. For late type WC Crowther et al. (1998b) used logarithm of equivalent width ratios of the lines CIV $\lambda\lambda$5801-12/CIII λ5696. The subclasses WO1-4 are also defined by looking at the line ratio of OVI $\lambda\lambda$3811-34/OV λ5590 (Fig. 1.4).

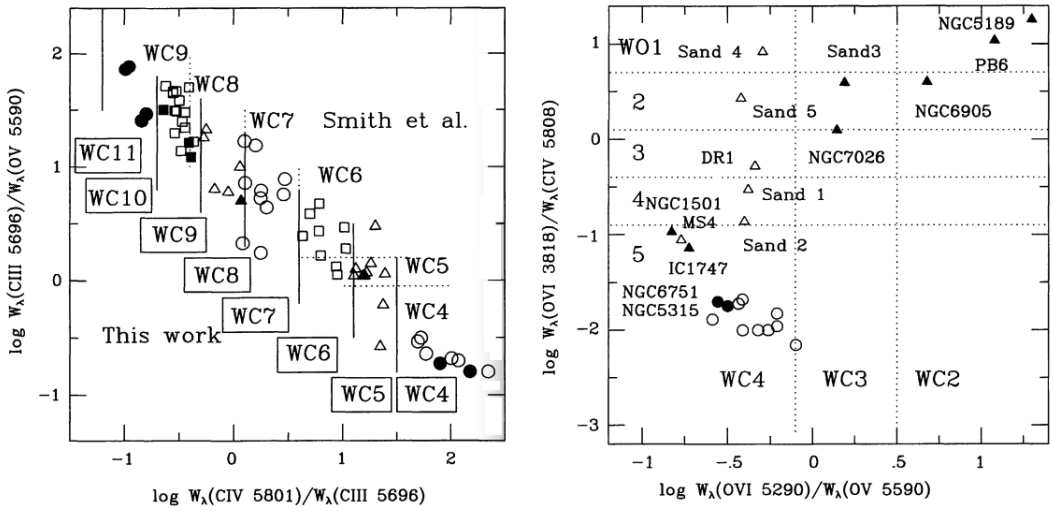

Figure 1.4: Classification of WCL and WCE types based on equivalent widths (W_λ) (Crowther et al. 1998b).

The WC subtypes span through the range of WC4 to WC9, WC4 to WC6 being the early types (WCE) and the rest WCL types (for late WC types). In addition to this, the WCE sequence has been extended to include the rare O-rich WO stars. These stars exhibit strong OVI emission line (Kingsburgh, Barlow, & Storey 1995). The WO sequence is divided into four subtypes, the WO1 to WO4, depending on the relative strength of OV, OVI and CIV emission lines (Crowther et al. 1998b).

Lastly, there are a small number of WN stars which have spectral features in which CIV emission lines are unusually strong and these constitute an intermediate WN/C classification (Conti & Massey 1989). These WN/C types are believed to be in transition phase between the WN and WC stages.

1.2.2 Wind properties and mass loss rates

The wind velocities are measured accurately by the wavelength of the blue edge of the P-Cygni absorption profile in the spectra of WR stars (Prinja et al. 1990a;b). The wind velocities can also be deduced by fitting a CMFGEN (Hillier & Miller 1998) Non-Local Thermodynamic Equilibrium (NLTE) to the spectral lines to model the atmosphere. The model solves the radiative transfer equation in the co-moving frame and assumes an expanding, spherically symmetric, homogeneous atmosphere, allowing for metal-line blanketing and wind clumping.

Observations show that later types WR stars have lower wind velocities than the early types and in some cases, the velocities can be a factor of up to even 10 times lower (Herald et al. 2001, Barniske et al. 2006, Crowther et al. 2002). The fastest wind velocity known is in the star WR93b (v_∞ = 6000 km s^{-1}) which is a galactic WO type star (Drew et al. 2004). Observations also show a decrease in line width and hence wind velocity for stars of progressively lower metallicity, by a factor of up to even two between the galactic and IC1613 WR stars (Crowther & Hadfield 2006).

Wolf-Rayet mass-loss rates are surprisingly uniform across spectral type. All the observed spectral types have an average mass-loss rate of $\dot{M} = 10^{-5}$ M$_\odot$ yr^{-1}, except for WC9 stars, which have $\dot{M}$ lower by at least a factor of 2. Both radio flux observations by Leitherer et al. (1997) and optical observations by Hamann et al. (1995), Koesterke & Hamann (1995) of mass-loss rates for WN and WC stars, are in good agreement with each other (Fig. 1.5).

Referring to Figure 1.5, WC9 sequence stars do not seem to follow the general trend in mass loss rate. One of the reasons might be that WC9 stars differ from other subtypes due to their high amount of heated circumstellar dust (Williams 1995).

Another result of stellar wind bubbles is a ring nebula around most WN types. These rings are believed to be material ejected during the Red Super Giant (RSG) or Luminous Blue Variable (LBV) phases that is photo-ionized by the WR central star (Crowther 2007). These occur in relatively young WR types which are the WN types. Rings in that sense, provide evolutionary links between WR stars and their precursors (RSG and LBV). Thus, ring nebulae are very useful in providing information about their precursors. The first known examples are NGC 2359 and NGC 6888 (Chu et al. 1983, Dopita et al. 1994, Stock & Barlow 2010).

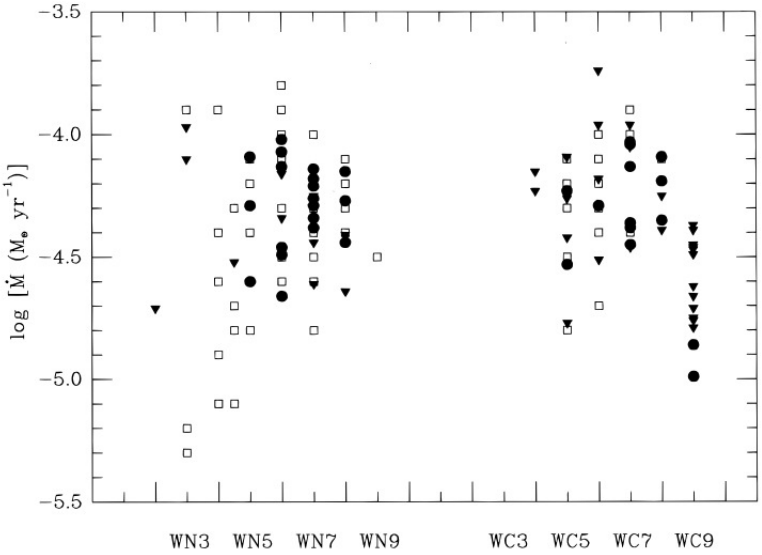

Figure 1.5: Comparison between mass-loss rates derived from radio fluxes and from optical recombination lines. The filled circles and triangles denote mass-loss rates from combined ATCA and VLA data. Open squares denote mass-loss rates determined from optical recombination lines by Hamann et al. (1995) for WN stars and by Koesterke & Hamann (1995) for WC stars (Leitherer et al. 1997).

1.3 WR stars in binaries

1.3.1 Colliding winds

Two early-type stars comprising of either WR or OB stars, in a binary system can produce a wind-wind interaction scenario (colliding wind binaries). The physics underlying colliding winds was reviewed by Stevens et al. (1992). Eichler & Usov (1993) reviewed the production of non-thermal (synchrotron) radio emission from early-type stars like WR and OB binaries. The region where the stellar winds collide in these WR binaries may be a strong source of non-thermal radio emission, whereas, thermal radio emission may be produced via free-free emission from their stellar wind. The presence of magnetic fields in the winds of these stars is known to play an important role for accelerating electrons up to relativistic speeds, which in turn produces synchrotron emission. The detection of non-thermal radio emission depends on the orbital period of these binaries. One example is WR140, a binary system with a 7.9-year orbital period. The radio flux is thermal for the majority of the orbit, but for phases between 0.55 and 0.95 (where phase 0 is at periastron), the radio flux becomes non-thermal (Williams et al. 1990a)

1.3.2 Using polarization to detect binaries

Colliding wind binaries might obscure binary detection via radial velocity monitoring methods. In that case, another tool which can be used to access the windy binaries is polarimetric observations. The partial alignment of dust grains in the interstellar medium can produce

linear polarization. Intrinsic variability in linear polarization might occur due to different mechanisms which include non-radial pulsations, rotation of spots or other inhomogeneities in the wind, blob ejection in the wind and/or modulation by binary motion (St.-Louis et al. 1987). Polarization is also produced by Thomson scattering (Billings 1966), i.e. light from the companion is scattered by free electrons in the wind. In the case of a binary system, the geometry of the system and more particularly the inclination of the orbit can be derived from the polarization (Rudy & Kemp 1976, Rudy 1977, Moffat & Piirola 1993, St-Louis 2013).

1.3.3 Formation of Dust

Binarity appears to play a key role in the formation of dust around massive stars, more specifically, WC types, provided that the correct density within the shock region is reached (Crowther 2007). Observations show episodical dust formation in WR 140 at its periastron passage, when the colliding winds reach their highest power (Williams et al. 1990b).

Usov (1991) provided arguments that the wind conditions of WR 140 at periastron favours a strong gas compression near the shock surface, providing a cold-gas outflow. Thus, a very plausible explanation is a colliding wind binary, in which dust forms in a high density, low-temperature, Carbon-rich (C-rich) environment such as a bow-shock. Another example is WR 104 (Fig. 1.6) which has a dust shell of radius 3000 $R_\star$ to 300000 $R_\star$ (Crowther 1997) and later proved to be a binary system by Tuthill, Monnier, & Danchi (1999). It is currently believed that most if not all dust-forming WC stars are actually in binary systems (Crowther 2007).

1.4 Wolf-Rayet Central Stars of Planetary Nebulae ([WR] CSPNe)

In around 1500* true or probable PN listed by Acker et al. (1992a;b), Acker & Ochsenbein (1993), those having a Wolf-Rayet central star represent around 6-10% (Gorny & Stasińska 1995). According to Depew et al. (2011), around $\sim 10-20\%$ of central stars of planetary nebulae are currently known to mimic the massive WR stars mentioned in Section 1.2. However, it should be noted that surveys up till now are quite incomplete and biased and only a small fraction of CSPNe have been studied spectroscopically.

These CSPNe are considered as the low-mass equivalents of the massive WR stars (see Crowther 2008) and are bracketed as [WC] and [WN], to differentiate them from the massive ones (van der Hucht et al. 1981). They evolve from low and intermediate mass main sequence stars instead of the massive O-stars. Spectroscopically, the [WR] closely resemble the massive WR stars (Fig. 1.7 and 1.8).

*The number of galactic PNe is much larger; an upper limit of $\sim$ 2850 (Miszalski et al. 2012a).

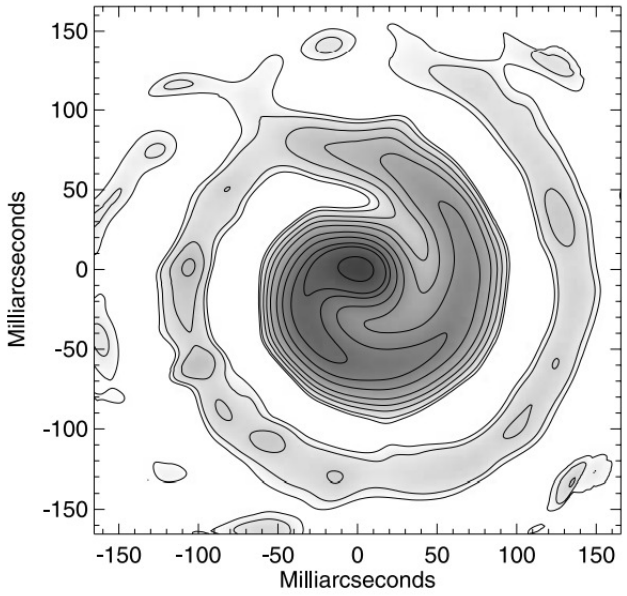

Figure 1.6: Stacked composite images of WR 104 (The pinwheel) with radio contour levels of 0.1%, 0.2%, 0.5%, 1%, 2%, 5%, 10%, 20%, 30% and 70% of the peak. Winds from the binary WR central stars collide and as they orbit each other, the winds are driven outwards producing this pinwheel shape (Tuthill et al. 2008).

1.4.1 Distribution of [WC] CSPNe

Most of the [WC] CSPNe are distributed among early [WC] (often written [WCE]) and late [WC] ([WCL]) types. The cooler late-types evolve much more like post-AGB stars and eventually evolve into the hotter early types after an intense mass-loss process (Acker et al. 1996). Only a handful of [WC] types are found to be in the intermediate [WC5-8] phase. One possible explanation might be that the transition of the [WC] types in this intermediate phase is fast. Figure 1.9 shows the galactic disk, Large Magellanic Cloud (LMC) and Small Magellanic Cloud (SMC) distribution of the [WC] types as compared to the massive WC ones.

Seemingly, due to selection effects, the number of [WC] types detected in the bulge is less as compared to those found in the disk. Firstly, in the bulge, one would expect to detect fewer stars because of high extinction and crowding. Also, PNe in the bulge are smaller in angular size and a large fraction of their nebular fluxes (L(H_β)) are present in their spectra. This makes the detection of a [WR] type CS possible only for objects having a V band luminosity (L_V) of the star sufficiently large with respect to the total nebular flux. On the other hand, many PNe in the galactic disk tend to be closer to us relative to the ones in the bulge and thus having larger angular sizes. A model by Górny et al. (2004) shows that only a small fraction of the total nebular flux will be present in the spectra making them more easily detectable (see Figure 1.10).

Moreover, Górny et al. (2004) reports the detection of more late-type [WC] in the bulge

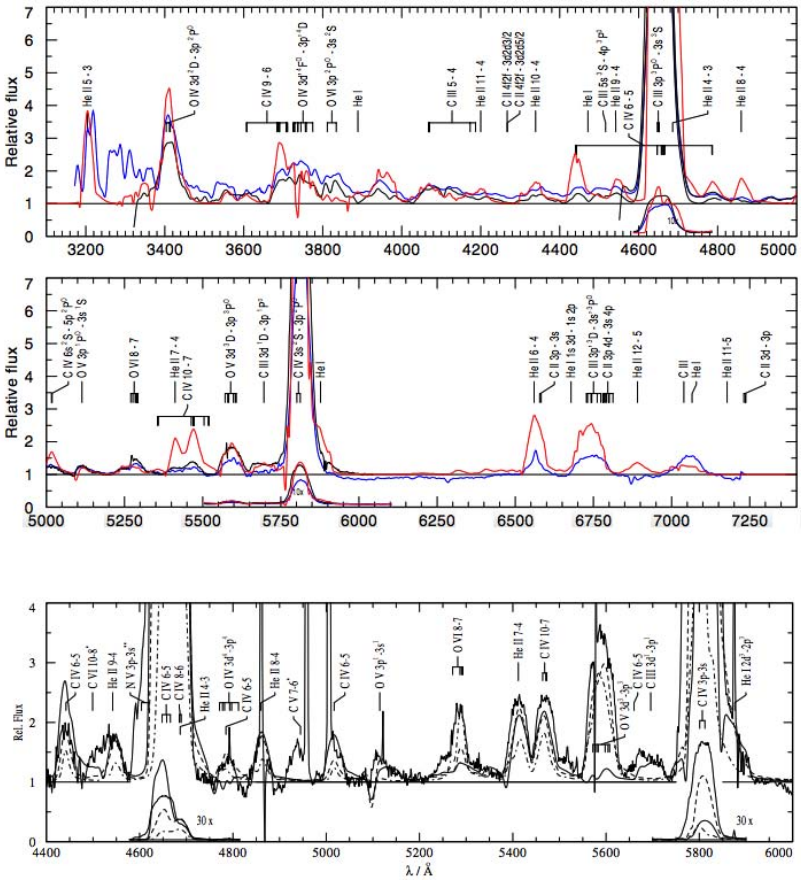

Figure 1.7: *Upper two*: Spectra of WR143 which is a WC 4 subtype (Sander et al. 2012). *Lower*: NGC 6751 which is a [WC 4] subtype (Koesterke & Hamann 1997b).

than the disk. Conversely, Depew et al. (2011) found many [WO] sub-types with deeper spectra than previously taken. The main reason behind this discrepancy might be that the spectra in the blue region are very much suppressed by interstellar absorption and the OVI-3811.34 line (one of the lines for [WO] classification) is just hard to confirm. It is quite clear that observational data do play a crucial role in the selection and classification of [WR] stars.

1.4.2 Atmospheric composition and evolutionary sequences

One very interesting question so far in this discussion is how do these [WC] CSPNe form? To understand this, the study of an evolutionary sequence of the [WR] CSPN is required. These sequences are informed by the atmospheric composition studies of these stars.

Late [WC] types ([WCL]) contain $\sim$ 50% of C, 40% of He, somehow similar to PG 1159 stars (Leuenhagen et al. 1996). They are believed to follow the evolutionary sequence: [WCL] $\rightarrow$ [WCE] $\rightarrow$ PG1159 stars (see Figure 1.11). This evolutionary sequence is in good accordance with the atmospheric compositions reviewed by Werner & Herwig (2006) and

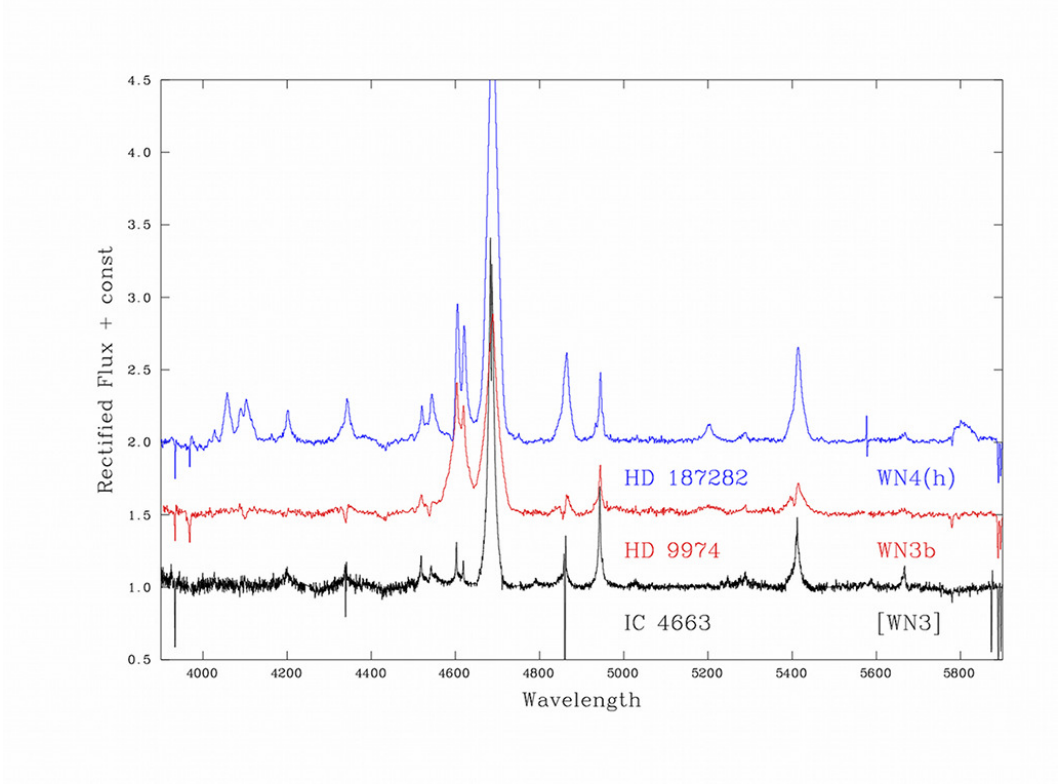

Figure 1.8: Spectra of WN 3 and 4 types (upper two) and Spectrum of a [WN 3] subtype (Miszalski, Crowther, De Marco, Köppen, Moffat, Acker, & Hillwig 2012b). A second flavor of Wolf-Rayet central stars of planetary nebulae (Miszalski, Crowther, & Moffat 2012c)

Crowther (2008). This sequence was proposed because of the strong match in chemical abundances (Fig. 1.11).

The early types ([WCE]) are known via various studies, to contain lower carbon mass fractions, with $\sim$ 30% of C and $\sim$ 60% of He (Koesterke & Hamann 1997b, Todt et al. 2006). However, Crowther et al. (2003) included clumping and line blanketing in their model calculations, which was not included in the earlier models and found that the carbon abundances in [WCE] types are not systematically lower than [WCL] types.

Recently, two new objects have been added to the [WN] scheme; IC4663 (Miszalski et al. 2012b) and Abell48 (Todt et al. 2013). Another possible member of this sequence might be PB8 which appears as an intermediate nitrogen and carbon sequence, described as a [WN/WC] type (Todt et al. 2010).

On the other hand, the formation of [WR] CSPN can be understood using the nebular abundances of PN as a probe (Gorny & Stasińska 1995). The most suitable abundance ratios which can be derived from the PN and which are primarily functions of the [WR] CSPN, are He/H, N/O and C/O (Gorny & Stasińska 1995). Gorny & Stasińska (1995) have compared the chemical abundances of $\sim$ 50 [WR] CSPNe with non-WR types and showed

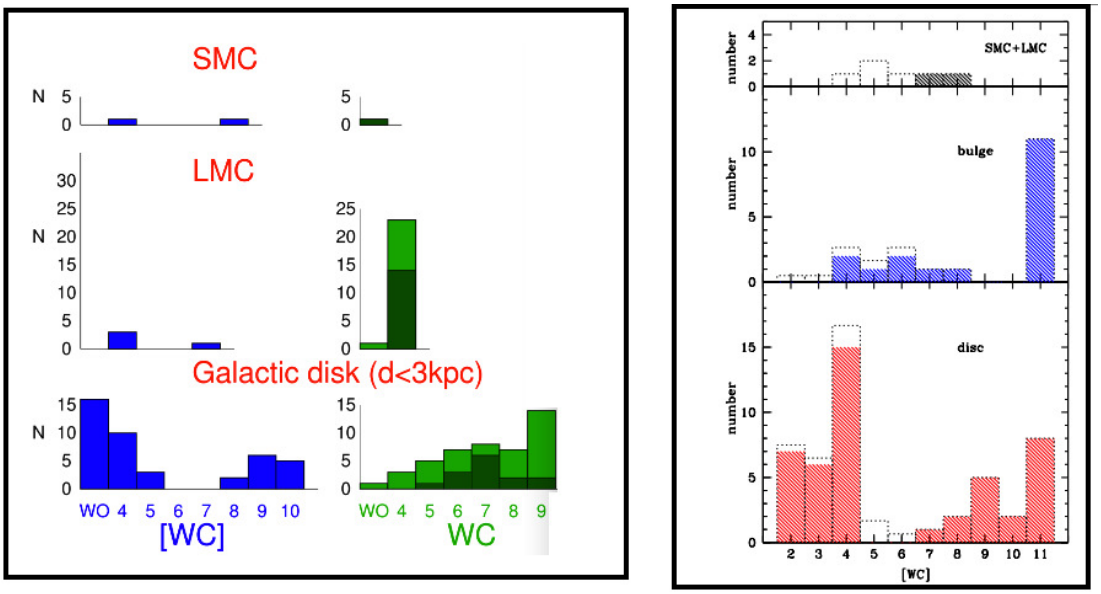

Figure 1.9: *Left*: Differences in the distribution of the [WC] and WC subtypes in the galactic disk, LMC and SMC (Crowther 2008), *Right*: LMC, SMC, Galactic disk and bulge distribution of [WC] types (Górny 2008). Note: These were discovered before Depew et al. (2011) who found many [WCE] type CSPN in the galactic bulge.

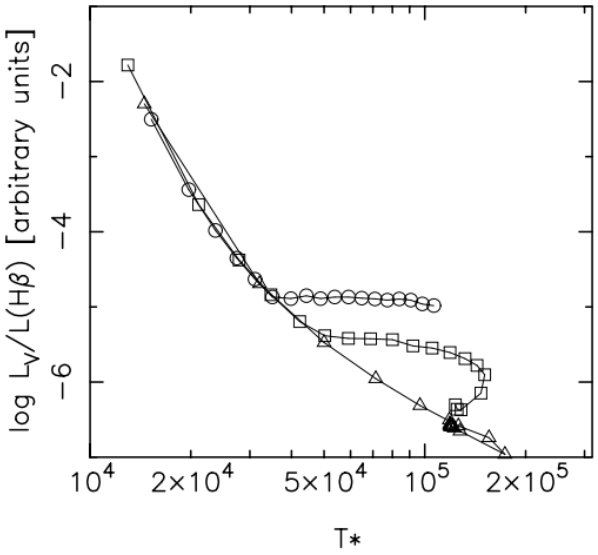

Figure 1.10: The ratio $L_V/\mathrm{L}(H_\beta)$ plotted as a function of the star effective temperature T_* from a series of models of PNe around CS of different masses. We can see the ratio $L_V/\mathrm{L}(H_\beta)$ is higher for cooler stars (Górny et al. 2004).

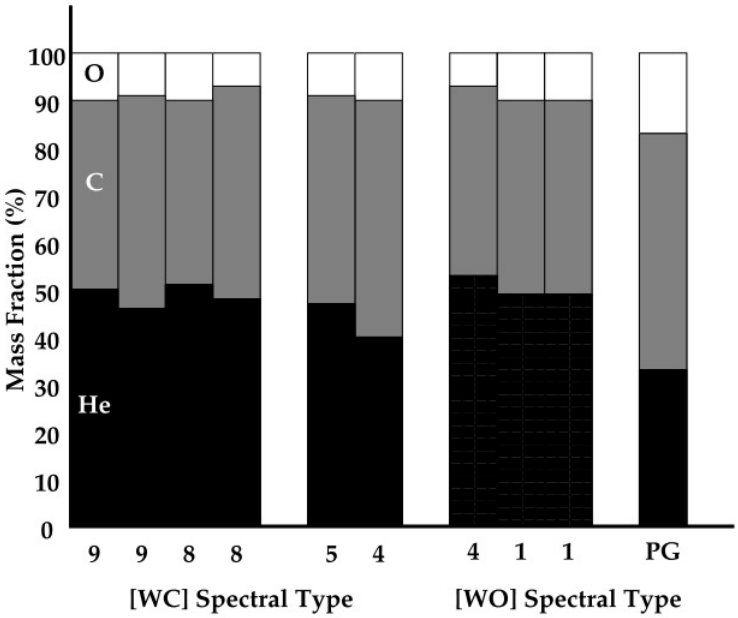

Figure 1.11: Mass fractions for [WCL], [WCE] and [WO] stars along with typical PG1159 star abundances - labelled PG (Crowther 2008).

that the distribution of He/H, N/O and C/O are the same for both samples. A similar work by Girard et al. (2007) showed that nebular abundances of PNe around [WR] types do not differ much from the non-[WR] ones. Górny et al. (2004) studied the oxygen abundances for a sample of $\sim$ 15 [WR] CSPNe and again compared with non-WR CSPNe. Also, the distribution of N/O is the same for both of the [WR] and non-[WR] CSPNe.

However, Górny et al. (2009) reports an approximate amount of 0.3 dex of S/H and Ar/H abundances in [WR] CSPNe. There seem to be no major statistical differences in the samples and Górny et al. (2009) conclude that oxygen abundances in [WR] CSs are not significantly affected by nucleosynthesis and mixing in the progenitors. In addition, a recent work by García-Rojas et al. (2013) shows that there is no correlation between the nebular chemical abundances and the [WC] stellar type, concluding that the [WR] phenomenon can occur in stars of very different stellar masses.

More tightly constrained elemental abundances in the [WC] types are required to better confirm the evolutionary sequences mentioned earlier.

1.4.3 Hydrogen deficiency in the [WR] central stars

The origin of the H-deficiency in [WR] CSPNe is currently not well understood. Werner & Herwig (2006) reviewed the properties of extremely hot H-deficient post-asymptotic giant branch (AGB) stars of spectral type [WC] and PG 1159 (which also show H-deficiency). Possible explanations for the H-deficiency are either due a late thermal pulse (LTP), a very late thermal pulse (VLTP) or an AGB final thermal pulse (AFTP).

Most of the currently known H-deficient [WR] CSPNe display spectra with strong carbon and helium lines and hence the [WC] types. There is another subtype, the [WO], which is widely accepted as a later phase in the [WC] sequence before reaching the PG 1159 phase.

In the case of an LTP, if the He-shell ignites while the star is on the constant-luminosity horizontal track, it will return to the AGB phase (termed as "born-again") (Blöcker 2001, Schoenberner 1979). Herwig (2001) argued that dredge-up may be one of the causes of H-deficiency due to an LTP. Even though the LTP does not deplete the hydrogen in the surface layer by nuclear burning, it will still develop a H-deficient surface composition. A mixing process is responsible for this. At this point, the star expands, its surface gets cooler, and envelope convection takes place. A very thin H-rich envelope layer of the order of 10^{-4} $M_{\odot}$ is mixed with a H-free layer of a few 10^{-3} $M_{\odot}$, which turns into H-deficiency as a result of dilution (Werner & Herwig 2006).

On the other hand, in the VLTP case, a He-flash occurs very late in the post-AGB evolution phase, i.e when the star is on its way to becoming a white dwarf, on the cooling track. In contrast with the LTP evolution, where the star makes only one single loop in the HRD, in the VLTP case, the star actually makes two loops as argued by Lawlor & MacDonald (2002).

At the end of the AGB phase, the star experiences a series of thermal pulses due to an increase in mass of the He shell. The latter is a consequence of hydrogen fusion occurring in the hydrogen shell above the He shell. A series of thermal pulses occurs at a time scale lower than the time it takes for the post-AGB star to exhaust is fuel. The last thermal pulse or final thermal pulse (FTP) occurs during the post AGB phase and depending on when does this happen during the post-AGB evolution, the star returns to the AGB phase as H-poor or H-free ("born-again") (De Marco 2008).

Werner & Herwig (2006) concludes that elemental abundances predicted by born-again models for the LTP for e.g Koesterke (2001), VLTP for e.g Iben & MacDonald (1995) and FTP for e.g Herwig (2001), are very much in accordance to observational data for [WC] stars from Koesterke & Hamann (1997a), Werner & Koesterke (1992). But, Górny & Tylenda (2000) found that the evolution of the nebulae surrounding H-rich stars very much resembles that of H-deficient stars, which contradicts the path followed by a "born-again" scenario.

Lau et al. (2011) debated whether a nova can be another path to producing H-deficient stars. The material ejected during outburst of the central star of PN V605 Aql is very neon rich and this neon rich composition is possibly explained by a neon nova. One of the proposed models predicts a merger of a massive oxygen-neon-magnesium white dwarf and a main sequence star. The other model derived by Lau et al. (2011) invokes an oxygen-neon-magnesium classical nova that takes place shortly after the final helium shell flash. Nevertheless, there are still drawbacks in both models. The former model is unable to determine whether the ejecta would have the observed composition of V605 Aql and whether a merger could result in the observed H-deficiency in the stellar abundances. The latter model is somewhat more physically obvious but is less frequent in occurrence based on what is implied by the number of observations. These findings are in contrast with what LTP or

VLTP predicts and an alternative explanation is required.

So, now the debate is whether the LTP and VLTP mechanisms hold for the larger sample of H-deficient stars. However, other mechanisms, such as common envelope (CE) scenarios due to close-binary evolution could be yet another route (De Marco 2008, De Marco & Soker 2002).

1.4.4 The [WN] and [WN/WC] types

The first [WN] type Wolf-Rayet CS (IC 4663) of a PN was discovered by Miszalski et al. (2012b). The spectrum displays broad He II and N V emission lines which classifies IC 4663 as a [WN3] spectral type (Fig. 1.12). The CS is surrounded by an elliptical shaped nebula contained in an Asymptotic Giant Branch (AGB) halo. The stellar atmosphere is composed mainly of helium ($\sim$ 95 %), less than 2 % of H, 0.8 % of N, 0.2% of Ne and 0.05% of O, by mass fractions.

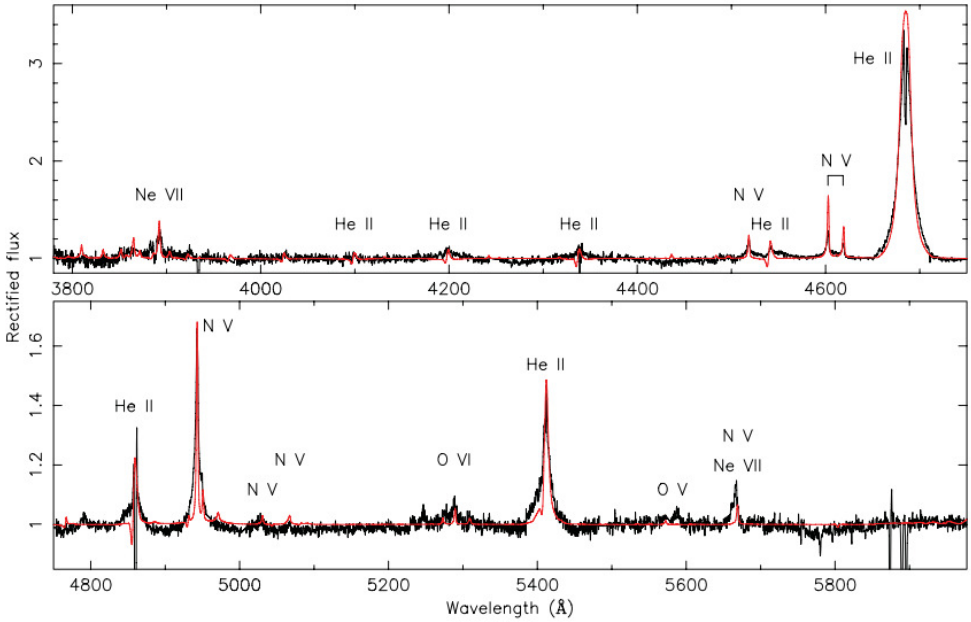

Figure 1.12: Spectrum of IC4663; a [WN 3] type CS with broad He II and N V emission lines. The red line is the NLTE model fit (Miszalski et al. 2012b).

Todt et al. (2010) reports the discovery of PB8, another interesting He-rich CSPN (tagged as an unusual [WN/WC] type by them), which does not seem to fit the [WC] paradigm. PB8 contains a significant amount of CO, which differentiates it from IC 4663. The main atmospheric compositions are 40 % of H, 55 % of He, 1.3% of C, 2 % of N and 1.3 % of O, by mass fractions. PB 8 was previously classified as [WC5-6] by Acker & Neiner (2003a) and Todt et al. (2010) gives a completely new classification to these objects, the [WN/WC] types. PB 8 shows strong nitrogen lines present in its spectrum, therefore, resembling more a [WN] type. According to the [WN/WC] classification, PB 8 might be also in a transition

evolutionary phase between the [WN] and [WC] types analogous to the WN/C types for massive WR stars. PB 8 is a slightly later type than IC 4663 and its H-deficiency can be explained by the depletion of the H-layer by for e.g a FTP whereby there is ingestion of the H envelope. Thus, by the time it reaches an earlier [WN] type, like IC 4663, it has lost almost all of its hydrogen.

One other object, Abell 48, (Todt et al. 2013) is recently added to the [WN] classification. Abell 48 contains a [WN] type CS, having strong helium and nitrogen emission lines in its spectrum and more residual hydrogen than IC 4663 which makes them slightly different. The chemical abundances are 10 % of H, 85 % of He, 0.3 % of C, 5 % of N and 0.6 % of O, as derived from the wind (Todt et al. 2013). The amount of residual hydrogen in this object might possibly rule out a merger scenario. On the other hand, the nebular morphology appears slightly elliptical.

An LTP event *cannot* explain the extreme helium rich compositions of [WN] CSPNe. LTP Models are not able to produce the high helium content in the [WN] stellar atmospheres. So, there is a need of an alternative explanation for the atmospheric composition of the [WN] types.

In the last few years, attempts have been made to explain the He-rich atmospheres of other H-deficient stars, which may be applicable to these new [WN] CSPN. Referring to Saio & Jeffery (2002), one possible explanation of the He-rich atmosphere could be a merger process of a CO+He white dwarf pairs, which in turn produces extreme helium stars and the majority of R coronae Borealis stars. The evolutionary model predicted by Saio & Jeffery (2002), has been compared to observations of extreme helium stars and the distribution of the latter in the log g, $T_{\rm eff}$ diagram is in agreement with merger models of a $\sim 0.6\ M_{\odot}$ CO white dwarf and a He white dwarf of $\sim 0.3\ M_{\odot}$. A merger of He+He White Dwarf pair (Zhang & Jeffery 2012) might be the explanation of the high helium atmospheric compositions of IC4663 and A48 (Reindl et al. 2013). One other example might be PB 8 which contains slightly more C and O abundances as compared to IC4663 and A48 and might be the result of CO+He white dwarf pair mergers. Another explanation for these He-rich objects might be a Diffusion-induced Nova (DIN) (Miller Bertolami et al. 2011). In the DIN scenario, H diffuses inwards and C diffuses outwards within a pure He intershell ("He-buffer") located in between the H and C regions, see Figure 1.13. Iben & MacDonald (1986), showed that if this He-buffer is thin enough, for stars of about $\lesssim 0.6\ M_{\odot}$ and $Z_{ZAMS} \lesssim 0.001$, the C and H regions can come into contact, causing an unstable burning. This gives rise to a sudden energy release and rapid expansion. As a consequence, the star expands rapidly, of the order of a few years, causing the visual magnitude to increase by a factor of up to 15 mag ($M_V \sim$ 9 to $\sim$ -6), in a few years. This evolutionary scenario is termed as the diffusion-induced nova and might be another route to explaining chemical compositions of the [WN], [WN/WC] type CSs. Simulations by Miller Bertolami et al. (2011) are able to reproduce typical abundances observed in Abell 48. The mass ratios of the model are H:He:C:N:O=22:73:0.66:3.8:0.1 per cent, that is close to their results of H:He:C:N:O=10:85:0.3:5:0.6 for the wind of Abell 48. Together with the low dynamical age of its nebula, this object can be explained quite well

by the DIN mechanism (Todt et al. 2013).

Miller Bertolami & Althaus (2006), explain the He-enriched PG 1159 stars by a very low mass object which leaves the AGB phase shortly before the start of the first thermal pulse. These objects experience the first thermal pulse as an LTP. After the LTP, during the evolution through the Red Giant Branch (RGB), moderate mass loss rates could turn these objects into H-deficient, but with high helium content and nitrogen deficient.

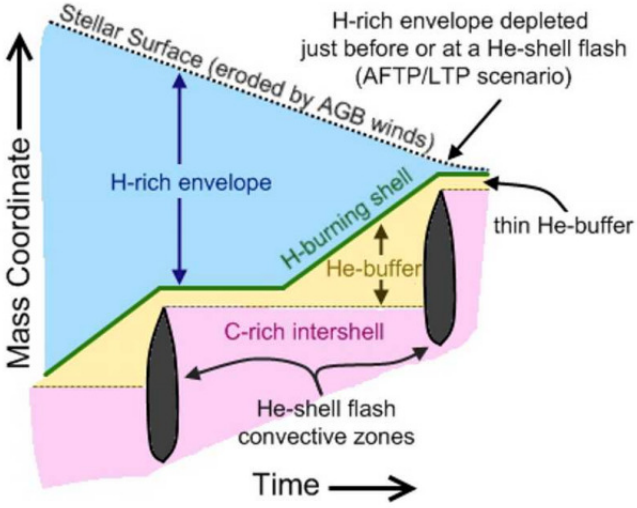

Figure 1.13: Sketch of a scenario involving the formation of DA white dwarfs with a thin He-buffer (Miller Bertolami et al. 2011).

1.5 Can binarity explain the H-deficiency of [WR] CSPNe?

There are at least 10-20 % of CSPNe which are known to be close binary systems (Bond 2000, Miszalski et al. 2009a), but only one - the CSPN of PHR0654-1045 might be a binary [WR] CSPN with a period of 0.63 days (Hajduk et al. 2010). Why are there not more [WR] CSPNe in binary systems? Or, is binarity a solution to explain the characteristics of these [WR]? Along with the aforementioned questions in section 1.4.3, this thesis aims at answering some of these new interesting questions in the field of PN.

1.5.1 PNe shaping and link to [WR] CSPNe

Understanding the PN shaping mechanism has been one of the major objectives of PN research in the last few decades (e.g Balick & Frank 2002). Previously, high-resolution studies of PNe have unfolded a rich amount of PN morphologies with complex symmetries (e.g Planetary Nebulae Image Catalogue (PNIC), by Balick (2008) & HST images of 119 PNe by Sahai et al. (2011)) (Fig. 1.14).

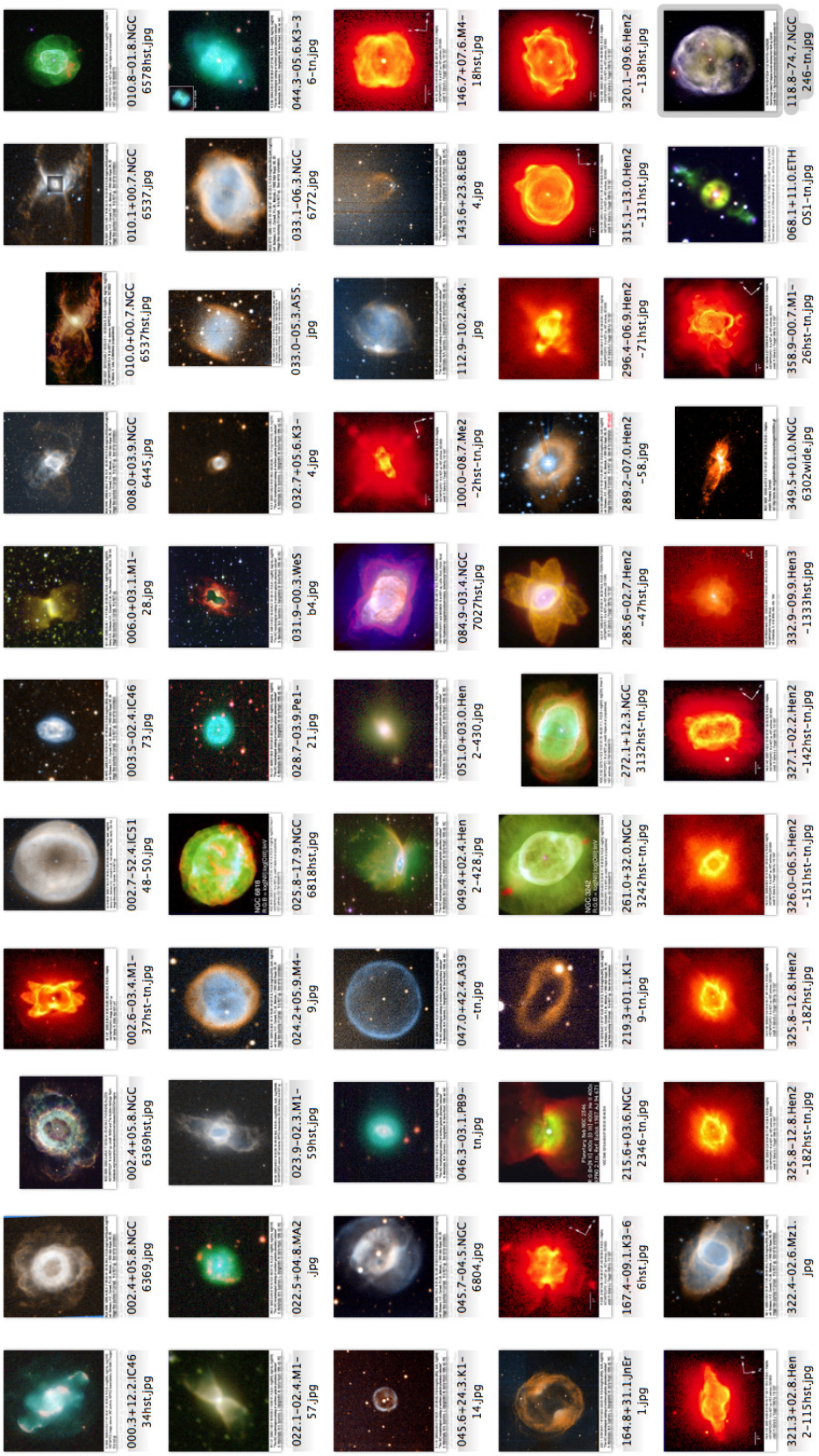

Figure 1.14: A range of complex shapes displayed by PNe including spherical, elliptical, bipolar, jets and other irregular ones (Balick (2008), Sahai et al. (2011)).

There exists other PNe showing morphological features other than the ones mentioned above, including asymmetrical shapes. For example, jets (Fig. 1.15) which are seen in PNe are believed to be ejected due to a binary interaction. A likely explanation for jets in PNe could be precessing accretion disks around the companion which accretes material and loses angular momentum due to viscosity that in turn launches episodic precessing jets (Miszalski et al. 2013). Point symmetric nebular structures are then produced (Raga & Noriega-Crespo 1993, Cliffe et al. 1995, Raga et al. 2009, Boffin et al. 2012). Precession causes smearing out or widening of the jet and could be another cause of bent jets. Furthermore, jets appearing in two pairs (e.g NGC 6778) might be results of multiple ejections and are very difficult to explain (Tocknell et al. 2013). Interestingly, the same jet-like and filament structures seen in Fleming 1 is also seen in some [WR] CSPNe (Fig. 1.15). In addition to this, LMC-N66 (Pena 1994; 1997), a [WN] type CS in the large magellanic cloud is another object which show point symmetric jet-like structures. The latter is very likely due to a binary stellar evolution. That said, the link between jets and binarity in these systems showing jets seems quite strong. The best proof of accretion in a post-common envelope binary CSPN which is linked to jets is a recent work by Miszalski et al. (2013). The Necklace (Corradi et al. 2011) is also an example of a PN hosting a close-binary central star and having polar outflows. Spectroscopic observations by Miszalski et al. (2013) reveals for the first time a carbon dwarf companion with C/O ratio of > 1 in a post-CE central star. Miszalski et al. (2013) argue that the chemical (C) enhancement of the secondary might be due to accretion from the primary, since unevolved stars are most unlikely to produce carbon. Strong evidence of accretion in the Necklace provides a clue about the origin of the pair of jets being launched, most probably, due to an accretion disk around the companion.

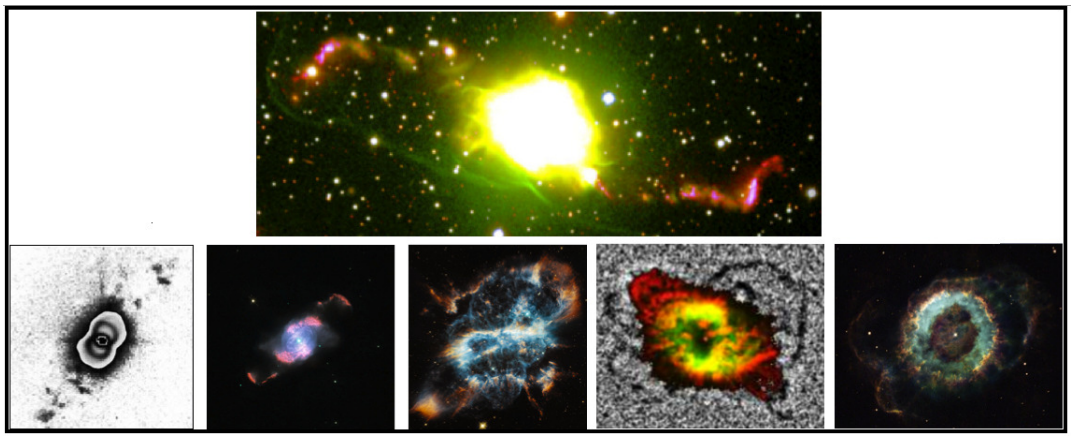

Figure 1.15: *Upper*: Fleming 1 (Boffin et al. 2012) having a set of bipolar jets. The long ones were probably ejected $\sim$ 16000 years ago while the inner nebula was ejected $\sim$ 9 to 10 000 years later. *Lower ([WR]), left to right*: MyCn18 (Bryce et al. 2004, Dayal et al. 2000), slightly bipolar shape and presence of jets. IC4634 (Guerrero et al. 2008) which also shows bent jet-like shapes. NGC 5189 (Phillips & Reay 1983) with the presence of ansae (loop or arc like structures); another shape which might be caused by precessing disk. Hb4 (Lopez et al. 1997) which shows elongated, ionized knots symmetrically on both sides of the core. NGC6369 (Monteiro et al. 2004), showing jets and filament like structures in the nebula.

The spherical shaped PNe are believed to originate from a single CSPN or may even be merged systems as in the case of an offset CSPN of A39. When it comes to the more complex shapes, new shaping mechanisms must be considered in order to explain the various morphologies. One of the schools of thought is that magnetic fields in PNe might be the main agent contributing to the complex shapes of PNe (Garcia-segura 1999; Frank 2000). Conversely, a very consistent explanation for these complex shapes is that the central stars are actually binary systems which enters a common envelope phase (De Marco 2009) (see section 1.5.4)

1.5.2 Magnetic fields as a shaping agent

The influence of magnetic fields in the PNe shaping of the nebulae is becoming a considerably important factor (e.g García-Segura et al. (1999), Frank (2000)). Theories suggest that aspherical PNe shapes might be due a stellar companion, planetary companion, magnetic fields or a combination of these. As far as magnetic fields are concerned, these are very likely to be sustained due to the action of a companion that is still present or has merged (De Marco 2009). Nordhaus & Blackman (2006) give a possible description of how magnetic fields can shape PNe via binary-induced dynamos. Three possible outcomes for common-envelope (CE-discussed in later sections) evolution (Fig. 1.16) are outlined.

1. The companion becomes embedded in the stellar envelope, their orbital separation is reduced and the envelope unbinds equatorially.

2. The companion spirals in and the envelope spins up, creating differential rotation. If there exists a deep convective zone, together with differential rotation, a dynamo is generated in the envelope (applicable for low-mass companion).

3. The companion is shredded into an accretion disc around the core and eventually, the disc drives an outflow.

Yet, as the CE phase evolves, there can be a combination of all the three above as well. For example, differential rotation in the CE phase might trigger a dynamo in the envelope. The companion continues to spiral in and eventually forms a disc, which produces a bipolar outflow. More about magnetic fields as a shaping mechanism is discussed in section 4.8.

1.5.3 Binarity as a shaping mechanism

One of the most promising explanations for the complex shapes of PNe is that the central stars are actually binary systems (De Marco 2009). A typical scenario involves an initial system of binaries composed of an AGB star (donor) and a companion star (e.g main sequence star) orbiting each other and there is transfer of material from the donor to the accretor which is the companion star. The result is a CE formation which engulfs both stars and there is loss of angular momentum due to drag forces inside the envelope, bringing them

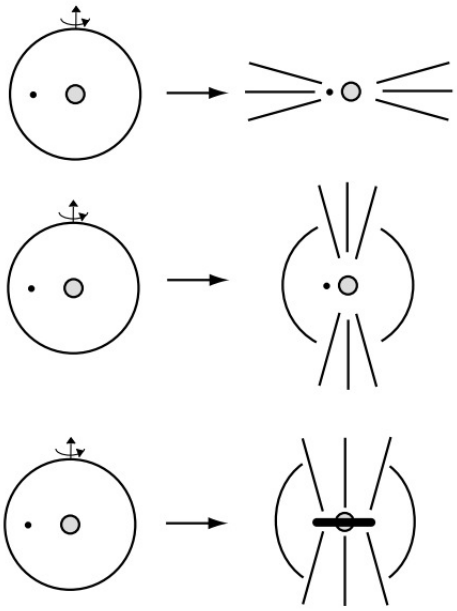

Figure 1.16: *Top*: Envelope unbinded equatorially. *Middle*: Poloidal outflow, collimated and aligned to rotation axis. *Bottom*: Disc-driven outflow (Nordhaus & Blackman 2006).

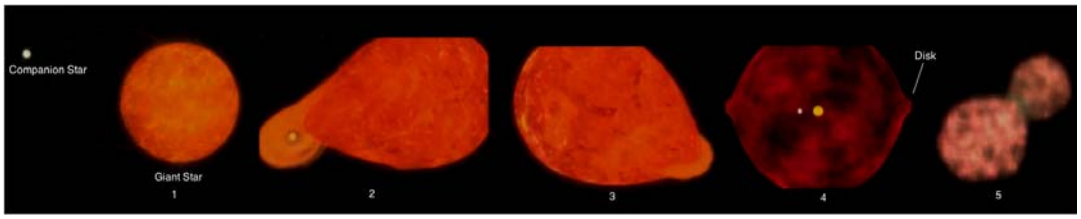

Figure 1.17: *Evolutionary phase from left to right*: 1. Initial binary system. 2. Mass accretion from donor to companion. 3. Formation of common envelope. 4. Disk formation. 5. CE ejection (Image credit: NASA, ESA and The Hubble Heritage Team (STScI/AURA)).

into closer orbit. Eventually there is a disc formation followed by CE ejection as a PN (see Figure 1.17).

The binary system left at the centre will have a period of $\sim$ 0.1-1.0 days. At the lower end of this range, some may be double degenerate Supernovae Ia progenitors with quite low periods of $\sim$ 4hr, merging within a Hubble time (Tovmassian et al. 2010).

1.5.4 Common Envelope Evolution

Iben & Livio (1993) gave a full description on the common envelope evolution in binary systems. In the Roche approximation, the gravitational field generated by the two stars acts as if they are point masses. The slight elongation along the line of centres is caused by tidal effect of the companion and centrifugal forces (see Figure 1.17). The Roche lobes are the equipotential surfaces surrounding the two stars, connected by the inner Lagrangian

point L_1. Once the donor fills its Roche lobe, it transfers mass to its companion through L_1. If the mass transfer rate is too fast for the accretor to accept, the material piles up into a hot blanket surrounding the companion. Consequently, the hot blanket begins to overflow the Roche lobe of the companion and the overflowed material is believed to form a "common envelope (CE)", in which the two stellar components are immersed. The system has a CE which is not co-rotating with the stars and therefore, the drag forces due to the velocity differences between the binary system and the CE itself, transfer angular momentum from the orbiting stars to the CE. The orbiting stellar components spiral closer and closer because a fraction (α_{CE}, known as the ejection efficiency) of the orbital energy is released and imparted to the CE. However, the value of α_{CE} is poorly constrained because the physics underlying the CE phase is not very well known (Ivanova et al. 2013, Davis et al. 2012).

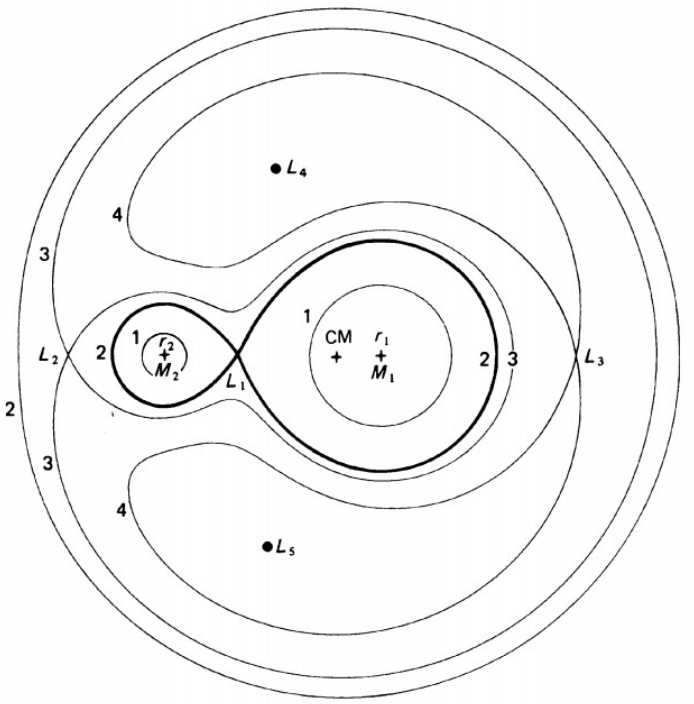

Figure 1.18: A binary system consists of two stars of masses M_1 and M_2 and radii r_1 and r_2, rotating about a common centre of mass (CM). Equipotential surfaces denoted by 1,2,3 and 4 in the orbital plane of the binary. One star fills its Roche Lobe and transfers mass to the companion through the inner Lagrangian point, (L_1) where the two Roche Lobes touch. The other Lagrangian points L_2, L_3, L_4 and L_5 are other stable points over a larger region of parameter space (Iben & Livio 1993).

PNe morphologies and their connection to CE ejection is poorly understood. There exists no direct evidence of CE ejection from observations because the timescale is too short. Soker (1996) suggested that PNe having bipolar structures might be due to binary interactions which avoid a CE phase. However, based on a larger sample of post-CE PNe, studies showed that there is at least a tendency for post-CE PNe to have bipolar structures(De Marco 2009; Miszalski et al. 2009a). Also, common-envelope PNe seem to exhibit low ionization features, knots and filaments embedded in larger, toroidal structures (Miszalski

et al. 2009a). Moreover, the morphologies of some axially symmetric PNe may be due to an enhanced mass-ejection rate in the equatorial plane of the CE compared to the mass-ejection rate in polar directions (Iben & Livio 1993).

Progress in the understanding of CE evolution in the past few years has focused on a few methods including 3-D hydrodynamical modeling of the CE ejection (e.g Taam & Ricker 2010), observational programmes to constrain the ejection efficiency (α_{CE}) (e.g Davis et al. 2012; Zorotovic et al. 2010) and population synthesis models of PNe formation rates via CE ejection (e.g Moe et al. 2006). Mitchell et al. (2007) carried out a detailed kinematical analysis of the post CE binary CS of PN Abell 63. Similar kinematics are seen in other post CE PNe, e.g ETHOS 1 (Miszalski et al. 2011) and the "Necklace" (Corradi et al. 2011). We presently need more detailed studies of PN around post-CE central stars to understand better the CE formation and ejection mechanisms.

1.5.5 Jets in CSPNe and the link to binarity

The strongest clue that [WR] CSPN may not be single stars is that many of their nebulae show jets. Jets are the only morphological structures that are strongly tied to binarity (as discussed in section 1.5.1), as is seen from several studies, discussed in the next few paragraphs.

Boffin et al. (2012) found a close-binary system at the core of the PN Fleming I (Boffin et al. 2012), with a period of 1.1953 days. Fleming I shows point-symmetric jets and it is believed that point-symmetric jets are launched by a precessing disk around a companion (Raga & Noriega-Crespo 1993, Cliffe et al. 1995).

Abell 63 (Mitchell et al. 2007) is another example where a binary central star is thought to be forming jet-like structure along its polar axis. Mitchell et al. (2007) produced a morphological-kinematical model where an inclination of 87.5° which is consistent with the binary orbit is used. Mitchell et al. (2007) show that the binary central star is capable of forming large scale structures, including jets. According to their derived kinematical ages, the jets seem $\sim$ 1000 years older the nebular rim, which would imply that the disc-generated jets should form just after the common-envelope (CE) phase but before the nebular shell (Soker & Livio 1994).

ETHOS 1, discovered later by Miszalski et al. (2011a) also shows similar jet like structures and it is suspected that it is mainly caused by its binary nucleus. Here also, the jets are $\sim$ 1000 years older than the nebula and are slightly detached (no jet activity and maybe accretion taking place for CE ejection to occur), which would give further evidence of CE ejection after the jets being launched.

A similar age difference between the polar outflow and the inner nebulae exists for this object as for ETHOS 1 and Abell 63. Therefore, making all three objects quite similar and following about the same trend of evolution. All these objects show strong connection between jets and binarity.

Interestingly, NGC 5189 (Sabin et al. 2012), composed of a WO1 type central star, also shows bent jets with a complex morphology (Sabin et al. 2012). Based on the above

mentioned evidence showing the relation between binarity and jets, the central star of NGC 5189 is ranked as a strong binary candidate. More follow up is required on this object to further prove this hypothesis.

There are some PNe with [WR] central stars which exhibit very weird, complex nebular shapes and ionization structures, for example NGC 6751, NGC5189, NGC 2452 and Hb4 (Miszalski et al. 2009b). These objects are [WO] types which contains very strong winds. Turbulence from these strong winds might disrupt the Low-Ionisation Structures (LIS) (Miszalski et al. 2009b) in these objects making the LIS not quite visible in their images (Acker et al. 2002). In addition to this, NGC 6778 is a bipolar shaped PN which seems to be shaped by fast collimated outflows which disrupt the nebular envelope (Guerrero & Miranda 2012). Guerrero & Miranda (2012) report that the equatorial ring is highly disrupted and many radial features, like filamentary wisps and cometary knots, are seen.

So, it appears that the complex nebular shapes of PNe hosting both a WR central star and a non-WR central star, have stored significant information about the binary status of their nuclei.

1.5.6 Previous variability studies

There are few [WR] CSPNe that have been studied in enough depth to constrain the nature of any potential binary companions they may have. Ciardullo & Bond (1996) studied variability in the light curves of a sample of 29 hydrogen-deficient CSPNe which exhibit early WC (WCE) or PG 1159 type spectra. Their study revealed six of these objects with low-amplitude pulsations, five of which are early WC types. An example of one of the objects (NGC6905) is shown in Figure 1.19.

Miszalski et al. (2009a) established a close binary population of $10-20$ % using photometry to derive light curves for the photometric binaries in their sample, confirming the earlier work of Bond and colleagues (Bond 2000). For a close-binary system, if we have a hot white-dwarf ($T_{eff} \geq 100$ kK)and a main sequence companion, the hemisphere of the companion will be irradiated and we will be able to see it in the light curve (e.g. De Marco et al. 2008, Corradi et al. 2011, Miszalski et al. 2011c). Also, the lightcurves associated with binaries are smoother and show more or less sinusoidal variations (Méndez et al. 1986). Moreover, Mendez et al. (1990), looked at five Of-WR CSPNe and found variation in spectral emission lines in three of them. Mendez et al. (1990) conclude that these variations are more likely to occur due to strong winds and not because of a binary system, which would produce much larger RV shifts that is seen in close-binary CSPNe. Méndez (1989) also looked at RV variability in a sample of CSPNe where no clear binaries was found. Overwhelmingly, none of the previous variability studies have been able to prove any clear binary [WR] CSPNe. The light curves from the studies are almost flat with very little variations in magnitude (in the case of pulsations). Most of the photometric variability studies have been carried out on the (very hot) [WO] types. Their light curves being almost flat might imply that they are due to pulsations and not a binary system (Ciardullo & Bond 1996).

A summary of some of the earlier RV/photometric monitoring amongst [WR] CSPN is

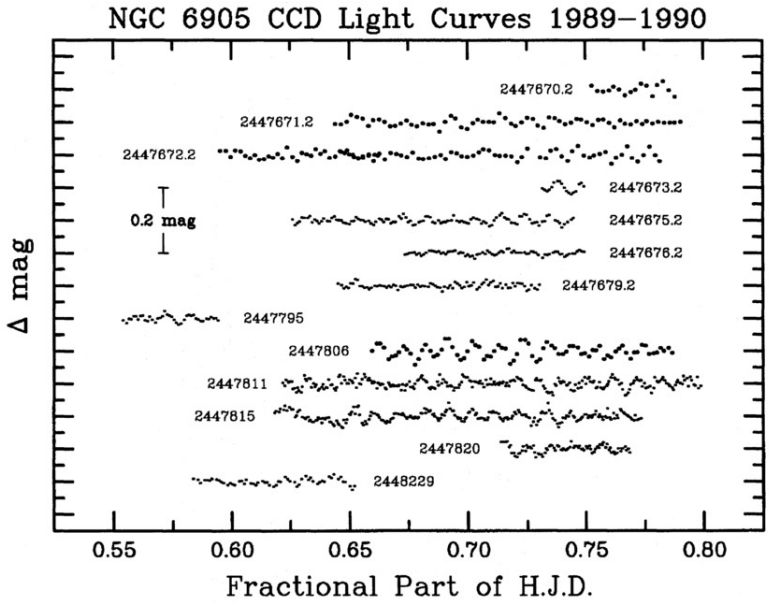

Figure 1.19: Small scale pulsations in the light curve of NGC 6905, a WO1 type object (Ciardullo & Bond 1996).

found in Table 1.1. The 1st column is the object name, the 2nd column shows the PNG number, the 3rd column is the CS type, the 4th column shows the references to each object in the table, the 5th column is the type of monitoring and the last column shows the type of variability for each object.

For the small variations in RV for CSPN with strong winds, a somewhat variable wind is the rule rather than the exception. However, one of the possibilities might be that these are mergers or single stars. A single star scenario is perhaps less likely to be an explanation for the non-variable objects, because of the very complex shapes of their surrounding nebulae.

1.6 Aim of my thesis

The aim is to study the variability of a sample of 7 [WR] CSPNe which are mostly late [WC] types. The amount of variability will give an indication of whether the systems contain a clear binary or not. The method used for this is cross-correlation of a set of spectra with a high SNR template spectrum to find radial velocity shifts. Sections 1.6.1 and 1.6.2 give a brief description of the radial velocities of a star in a binary system and the mass determination of such a system, respectively.

1.6.1 Radial Velocity review of binary stars

Spectroscopic binaries are systems with two superimposed, independent spectra. If a given star has non-zero radial velocity, Doppler shift makes its observed spectral lines shift from the rest wavelengths. For a binary system, the shift is periodic (Fig. 1.20) because the two

Table 1.1: Table showing previous variability studies.

Object	PN G	Type	ref	Monitoring Type	Variability
NGC1501	144.4+06.5	[WO4]	a,b	Photometric	pulsations
NGC2371-2	189.1+19.8	[WCE]	c	Photometric	pulsations
NGC2867	278.1−05.9	[WO2]	a,b	Photometric	pulsations
NGC5189	307.2−03.4	[WO1]	a,b	Photometric	pulsations
NGC6905	061.4−09.5	[WO2]	a,b	Photometric	pulsations
NGC6369	002.4+05.8	[WO3]	a,b	Photometric	No pulsations
NGC5189	307.2−03.4	[WO4]	a,b	Photometric	No pulsations
NGC2867	278.1−05.9	[WO2]	a,b	Photometric	No pulsations
NGC2452	243.3−01.0	[WO1]	a,b	Photometric	No pulsations
M3-30	017.9−04.8	[WO1]	a,b	Photometric	Uncertain
PB 6	278.8+04.9	[WO1]	a,b	Photometric	Uncertain
He2-55	286.3+02.8	[WO3]	a,b	Photometric	Slow/Irregular
PHR 0654−1045	222.8-04.2	[WC7/8]	g	Photometric	Possible orbital variation[1]
IC 468	215.2−24.2	O7fp	c,d	RV	No Variation
IC 4663	346.2−08.2	[WN3]	e	RV	No Variation
PB 8	292.4+04.1	[WN/WC]	f	RV	No Variation
A78	081.2−14.9	[Of/WC]	h	RV	Possible variation[2]
NGC6543	096.4+29.9	[Of-WR]	i	RV	Wind variation
NGC6826	083.5+12.7	[O6fp]	i	RV	Wind variation
NGC6572	034.6+11.8	[Of-WR]	i	RV	Wind variation

References: (a): Acker & Neiner (2003a) (b): Ciardullo & Bond (1996) (c): Méndez et al. (1986) (d): van Altena et al. (1995) (e): Miszalski et al. (2012b) (f): Todt et al. (2010) (g): Hajduk et al. (2010) (h): De Marco et al. (2004) (i): Mendez et al. (1990)

[1] May also be due to pulsations. Needs more RV monitoring.
[2] Poor quality data. Very unlikely to be a binary.

components are constantly moving around the common center of mass of the system (unless the orbital plane is 90° with the line of sight).

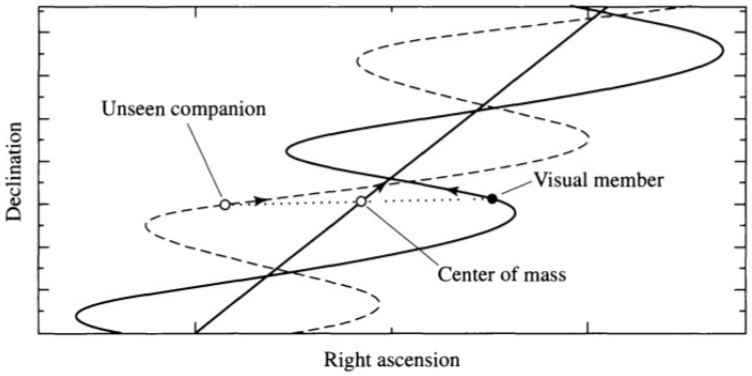

Figure 1.20: Periodic RV shifts due to oscillatory motion of the components around the centre of mass of the system (Carroll & Ostlie 2006).

However, if the period of the system is long (of the order of months or years), the periodic motion will not be readily apparent in the spectra observed in short time lapses (∼ days or

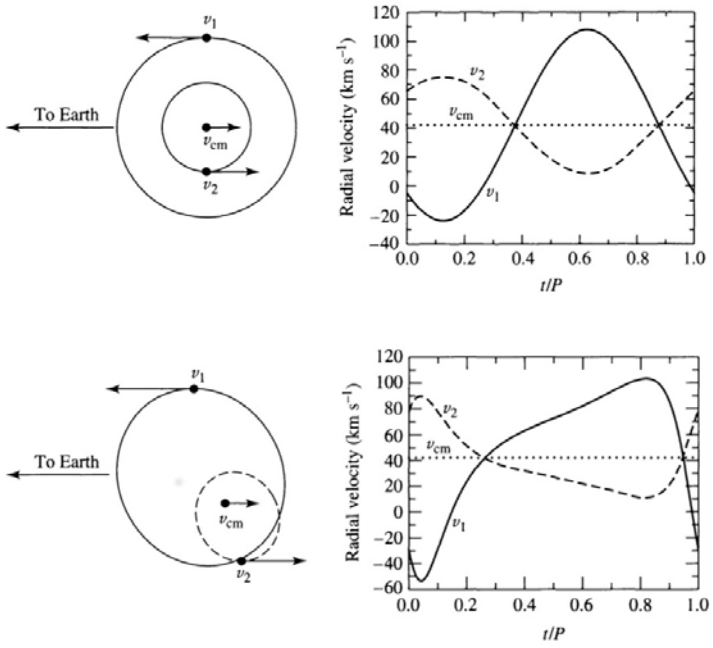

Figure 1.21: **Top**: Orbital paths and RVs of a system of two stars 1 and 2 with masses $M_1 = 1.0\ M_\odot$ and $M_2 = 2.0\ M_\odot$, velocities v_1 and v_2, in circular orbits with eccentricity, $e = 0$. The centre of mass has a radial velocity of $v_{cm} = 42\ km\ s^{-1}$ and the plane of the orbit is along the line of sight. **Bottom**: same system but with eccentricity, $e = 0.4$ and 45° orientation of periastron (Carroll & Ostlie 2006).

weeks). The latter is a case where the system needs to be sampled at longer time intervals. On the other hand, if one of the components is not overwhelmingly more luminous than the other, and if the stars can't be resolved separately, it is still possible to check the binary status by observing the superimposed and oppositely Doppler-shifted spectra. For stars of different spectral features, even if the orbital plane is perpendicular to the line of sight, a binary is still detectable by decomposing two sets of superimposed spectra that originate from both stars respectively.

For systems with short orbital periods, if the RV has a component along the line of sight, periodic shifts in the stellar spectral lines will be observed at short time scales. If the luminosity of both components are comparable, two periodically variable RV curves will be seen. Even if one of the components is far more luminous than the other (which might be the case for [WR] CSPNe), a single periodic RV curve is seen. The shapes of the RV curves depends on how eccentric the binary system is (Fig. 1.21).

1.6.2 Mass determination

The determination of masses of a WR binary system depends mainly on two factors,

- The uncertainties in the orbital inclination i.
- Errors in the velocity semi-amplitude.

For the case of visual binaries, assuming that the eccentricity of the system is very small ($e \ll 1$) and the stars have velocities v_1 and v_2, with masses m_1 and m_2, respectively. The velocities, v_1 and v_2 are constants and given by $v_1 = 2\pi a_1/\mathrm{P}$ and $v_2 = 2\pi a_2/\mathrm{P}$, where a_1 and a_2 are the semi major axes and P is the period. The ratio of the masses is then given by:

$$\frac{m_1}{m_2} = \frac{a_2}{a_1} \tag{1.1}$$

and in terms of velocities:

$$\frac{m_1}{m_2} = \frac{v_2}{v_1} \tag{1.2}$$

Now considering only the radial components of the velocities (v_{1r} and v_{2r}), we introduce the inclination i in the equations, resulting into the ratio of the masses:

$$\frac{m_1}{m_2} = \frac{v_{2r} \sin\ i}{v_{1r} \sin\ i} \tag{1.3}$$

Defining a as the sum of the semi major axes of stars 1 and 2, we get:

$$a = \frac{P}{2\pi}(v_{1r} + v_{2r}) \tag{1.4}$$

Using Kepler's third law;

$$P^2 = \frac{4\pi^2}{G(m_1 + m_2)} a^3 \tag{1.5}$$

The sum of the masses can be written in terms of the observed values as:

$$m_1 + m_2 = \frac{P}{2\pi G} \frac{(v_{1r} + v_{2r})^3}{\sin^3\ i} \tag{1.6}$$

In the case of single-line spectroscopic binaries, where only one of the stars is visible in the spectrum, Equation 1.3 allows us to replace v_{2r} with the ratio of the masses. Rearranging gives:

$$\frac{m_2^3}{(m_1 + m_2)^2} \sin^3\ i = \frac{P}{2\pi G} v_{1r}^3 \tag{1.7}$$

$$v_{1r}^3 = \left(\frac{P}{2\pi G}\right)^{-1} \frac{m_2^3}{(m_1 + m_2)^2} \sin^3\ i \tag{1.8}$$

If we include the eccentricity of the orbit, the mass of the WR star is given by Moffat (1982), as:

$$M_{WR} = k(1 - e^2)^{3/2}\ P\ K_O \frac{(K_{WR} + K_O)^2}{\sin^3\ i} \tag{1.9}$$

Where, the subscript "O" refers to the orbital companion, K_{WR} and K_O are velocity semi-amplitudes of the stars and k is a constant.

The right hand side of Equation 1.7 is known as the **mass function** and depends on the observable quantities like i and P. It is more likely for a shift to be detected if the inclination differs a lot from 0°. Thus, there is a selection effect associated with binary detection in a sample of objects and requires statistical estimates. A more representative way of choosing a value for the inclination is to take an integral value of $\sin^3 i$ ($\langle \sin^3 i \rangle$) averaged between 0° and 90°, which is ~ 0.589 (Carroll & Ostlie 2006).

The main advantage of WR stars in binaries is that we can infer the masses of both components accurately if the inclination of the plane in known (e.g. Bonanos et al. (2004)).

Chapter 2

Observations & Analysis

2.1 Observations

Spectroscopic observations of a sample of [WR] CSPNe were carried out at the South African Astronomical Observatory (SAAO) on the 1.9m Telescope using SpCCD. There were two runs over three separate weeks namely May 16^{th} to 23^{rd} of 2012, June 26^{th} to 4^{th} of 2012 and July 2^{nd} to 9^{th} of 2013. We selected several bright [WR] CSPN from a range of literature sources that were accessible from Sutherland. Table 2.1 gives a brief description of the objects in the sample. The 1st column gives the PNG number of the object, the 2nd column is the object name, 3rd and 4th columns are the RA and DEC respectively, the 5th column is the V-band magnitude, the 6th column is the type of central star each object has, the 7th column is the number of spectra obtained for each object and considered useful for cross-correlation and the last column gives the reference to each object. See Table A.2 in Appendix A for the log of observations.

Table 2.1: Table giving details of the sample of [WR] CSPNe observed.

PNG	Name	RA	DEC	V_{mag}	CS-type	Epochs	Ref.
321.0+03.9	Hen2-113	14 59 53.48	-54 18 07.5	11.9	WC10	15	a,b
309.0-04.2	Hen2-99	13 52 30.67	-66 23 26.8	13.3	WC9	9	a,c,d
332.9-09.9	Hen3-1333	17 09 00.86	-56 54 48.0	10.9	WC10	12	a,e
358.9-00.7	M1-26	17 45 57.67	-30 12 00.76	12.08	WR	6	-
309.1-04.3	NGC5315	13 53 57.00	-66 30 50.7	14.4	WO4	5	a,g,h
291.3+08.4	PHR1134-5243	11 34 38.55	-52 43 32.1	-	WC9/10	7	i
001.5-06.7	SwSt1	18 16 12.27	-30 52 08.01	11.9	WC9/10	4	a,k,l

References: (a): Acker and Neiner 2003. (b): Lagadec et. al. 2005. (c,d): Leuenhagen et. al. 1996, Mendez et. al. 1991. (e): Miszalski et. al. 2011. (f): Weidman and Gamen 2011. (g): Peimbert et. al. 2004. (h): Kastner et. al. 2008. (i): Morgan et. al. 2001. (j): Gauba et al. 2001. (k): Leuenhagen and Hamann 1998. (l): Cohen et al. 1983.

A slit width of 1.5" was used and the slit was centered on the central star. Both grating 4 (for high resolution spectra) and 6 (for low resolution spectra) were used in the first and

second runs respectively. Grating 4 has 1200 line mm^{-1} and gives a wavelength coverage of $\sim$ 800 Å at $\sim$ 1 Å resolution (FWHM). Grating 6 has 600 line mm^{-1} and provides a wavelength coverage of $\sim$ 1600 Å at $\sim$ 2 Å resolution (FWHM). The CCD was read out with a binning factor of 1x2 in dispersion and spatial axes, respectively. It was challenging to achieve the S/N we required (we aimed to get S/N $>$ 30-40 in the continuum) due to weather conditions and other restrictions. The Copper Argon (CuAr) arc lamp was used as reference spectrum before and after each exposure to calibrate the wavelength scale.

Both short ($\sim 120s$) and long exposures ($\sim 2400s$) were taken for each target, since we needed both unsaturated nebular emission lines and deep enough exposures to be able to see the stellar lines. Since this is a radial velocity monitoring, we needed arc lamp exposures both before and after the observations to correct for any time-dependent shifts in the instrument. I used the IRAF task **splot** to plot the wavelength-calibrated arc lamp spectra and measure carefully the FWHM of a number of lines, before averaging. The mean spectral resolution varied from 2.5 Å to 2.9 Å. The observations were mostly made when the seeing ranged between f $\sim$ 1.5" to 2.5". We had a mix of red and blue spectra with wavelengths described in Table 2.6, the former taken during nights where the Moon was brighter. The cross correlations were mostly run on the blue spectra, the reason being that better S/N in the blue was noted as compared to the red ones. In all the spectroscopic observations, the number of objects which were considered useful (i.e; S/N $\gtrsim$ 20 and a sufficient number ($\gtrsim$ 4) of spectra for cross-correlation), came down to seven. Please note that the "-" in the SNR column of Table A.2 refers to the spectra which had an average S/N $\lesssim$ 20 and were not included in the template construction, but still used as a spectrum for cross-correlation.

2.1.1 Data reduction

Trimming and cleaning

The flatfield exposure was plotted using the IRAF task IMPLOT and the useful region of the chip was identified. The respective x and y values to be kept, were entered into the TRIMSEC and BIASEC fields of **ccdproc** for trimming the images and subtracting the overscan region bias level. The images were then cosmic ray-cleaned using the IRAF L.A. Cosmic task in **stsdas** (van Dokkum 2001). Each cleaned spectrum was checked to ensure minimal loss in line definitions by optimizing the L.A. Cosmic parameters. This package uses a variation of Laplacian edge detection to identify and remove cosmic rays of random size and shapes. In order to obtain a well cleaned spectrum, the gain and readout noise specifications can be read from the image header and input to the task (value for the gain is $\sim 1.0\ e^-/ADU$ and readout noise $\sim 6.7\ e^-$).

Extraction and wavelength calibration

Before wavelength calibrating the spectra, they were extracted using the IRAF task **apall** that traces the stellar continuum with a polynomial fit and then sums all the pixels in user-

specified windows into a one-dimensional spectrum. I used a background window of 4 pixels both up and down the spectrum in the spatial direction and a Legendre function of order 3 for fitting the trace with the correct parameters.

The first arc spectrum was used to identify the spectral lines for the dispersion solution. In order to adjust the pixel scale to a proper wavelength scale, the emission lines were identified in the arc and were matched to the CuAr spectral atlas collated by Alexei Kniazev in 2009, which contains identified emission lines in the wavelength range $\sim$ 3800 Å to 5300 Å. The line identification was rather straightforward, where I identified around 12 emission lines spread uniformly along the entire wavelength range using the IRAF tasks **identify** and fitting a Legendre function to the data. The second comparison spectrum is based upon the solution of the first comparison spectrum and the task **reidentify** was used to achieve an optimum wavelength solution.

The dispersion fit was adjusted interactively for each aperture for a given arc, and badly fit lines were deleted to obtain an optimum fit with an average Root Mean Square (RMS) value of $\sim$ 0.15 Å. This dispersion solution was then applied to the other arcs and these solutions were fit using spline3 functions of order 3. From the solution, a dispersion of 0.49 and 1.09 Å/pix for the high resolution and low resolution spectra was obtained, respectively. Each solution was linked to the appropriate object spectrum by adding the header keywords REFSPEC1 and REFSPEC2 in the header of the object. Two arcs were used to interpolate between them in case there is any small shift in the arc during the exposure (e.g. due to influence of gravity on the grating causing flexure). The final step was to apply the dispersion solution of the wavelength calibration to set the wavelength scale of the object spectrum and this was done using **dispcor**.

The high resolution blue spectra have a wavelength range of $\sim$ 4260 Å to 5115 Å and the low resolution ones cover the $\sim$ 4025 Å to 5950 Å wavelength range. Redder spectra were also obtained at low resolution in the $\sim$ 5720 Å to 7565 Å wavelength range. A more detailed description of the wavelength ranges is found in Table A.2. These are the ranges which contain most of the stellar emission lines.

Data quality

Fig. 2.1 shows the quality of the spectra used for cross-correlation. A mean spectrum was chosen from each set and displayed here. The nebular lines in the spectra that have strong emission lines are truncated down to the level of stellar emission.

2.2 Analysis

2.2.1 Cross-correlation overview

The method used for finding radial velocity (RV) shifts in the spectra is cross-correlation. In the next few paragraphs, I outline briefly the theory behind cross-correlation as described by Tonry & Davis (1979).

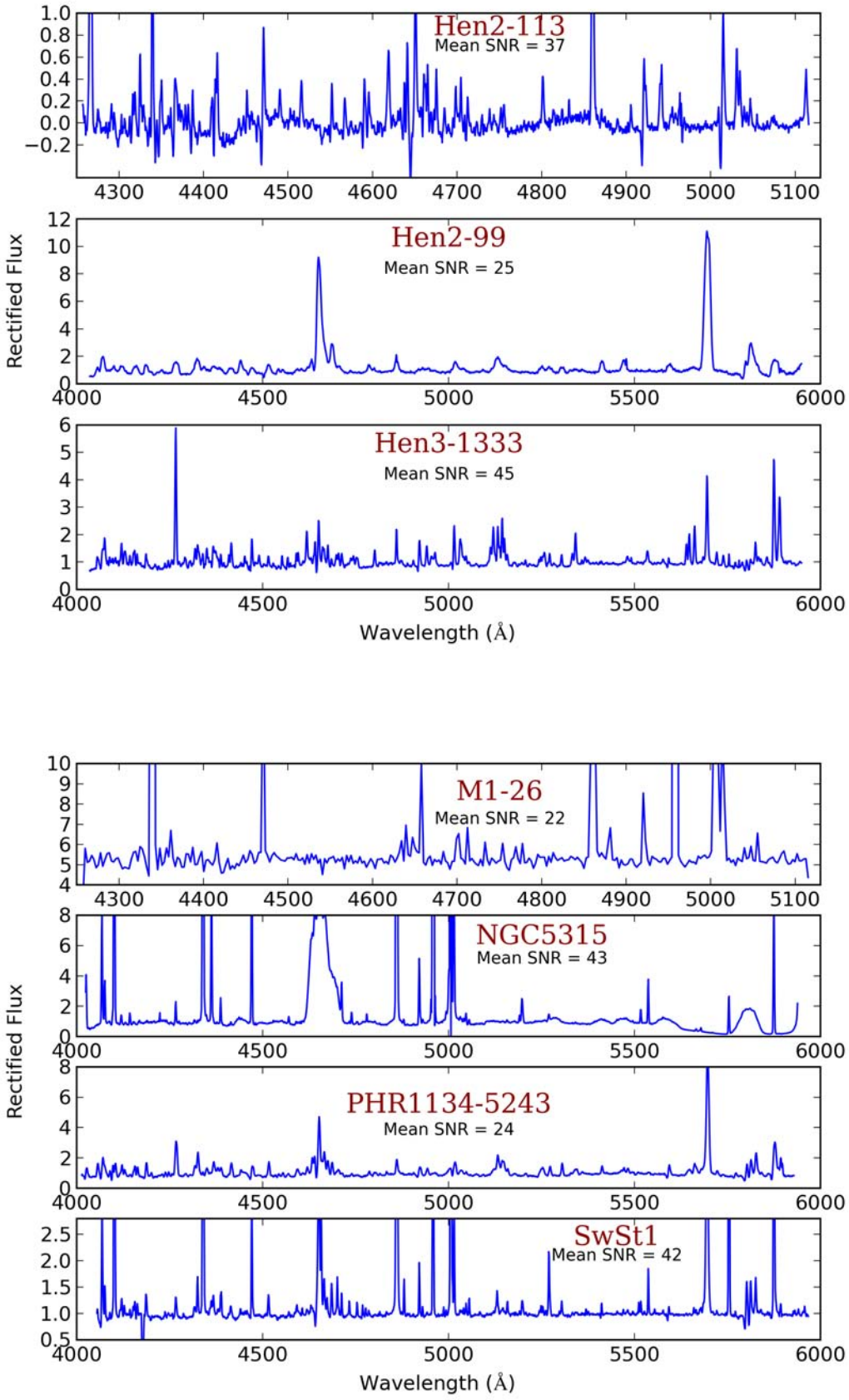

Figure 2.1: Plots of a mean spectrum for each object showing the quality of data based on the mean SNR in the continuum.

The cross-correlation task used is **xcsao** found in the RVSAO package (Kurtz & Mink 1998) that is executed in the IRAF environment. Notably, I also used **fxcor** for cross-correlating the spectra which is found in the IRAF RV package, to complement my **xcsao** results. These cross-correlation packages multiply the Fourier Transform (FT) of the object spectrum with the conjugate of the transform of a high Signal-to-Noise Ratio (SNR) template. The output which I am concerned with, is the RV shift of the object spectrum relative to the template and as well as the associated error.

The following is a brief outline of some of the main equations used by **xcsao** for cross-correlation. Let $S(n)$ be the spectrum of a star whose amount of radial velocity shift is to be found and $T(n)$ be a template spectrum of zero velocity. These spectra are discretely sampled into N bins, with bin number n. The equation connecting wavelength and bin number is:

$$n = \mathrm{A}\ ln\lambda + B \tag{2.1}$$

The spectra are assumed to be periodic with a period N, due to discrete Fourier transform and correlation functions requirements which are derived. Let $S(k)$ and $T(k)$ be the corresponding discrete Fourier transforms, with $S(k)$ defined by:

$$S(k) = \sum_n S(n)\ exp(-2\pi ink/N) \tag{2.2}$$

Let σ_s and σ_t be the root mean square (rms) of the spectra:

$$\sigma_s^2 = \frac{1}{N}\sum_n S(n)^2 \tag{2.3}$$

And therefore, the normalized cross-correlation function $c(n)$ is defined as:

$$c(n) \equiv S(n) \times T(n) = \frac{1}{N\sigma_s\sigma_t}\sum_m S(m)\ T(m-n) \tag{2.4}$$

This cross-correlation product ($\times$), is not commutative. It is defined so that if $S(n)$ is shifted by an amount d from the template $T(n)$ and if $S(n)$ and $T(n)$ are identical, then $S \times T(n)$ will have a peak of 1.0 at $n{=}d$. Now if we Fourier transform the formula for $c(n)$ we get:

$$C(k) = \frac{1}{N\sigma_s\sigma_t}\sum_m S(k)\ T^*(k) \tag{2.5}$$

Where the * indicates a complex conjugate.

Shift estimation

If $S(n)$ is some multiple α of $T(n)$ and shifted by an amount, say, δ. If $S(n)$ is broadened by a convolution with a symmetric function $B(n)$:

$$S(n) \simeq \alpha\ T(n) * B(n - \delta) \tag{2.6}$$

And here the $*$ means a convolution and not conjugate. **xcsao** estimates the parameters α and δ by minimizing the χ^2 written here in the Fourier space:

$$\chi^2(\alpha, \delta; b) = \sum_k \left[\alpha\ T(k)\ B(k)\ exp\big(-\frac{2\pi i k \delta}{N}\big) - G(k)\right]^2 \tag{2.7}$$

This equation applies quadratic weights to any deviations from zero and therefore, strong lines in the spectrum will be more strongly weighted than the weaker lines. Also, various experiments carried out showed that quadratic weighting is the best. Assuming that the largest peak in $c(n)$ is approximately Gaussian shaped, centered at δ with dispersion μ, then the value of σ that minimizes Equation 2.7 is (see Tonry & Davis 1979 for a rigorous derivation):

$$\sigma^2 = \mu^2 - 2\tau^2 \tag{2.8}$$

Where, τ is the dispersion of the largest peak in the template $T(n)$ which is assumed to be Gaussian in the Fourier space. Therefore, Equation 2.8 is showing us that the width of the cross-correlation peak is a mean of the widths of the stellar lines quadratically added to that of the template lines. To summarise, after the cross-correlation of the stellar spectrum with the template spectrum, which are rebinned to a similar dispersion, the resultant peak is fit by a smooth symmetric quadratic function with central height α, centered at δ and having width σ (see Figure 2.2).

Error measurement

The treatment of error in **xcsao** is the one derived by Kurtz & Mink (1998). Even though the data are not discretely binned, a peak is selected by fitting a smooth curve with accurate values of δ (the central value), h (the height of the central peak, analogous to α) and w (the full width half max of the peak, analogous to σ). Kurtz & Mink (1998) assumed a sinusoidal noise profile, with the halfwidth of the sinusoid = halfwidth of the correlation peak. The mean error output by **xcsao** is a single velocity measurement and is given by:

$$error = \frac{3}{8}\frac{w}{(1 + r)} \tag{2.9}$$

Where w is the FWHM of the correlation peak and r is defined in Tonry & Davis (1979), as the the ratio of the height of the true peak to the average peak. Tonry & Davis (1979) also tested the error estimation using **xcsao** by comparing histograms of observed data and expected results and concluded that the error estimations by **xcsao** are accurate to $\sim 20\%$.

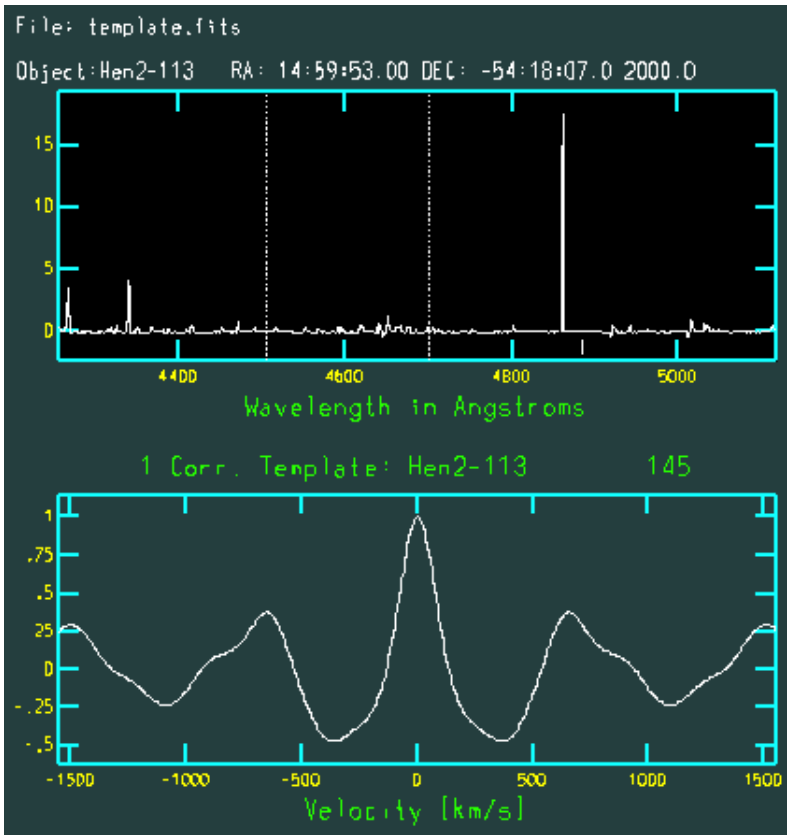

Figure 2.2: Example of the cross-correlation function for Hen2-113, cross-correlated with a high SNR template, in the wavelength range 4505 to 4700 . Top: wavelength range selected in **xcsao** shown by dotted vertical lines. Bottom: plot of cross-correlation function.

2.2.2 Application of the cross correlation method

Template construction

For a consistent RV monitoring programme, the spectrum which is used as cross-correlation template must have high SNR in the continuum. This requirement allows us to be less sensitive to any line-profile variations. The object spectra need to be cross-correlated with this high SNR zero-velocity template to obtain accurate RV shifts. Before creating a zero velocity template, the radial velocities needs heliocentric correction, because of the earths' different positions in its orbit during observation (see Figure 2.3).

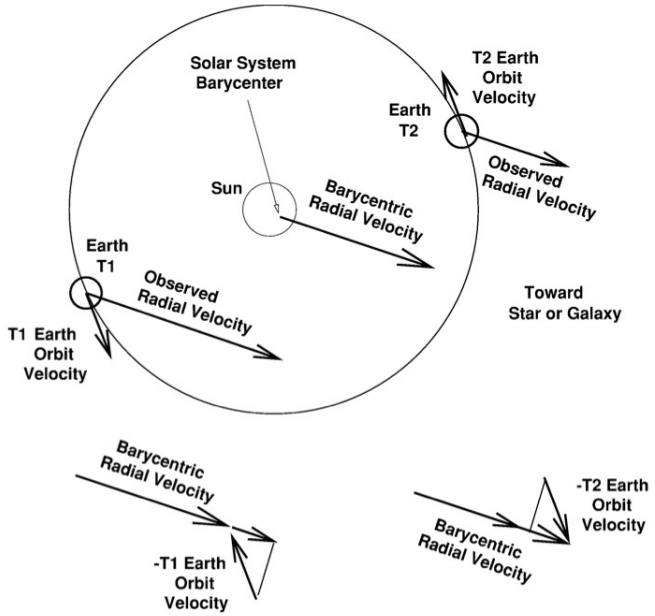

Figure 2.3: The radial velocity correction shown at 2 different times (T1 and T2) in the earths' orbit around the sun. The velocities are corrected to that which would be observed from the center of the solar system (Carroll & Ostlie 2006).

The **xcsao** task computes this correction using subroutines which reads the header information, which includes the object position (RA, DEC and EPOCH), observation site latitude (SITELAT), site longitude (SITELONG), site elevation (SITEELEV), observation date (OBS-DATE), the time when the observation started (UTOPEN) and exposure time (EXPOSURE). Using the **observatory** task in IRAF and choosing SAAO as the observing site, the information about the site may be obtained. If these header keywords are different, the user will have to update them accordingly in the headers. Once the headers are updated, running **bcvcorr** on the spectra, will output the heliocentric (hcv) and barycentric velocity (bcv) correction for each spectra. I chose an IRAF setting, where, once ran, **bcvcorr** writes the hcv and bcv computed values in the spectra headers so that whenever **xcsao** is used, the output velocities are hcv corrected.

I used the method described by Foellmi et al. (2003a;b) to create the high SNR template.

This method of constructing the template is advantageous in more than one way. Firstly, it is less sensitive to any line-profile variations, because they tend to be averaged out in the mean spectrum. Secondly, the user has the freedom of specifying the weight of a given spectrum in the set, as its contribution to the template construction. The latter proves to be very useful in situations where we have spectra of different average S/N in the continuum and more weight is to be applied to the ones with higher S/N (total weight being 1.0).

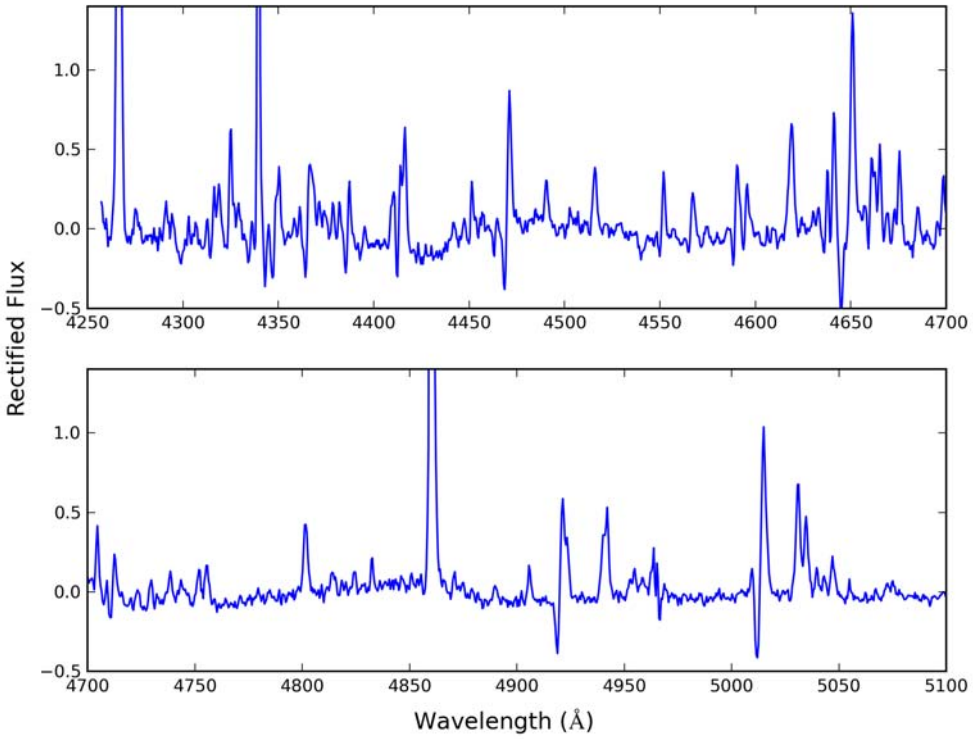

Figure 2.4: Normalized spectrum of Hen2-113 brought to zero continuum level.

The template construction was rather straightforward. Firstly, the data were grouped into sets which had the same resolution. All the spectra in that given set were normalized and brought to a zero continuum level by subtracting unity using the IRAF task **sarith** (see figure 2.4). They were then converted to a logarithmic wavelength scale using the IRAF task **dispcor** because cross correlation works in log wavelength space.

The spectral regions which contain most of the stellar lines (excluding the nebular emission lines as far as possible), used for cross-correlation are described in Table 2.6. The spectra were then plotted one by one and I measured the SNR in different regions (in the continuum) for each spectrum. Only spectra with an average SNR of ≥ 25 in the continuum were considered as good enough for cross-correlation. An average SNR was computed for each spectrum in the set and the one with the highest mean SNR in the continuum,

was used as first template (T1) for cross-correlation. All the other spectra in the set was cross-correlated with T1 and the RV shifts with respect to T1 was written to a log file (xcsao.log).

All spectra are now shifted to the common zero velocity template spectrum using the IRAF task **velset** using the result of the first cross-correlation (Fig. 2.5)

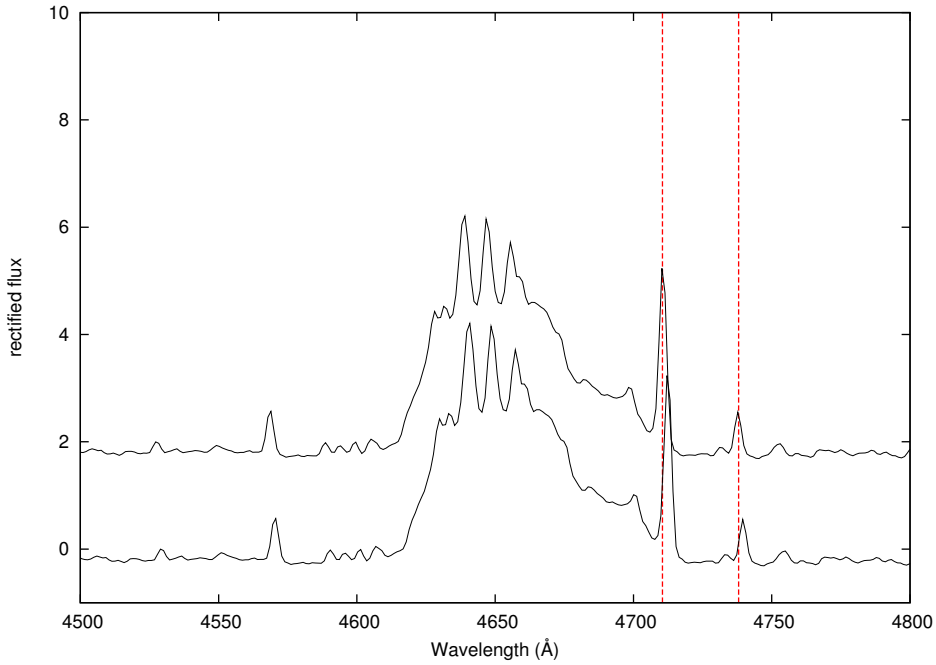

Figure 2.5: Plot of 2 different spectra of NGC5315 showing shift in the [ARIII]+He I 4711 and [Ne IV] 4724 lines, after running **velset** on the unshifted one (upper plot) with a shift velocity of $\gtrsim$ 114.3 km/s.

Now that we have all spectra shifted by a their respective velocity values, we are ready to build the zero velocity mean template T2 (template.fits). The IRAF task **scombine** is used to construct T2, weighted by the corresponding SNR in the continuum. T2 is then used to recompute new RVs using **xcsao**.

As we can see from Table 2.2 and Table 2.3, the errors in the first iteration are low enough, so I decided not to carry out a second iteration in my analysis. We would expect to trust the results if the cross-correlation peak is $\gtrsim 0.9$ and indeed we were able to achieve this peak in the first iteration itself (only if the spectra had a decent S/N in the continuum). Also, we are following the method of Foellmi et al. (2003b) in this approach, not worrying about a second iteration. Moreover, our resolution does not warrant any further iterations.

The same RVs was computed using **fxcor** task in the IRAF, RV package. The results are shown in Table 2.4.

I also plotted the results from **xcsao** and **fxcor** which match very well (Fig 2.6).

Table 2.2: Table shows the first cross-correlation output from **xcsao** for Hen2-113 (blue region), where the objects are cross-correlated with highest mean SNR template (obj24nz). The 1st column shows the object, the 2nd column is the first template used, the 3rd column is the R value for each cross-correlation, the 4th and 5th columns shows the RV shift and error in the RV shift, respectively. The 6th column is the height of the cross-correlation peak, the 7th column is the width of the cross-correlation curve and the last column refers to the mean SNR in the object spectrum.

Exp. No.	T1	R Value	RV Shift (km/s)	Error (km/s)	H	W	$\langle S/N_{Obj} \rangle$
obj22nz	obj24nz	45.29	0.4	1.0	0.960	74.412	30
obj24nz	obj24nz	8.454E7	0.0	0.0	0.984	70.092	51
obj26nz	obj24nz	54.19	-0.1	1.0	0.973	71.289	38
obj32nz	obj24nz	50.83	-0.3	1.0	0.974	72.430	48
obj54nz	obj24nz	3.86	25.0	10.0	0.347	69.040	5
obj67nz	obj24nz	54.85	4.0	1.0	0.970	73.288	31
obj82nz	obj24nz	4.38	-12.0	10.0	0.347	70.308	6
obj85nz	obj24nz	47.50	1.0	1.0	0.955	75.498	31

Table 2.3: Table shows the second cross-correlation output from **xcsao** for Hen2-113 (blue region) after using the mean velocity template T2 (template.fits). Note: the columns labels are explained in Table 2.2.

Exp. No.	T2	R Value	RV Shift (km/s)	Error (km/s)	H	W	$\langle S/N_{Obj} \rangle$
obj22nzl	template.fits	94.88	0.3	0.6	0.973	77.097	30
obj24nzl	template.fits	67.17	-0.1	0.8	0.978	74.266	51
obj26nzl	template.fits	82.96	-0.3	0.6	0.980	74.431	38
obj32nzl	template.fits	113.53	-0.5	0.5	0.983	75.352	48
obj54nzl	template.fits	3.93	26.0	11.0	0.387	70.864	5
obj67nzl	template.fits	76.09	4.5	0.7	0.980	76.162	31
obj82nzl	template.fits	3.83	-12.0	11.0	0.376	75.695	6
obj85nzl	template.fits	71.87	1.0	1.0	0.973	78.029	31

Using the bisector method to obtain absolute RV for the template

The emission line profiles were carefully examined while dealing with the cross-correlation method for the whole sample. Mostly, the bottom of the line is affected by the broad wings of other nearby (often overlapping) lines, interfering with the line profile being measured. Also, due to our restricted wavelength range, only a few strong stellar lines were seen in the spectra. Thus, it was onerous to identify a proper (unblended) stellar emission line to be used for diagnosing the stellar RVs.

Many WR stars are known to have emission lines with intrinsic line-profile variations that could influence the RV (e.g; Grosdidier et al. (2000)) at the top of the line, see Figure 2.7. So, to overcome this Foellmi et al. (2003a) uses the bisector method, which I chose to use as well.

Grosdidier et al. (2000) inspected the line variability of a sample of late-type [WC] CSPNe. The variability is very similar to that observed in the massive WC 9 star WR 103 (Robert 1992). The wind fragmentation is believed to be purely due to an atmospheric wind phenomenon, despite many differences between both types.

The online available tool **VOSpec** (Osuna et al. 2005) is one which is used for multi

Table 2.4: Table shows the cross-correlation output from **fxcor** for Hen2-113 (blue region) after using the mean velocity template T2 (template.fits). Column 1 shows the object name, column 2 is the object used to cross-correlate with T2, the 3rd column is the height of the cross-correlation peak, the full width half max of the cross-correlation function is shown in the 4th column, the 5th and 6th columns are the RV shift and the error, respectively.

Object	IMAGE	Height	FWHM	RV Shift (km/s)	Error (km/s)
Hen2-113	obj22nzl	0.98	221.83	0.5	1.0
Hen2-113	obj24nzl	0.97	219.46	-0.5	0.8
Hen2-113	obj26nzl	0.98	214.84	-0.9	1.0
Hen2-113	obj32nz	0.98	222.76	-0.3	0.5
Hen2-113	obj54nzl	0.36	152.80	23.0	16.0
Hen2-113	obj67nzl	0.97	228.29	5.6	2.0
Hen2-113	obj82nzl	0.35	173.69	-10.0	18.0
Hen2-113	obj85nzl	0.98	220.81	1.0	1.0

wavelength spectral analysis. **VOSpec** was used for bisecting well chosen, isolated stellar emission lines in the template spectrum. In the example below (Figure 2.8), the CIII 5696 line is bisected with a large number of horizontal levels between the two wings of the line and the midpoint of each level is shown by the blue dots. This is to make sure that neither the tip of the line nor the wings are affected while measuring the centre wavelength.

I varied the fraction of the emission line height (h) used for obtaining the middle point for different objects. This was done, because for different lines, I had to guess the portion which is more or less vertical. Whereas, Foellmi et al. (2003b) used a fixed fraction of $\sim 0.3h$ and $\sim 0.7h$. For this particular line (CIII 5696), the fraction used was $\sim 0.4h$ and $\sim 0.7h$.

Seemingly, **VOSpec** was introducing a $\sim$0.5Å shift in the template with respect to the one loaded on IRAF (which is trusted more) *. So, I had to introduce a velocity correction in all my calculations, which I called v_{cor} and made sure that the results of this thesis are not affected by this shift introduced. If the velocity as measured by **VOSpec** is v_{vospec} and the one by IRAF is v_{IRAF}, then:

$$v_{cor} = v_{vospec} - v_{IRAF} \tag{2.10}$$

To get the centre of the emission line by **VOSpec**, a gaussian was fitted to the line (Figure 2.9).

After the bisection, the chosen portion was fitted with a straight line, shown in black in the lower panel of Figure 2.8. The mid-point of this polynomial was obtained simply by moving the cursor in the **VOSpec** interface, on the figure midway between the fitted line. The rest wavelength of this line was retrieved from NIST website (NIS 2013), $\lambda_{rest} = 5695.92$ Å. Both of these wavelengths are substituted into the Doppler formula (Equation 2.11) to obtain the radial velocity of the central star V_r.

$$V_r = c \times \frac{\lambda_{obs} - \lambda_{rest}}{\lambda_{rest}} + v_{cor} \tag{2.11}$$

*The **VOSpec** developers were emailed about this problem and a request was made to release an updated version of **VOSpec** with no reply from them.

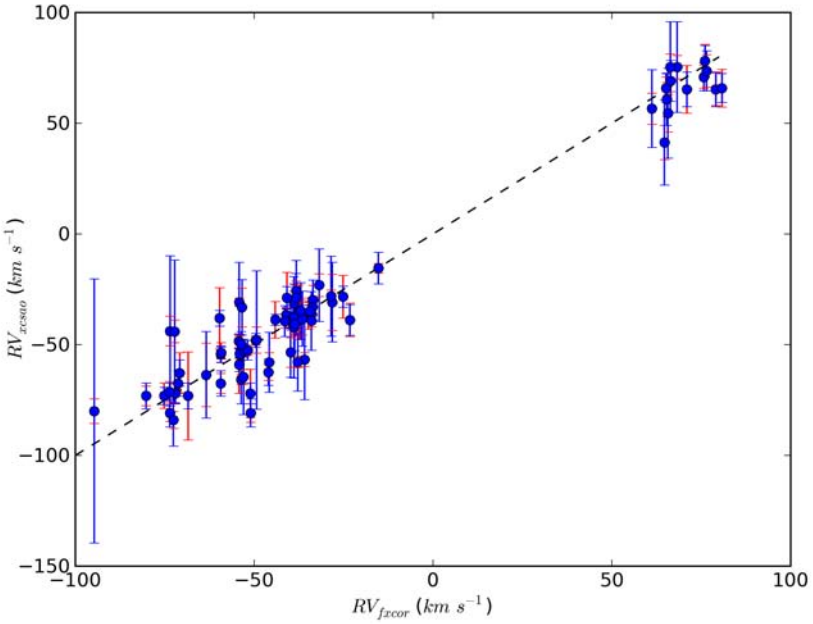

(a) Plot of *fxcor* (red) v/s *xcsao* (blue) velocities.

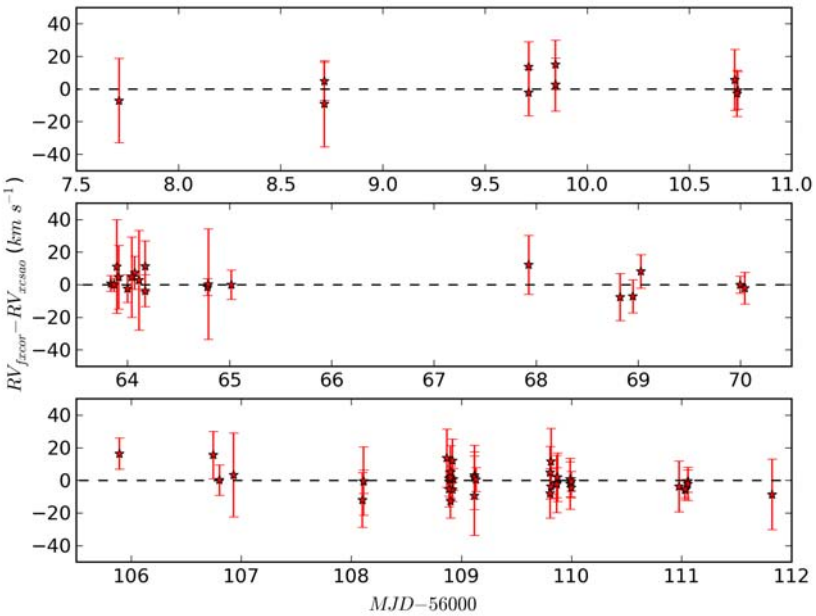

(b) Difference between *fxcor* and *xcsao* velocities plotted against Modified Julian Date.

Figure 2.6: These plots show that the cross-correlation outputs from both *xcsao* and *fxcor* are consistent with each other.

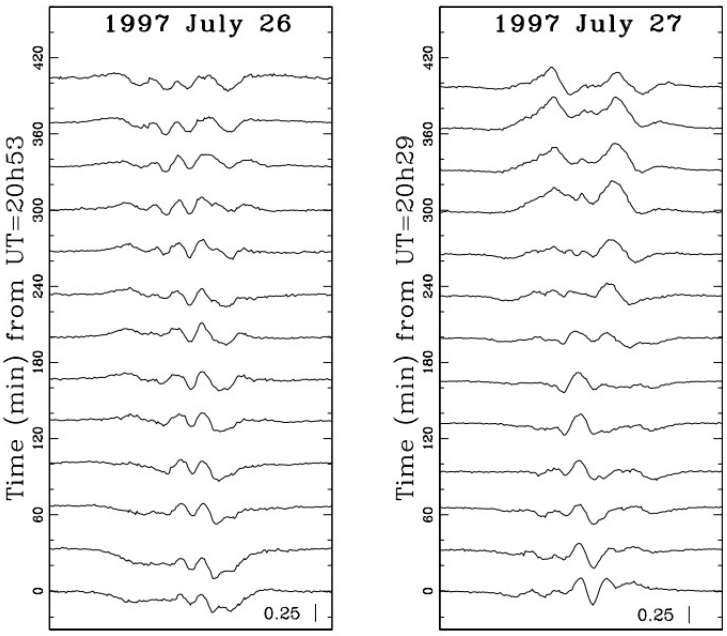

Figure 2.7: Residual for the mean profile of 2 nights of the CIII 5696 line (the best line to display variability) for BD +30°3639. The temporal behavior of the line profiles can be seen clearly (Grosdidier et al. 2000). Note: the x-axis scale is Å.

Where , v_{cor} was calculated to be (for this emission line):

$$v_{cor} = 57.4 \text{ km s}^{-1} \tag{2.12}$$

Where, c = 2.99792458 $\times$ 10^5 kms^{-1}, is the speed of light. In this case, the stellar radial velocity is:

$$V_r = 2.99792458 \times 10^5 \left(\frac{5694.1 - 5695.92}{5695.92} \right) \text{ km s}^{-1} + v_{cor} \tag{2.13}$$

$$V_r = -38.4 \text{ km s}^{-1} \tag{2.14}$$

After obtaining V_r, the barycentric velocity correction (V_{bcv}), is the next velocity needed to compute the correct radial velocity.The **bcvcorr** task was then run on the spectra to get V_{bcv}, which is plugged in Equation 2.17.

Errors in the bisector method

I calculated the errors in the radial velocity ($\triangle V_r$) by simply multiplying the wavelength difference corresponding to half the length of the fitted polynomial through the bisected points (i.e, maximum wavelength value - midpoint) by $\frac{c}{\lambda_{rest}}$. In this case:

$$\Delta V_r = 2.997 \times 10^5 \left(\frac{5694.13 - 5694.1}{5695.92} \right) \text{ km s}^{-1} \tag{2.15}$$

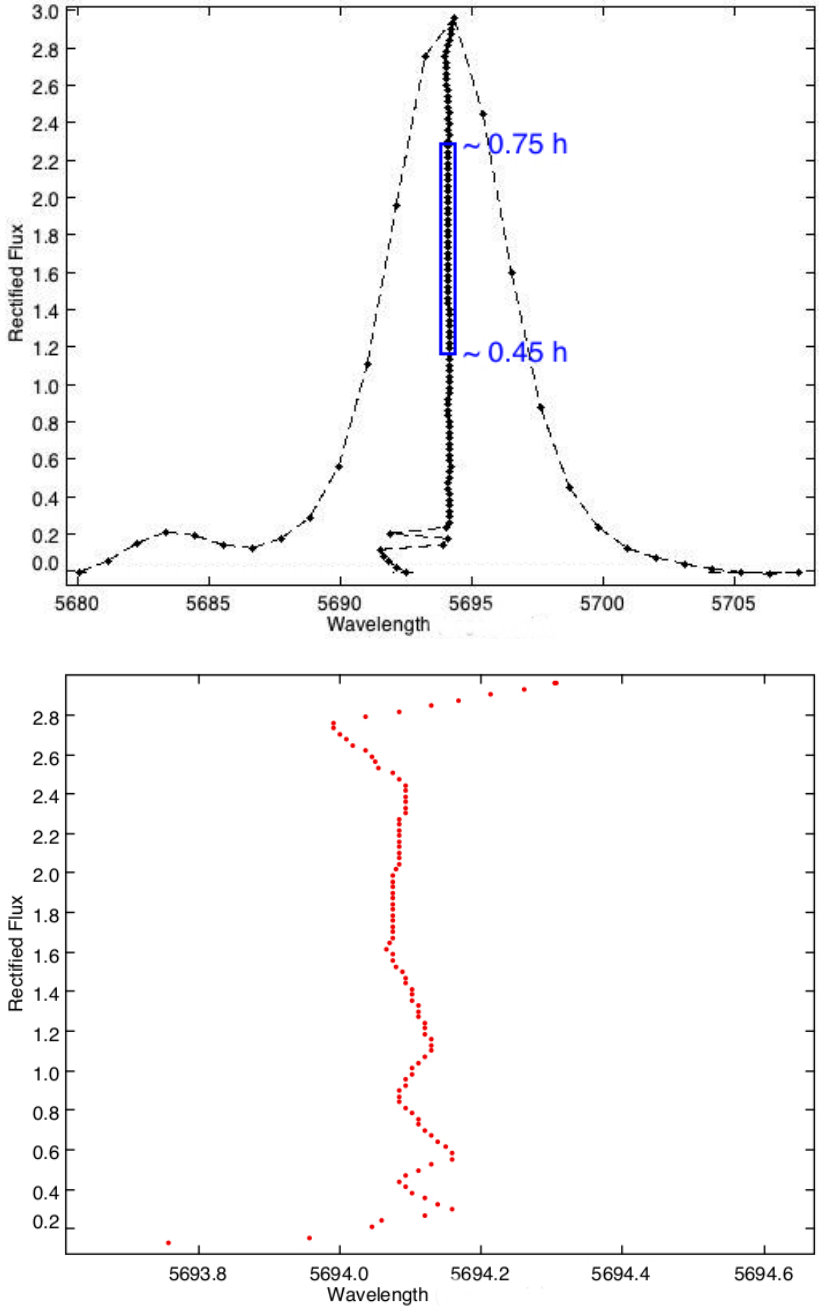

Figure 2.8: **Top:** Plot of the CIII 5696 emission line for Hen3-1333. The figure shows a hundred levels of bisection and the approximate vertical region ($\sim 0.45h$ to $0.75h$) used to fit a straight line having its midpoint at $\lambda_{obs} \sim 5694.1$ Å. **Bottom:** The linear fit to the "straight" part of the bisected points.

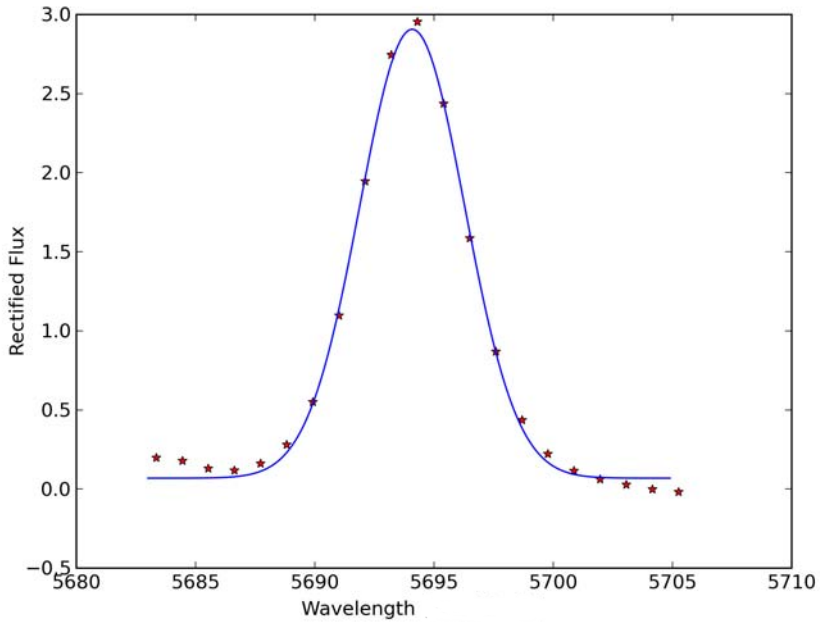

Figure 2.9: Gaussian fit to stellar line for obtaining correction.

$$\Delta V_r = \pm 2.0 \text{ km s}^{-1} \tag{2.16}$$

Finally, the corrected radial velocities (V_i) corresponding to each spectrum was computed and are given by:

$$V_i = V_{xcsao/fxcor} + (V_r + V_{bcv}) \tag{2.17}$$

Where $V_{xcsao/fxcor}$ are the velocity shift output by **xcsao** and **fxcor** after the cross-correlation, respectively.

This process was carried out for all the other objects in my sample and plots of heliocentric julian date (HJD) against RV were obtained to check for any RV shift. The main stellar line regions used for cross-correlations are summarised in Table 2.6.

The nebular velocities were obtained by running the task **emsao** on the spectra. **emsao** automatically identifies a number of nebular emission lines in the spectrum using a line list, then fits them to output the velocities of the identified lines. However, sometimes I had to specify the line name, because **emsao** would not identify the lines correctly. An example of the corrected velocities cross-correlated with the template for Hen2-113 and with wavelengths ranges defined in Table 2.6, is shown in Table 2.5. The first column of Table 2.5 is the exposure time for each object. The 2$^{\text{nd}}$ column is the Modified Julian Date−56000 and is defined as the geocentric Julian Date at the start of the integration, minus 2400000.5 days. The 3$^{\text{rd}}$ and 4$^{\text{th}}$ columns contain the radial velocity and error as computed by **xcsao**.

Table 2.5: Example of barycentric corrected velocities and the associated errors computed by **xcsao** and **fxcor** for Hen2-113 in the wavelength ranges described in Table 2.6. The repeated entries for the same MJD-OBS is because xcsao/fxcor were ran on different sub-regions containing stellar emission features for the same spectrum.

Corrected Velocities						
			xcsao		**fxcor**	
MJD-56000 (d)	Exposure (s)	Wavelength Range Å	RV (km s^{-1})	Error (± km s^{-1})	RV (km s^{-1})	Error (± km s^{-1})
63.8203	1500	4477-4705	-54	2	-54	2
63.8369	900	4477-4705	-54	2	-55	3
63.8698	1200	4477-4705	-54	2	-54	2
64.1222	1500	4477-4705	-28	13	-31	18
64.8012	1500	4477-4705	-63	14	-64	20
69.9965	1500	4477-4705	-53	2	-53	3
105.8911	1500	4477-4705	-46	4	-63	6
106.8011	1500	4477-4705	-15	2	-16	7
108.9281	1800	6736-7050	-52	2	-53	4
109.8133	1500	6064-6372	-54	2	-50	6
109.8133	1500	6736-7050	-53	3	-65	17
111.031	1500	4477-4705	-54	3	-49	3
111.031	1500	5050-5500	-59	2	-54	4

Same for **fxcor** in columns 6 and 7. Some of the errors output by both **xcsao** and **fxcor** are higher than expected and is due to relatively low signal-to-noise ratio in the spectra. The results of the cross-correlation are shown in the following chapter.

Table 2.6: The wavelengths ranges chosen for the cross-correlations of stellar lines. The empty fields ("-") means either no observations were made in that particular wavelength range or not enough spectra available for cross-correlation. See Table A.2 for more details objectwise.

Object	Blue range (Å)	Red range (Å)
Hen2-113	4477-4705 & 5050-5500	6064-6372 & 6736-7050
Hen3-1333	4500-4720 & 4785-5420	6000-6288 & 6734-7057
Hen2-99	4500-5740	6630-7300 & 6000-6490
M1-26	4477-4800	-
NGC5315	4477-4705 & 5050-5500	6000-6250 & 7241-7295
PHR1134-5243	4477-5400	6321-6536 & 6838-7055
SwSt1	4400-4800 & 4477-4705	-

Chapter 3

Results

A combination of spectra of a sample of 7 objects, observed in May, July 2012 and July 2013, have been analyzed and assembled together to create RV versus Julian Date plots. This chapter shows my results plotted sparsely in time and a statistical test which uses χ^2 statistics to calculate the percentage variability for each object. Most of the RV plots shows the results of observations in 2012, except for SwSt1 which contains results from both 2012 and 2013 due to a lack of a sufficient number of spectra. The most prominent stellar emission lines diagnosed for obtaining the mean RV via bisector are summarised in Table 3.1, together with the nebular emission lines. The results from **xcsao** and **fxcor** agree quite well within errors to each other for most objects except for NGC5315. The reason might be that the cross-correlation did not run properly because of the broad line profiles for NGC5315 due to very high stellar wind velocities.

The RVs do not show major periodic variations with large amplitude as we would expect from a proper binary. Also, for an orbital radial velocity variability, one would expect high periodic velocities of the amplitude of the order described in Figure 3.1. None of them show these kind of features, except for Hen2-99 where some hints of periodicity might be seen in the RV plot. A higher resolution follow up is absolutely required for this object. Nevertheless, the non periodic and relatively small amplitude RV shifts from the mean that we actually see in the plots presented in this chapter are most probably due to stochastic wind variability.

Table 3.1 shows the object name in the 1^{st} column, the stellar lines chosen for bisector in the 2^{nd} column. These stellar lines were chosen according to the criteria discussed under subsection 2.2.2 of this thesis and also because these were the most prominent stellar lines in the respective spectra. The observed wavelength of a particular stellar line and its rest wavelength according to NIST website in the 3^{rd} and 4^{th} columns respectively, the mean stellar velocity including the uncertainties given by $xcsao/fxcor$ in column 5, the nebular lines chosen for finding the nebular mean velocities in column 6 and the mean nebular

velocities for each object together with the errors in the 7^{th} column.

Table 3.1: Table shows the stellar and nebular weighted means for each object. The nebular lines' wavelengths are H_α-6563, H_β-4861, H_δ-4101, H_γ-4340, NII-6583 and OIII-4959. The two nebular means for SwSt1 are for two epochs namely June 2012 and July 2013. The mean stellar velocity including the uncertainties are shown as $xcsao/fxcor$ in column 5.

Object	Stellar	λ_{obs} (Å)	λ_{rest} (Å) (NIST)	$\langle \mathrm{RV_{stellar}} \rangle$ (km s^{-1})	Nebular	$\langle$ RV$_{\mathrm{neb}}\rangle$ (km s^{-1})
Hen2-113	CII	4266.41	4267.261	- 51 ± 4 / - 53 ± 3	H_α, H_β, H_δ, H_γ, NII	- 63 ± 2
Hen3-1333	CIII	5695.92	5695.19	- 37 ± 3 / - 37 ± 4	H_α, H_β, H_γ, NII	- 66 ± 10
Hen2-99	CIII	5694.26	5695.19	- 34 ± 14 / - 37 ± 18	H_α, H_β, NII	- 95 ± 13
M1-26	HeI	4470.16	4471.474	- 75 ± 6 / - 72 ± 6	H_β, H_δ, H_γ, OIII	- 26 ± 10
NGC5315	HeI	4469.49	4471.474	- 12 ± 7 / - 51 ± 32	H_α, H_β, H_γ, NII, OIII	- 24 ± 8
PHR1134-5243	CII	4267.66	4267.183	19 ± 5 / 18 ± 16	H_α, H_β, NII	- 66 ± 23
SwSt1	HeI	5875.06	5875.64	- 57 ± 7 / - 35 ± 7	H_α, H_β, H_δ, H_γ, NII, OIII	- 37 ± 3 / - 42 ± 5

Most of the RVs do not show large enough variabilities in the stellar lines as we would expect in a close binary system with a period of $\sim$ 0.2 days and $\sim$ 1.0 day (Miszalski et al. 2011b) and a post-AGB star mass of $0.6M_{\odot}$. Figure 3.1 depicts RVs calculated from Equation 1.7 for such a system with different inclinations.

Also, there is no clear detection of a periodic velocity variation which would provide strong support for binary motion. Thus, wind variability is still a preferred explanation for the observed small variations in the RV.

However, an interesting offset is seen between the nebular and stellar velocities. The reason might be that the lines that are formed in the photosphere are blue shifted due to the wind, like in the case of Of type stars (Crowther et al. 1998a, Mendez et al. 1990).

Since no obvious RV variations are observed in the sample, a statistical test was carried out to look at their probability of variability, based on a null hypothesis discussed in detail by Trumpler & Weaver (1953). These authors recommend a standard χ^2 computation, from the reduced χ^2_{n-1} (where n is the number of observations and n-1 is the number of degrees of freedom) which leads to an estimate of the probability that the star's RV is variable. In summary, lets say the hypothesis to be tested is H : *The semi-amplitude A of a radial velocity variation equals zero.* Then alternatively, the hypothesis is that $A > 0$. The test for H is such that:

1. P_I is the probability of **rejecting** H when H is true (i.e, saying $A > 0$, when $A = 0$). Now, if we set $\alpha = 0.1$ arbitrarily, then in this case, $P_I \leq \alpha$.

2. P_{II} is the probability of **accepting** H when H is false (i.e, saying $A = 0$, when $A > 0$). In this case P_{II} must be a minimum, no matter which orbit. So, maximizing β (where β = 1 - P_{II}, is the probability that the test will reject H when H is false) in the vicinity of $A = 0$.

The compromise consists of allowing the value of β to be at least as large as α. Hence, the criterion for rejection is: reject the hypothesis that $A = 0$ whenever:

$$\frac{1}{\sigma^2}\sum_{j=1}^{n}(x_j - \bar{x})^2 \geq \chi^2_{\alpha,n-1} \tag{3.1}$$

where,

- χ^2_{n-1} is the value of χ^2 given in Table A.1 in the Appendix for $n-1$ degrees of freedom and probability, $P = \alpha$.

- $\bar{x}$ is the stellar mean.

- σ is the standard deviation in the stellar velocities.

- x_j is the individual values for the stellar velocities.

This variability test was run on the 7 objects, assuming the stellar mean is the expected mean and the results are shown in Table 3.2. For each of them, the χ^2_{obs} (the observed

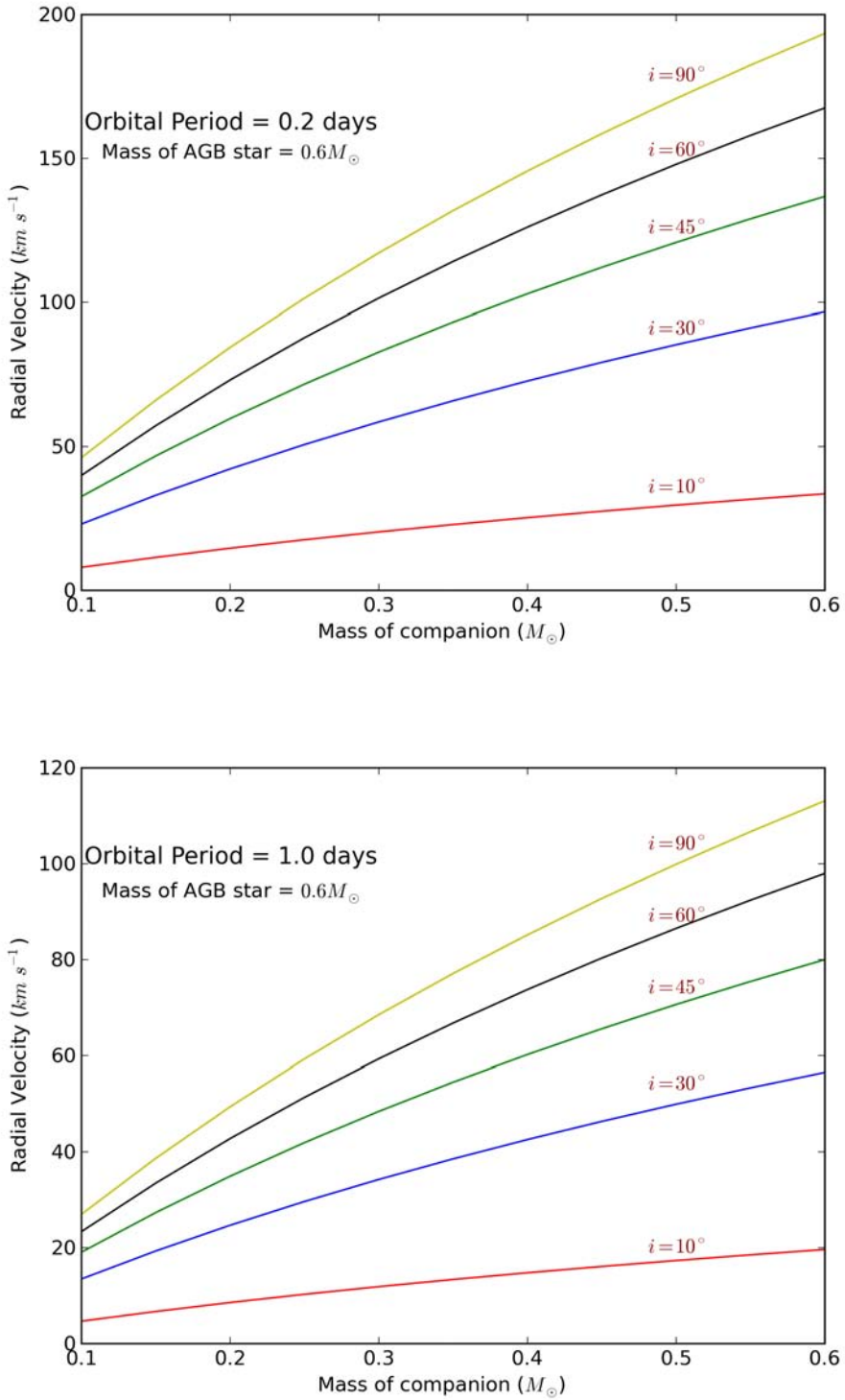

Figure 3.1: **Top**: Radial velocities as we would expect from a binary system containing an AGB star of mass 0.6 $M_\odot$ against different companion mass for different inclinations, assuming a period of 0.2 days. **Bottom**: Radial Velocities as we would expect from the same system but with a period of 1.0 day.

Chi-squared) was computed and the probability that the object is variable $P(\chi^2_{obs} \geq \chi^2_{n-1})$ was obtained using the χ^2 probabilities in Table A.1 (see appendix).

Table 3.2: Results of the variability test carried on individual objects. Column 1 shows the object name, the 2nd column is the number of spectra used (degrees of freedom), the 3rd column is the standard deviation in the velocities, the 4th column is the observed χ^2 and column 5 shows the probability of an object being variable based on its χ^2.

Object	n	σ (km s^{-1})	χ^2_{obs}	$P(\chi^2_{obs} \geq \chi^2_{n-1})$
Hen2-113	20	11.6	20.0	40%
Hen3-1333	26	4.24	26.0	41%
Hen2-99	9	13.11	9.0	35%
M1-26	16	6.68	16.0	38%
NGC5315	8	13.01	8.0	33%
PHR1134-5243	10	5.47	10.0	35%
SwSt1	4	4.87	4.0	26%

Based on the variability test, none of the objects show large enough percentage variability to be called a proper binary and therefore the null hypothesis is rejected at these low probabilities. However, the small variability observed is likely due to small changes in the wind as discussed in section 4.8. The figures below show the cross-correlation results for each object. The stellar mean weighted by the errors (in red) and nebular mean (in blue) RVs are plotted against julian date, together with the standard deviation.

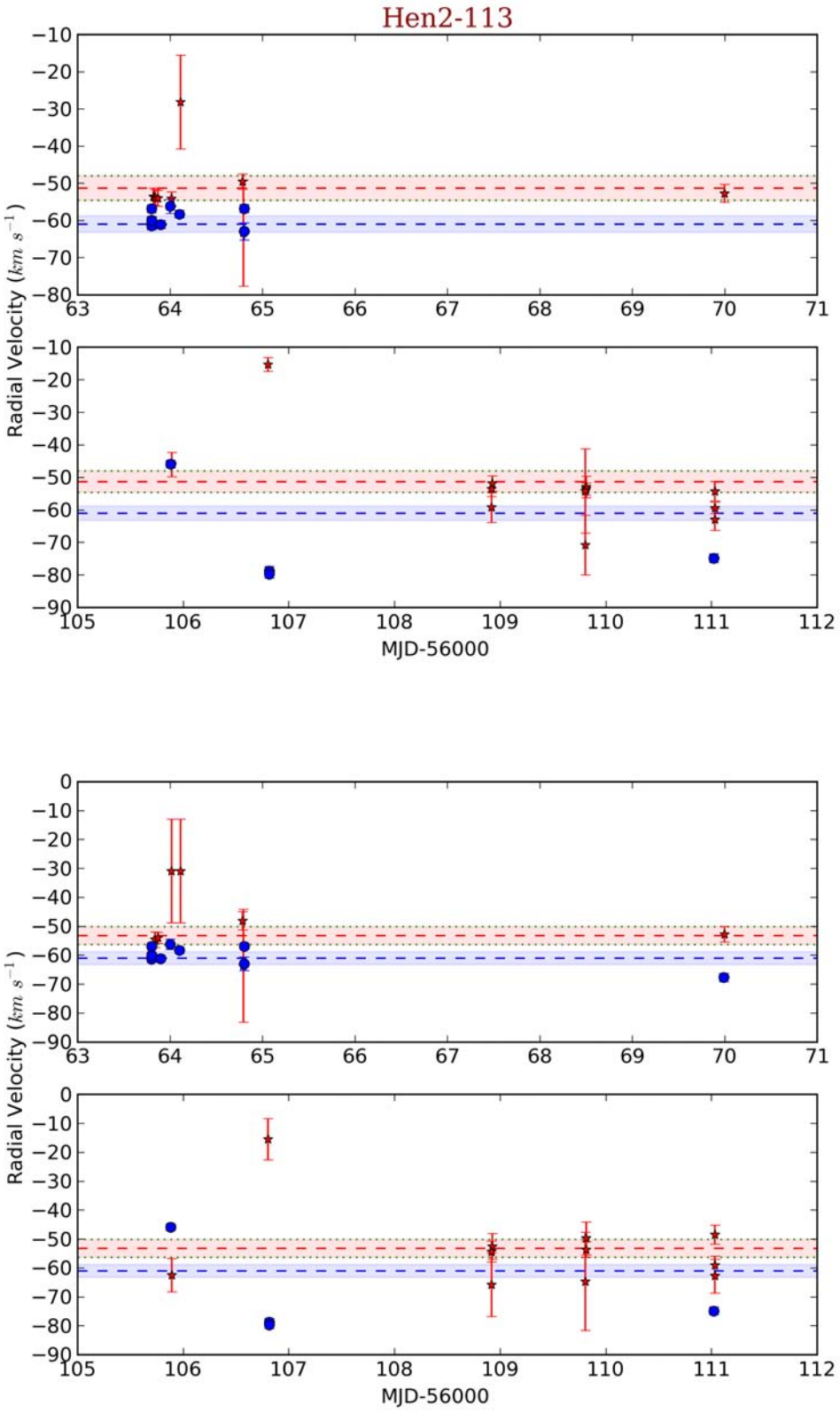

Figure 3.2: **Top**: Hen2-113 xcsao results. **Bottom**: Hen2-113 fxcor results. There is a $\sim$ 5 to 10 km s^{-1} offset between the nebular and stellar velocities and a maximum stellar RV shift of $\sim$ 20-30 km s^{-1} is seen. There is one outlier in the top xcsao panel and two of them around the same MJD-56000 value in the top fxcor panel. These might be the consequence of an imprecise cross-correlation run, due to poor SNR in the spectrum used.

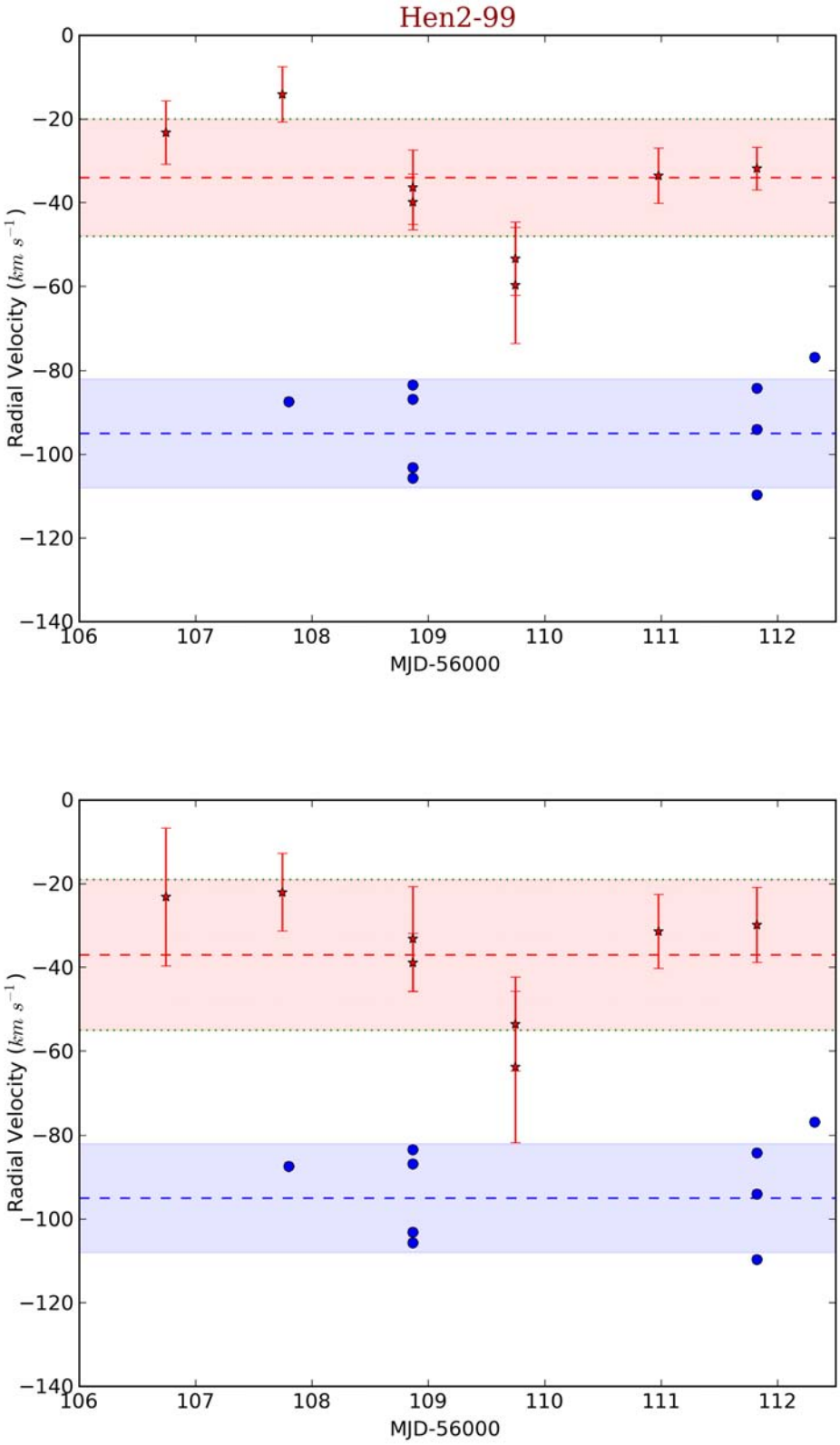

Figure 3.3: **Top**: Hen2-99 xcsao results. **Bottom**: Hen2-99 fxcor results. The offset between nebular and stellar velocities in this object is relatively high ($\sim$ 50 to 60 km s^{-1}). Stellar RV shifts of the order 20-30 km s^{-1} is seen. Moreover, a slight periodicity is observed in the stellar velocities. Higher resolution data is required to confirm the latter.

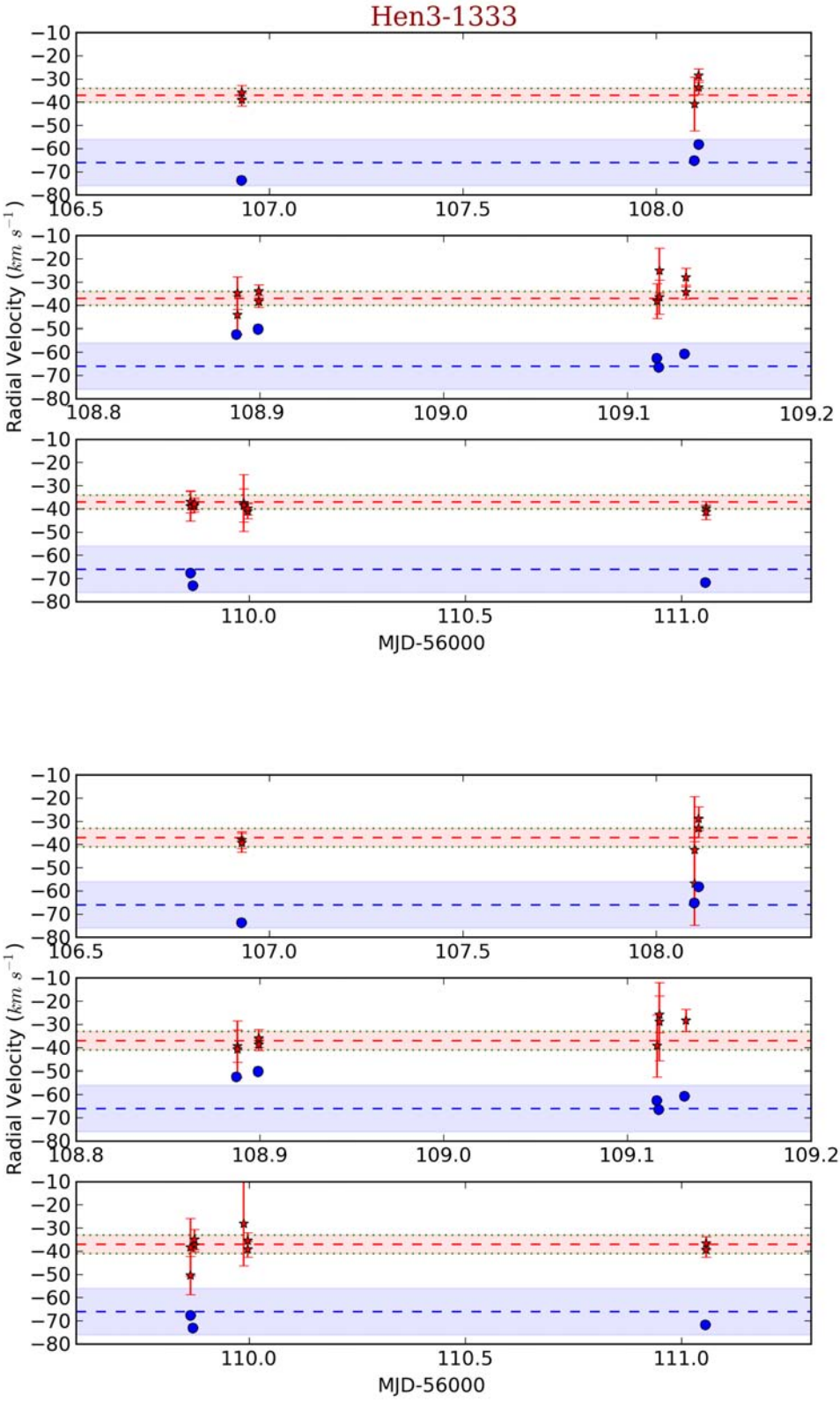

Figure 3.4: **Top**: Hen3-1333 xcsao results. **Bottom**: Hen3-1333 fxcor results. This is one of the objects in the sample which show the least variability, although it is believed by many authors (see discussion) to be a binary candidate, obscured by dust. It has an offset of $\sim$ 30 km s^{-1} between nebular and stellar velocities and the stellar velocities show little RV variations of $\sim$ 5-10 km s^{-1}.

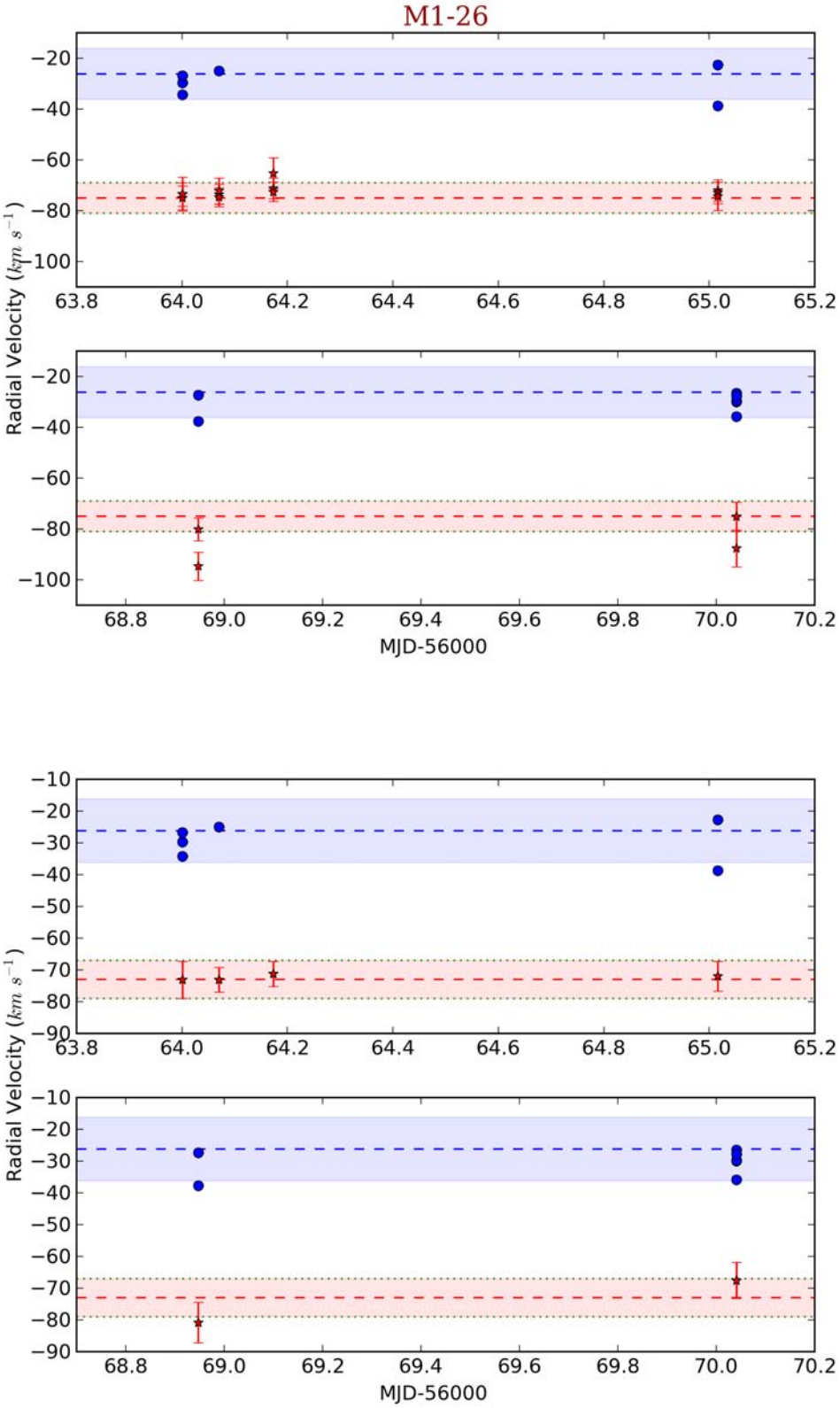

Figure 3.5: **Top**: M1-26 xcsao results. **Bottom**: M1-26 fxcor results. This is another object showing little variations in stellar velocities of $\sim$ 10-15 km s^{-1}. A nebular and stellar offset of $\sim$ 50 km s^{-1} is noticed.

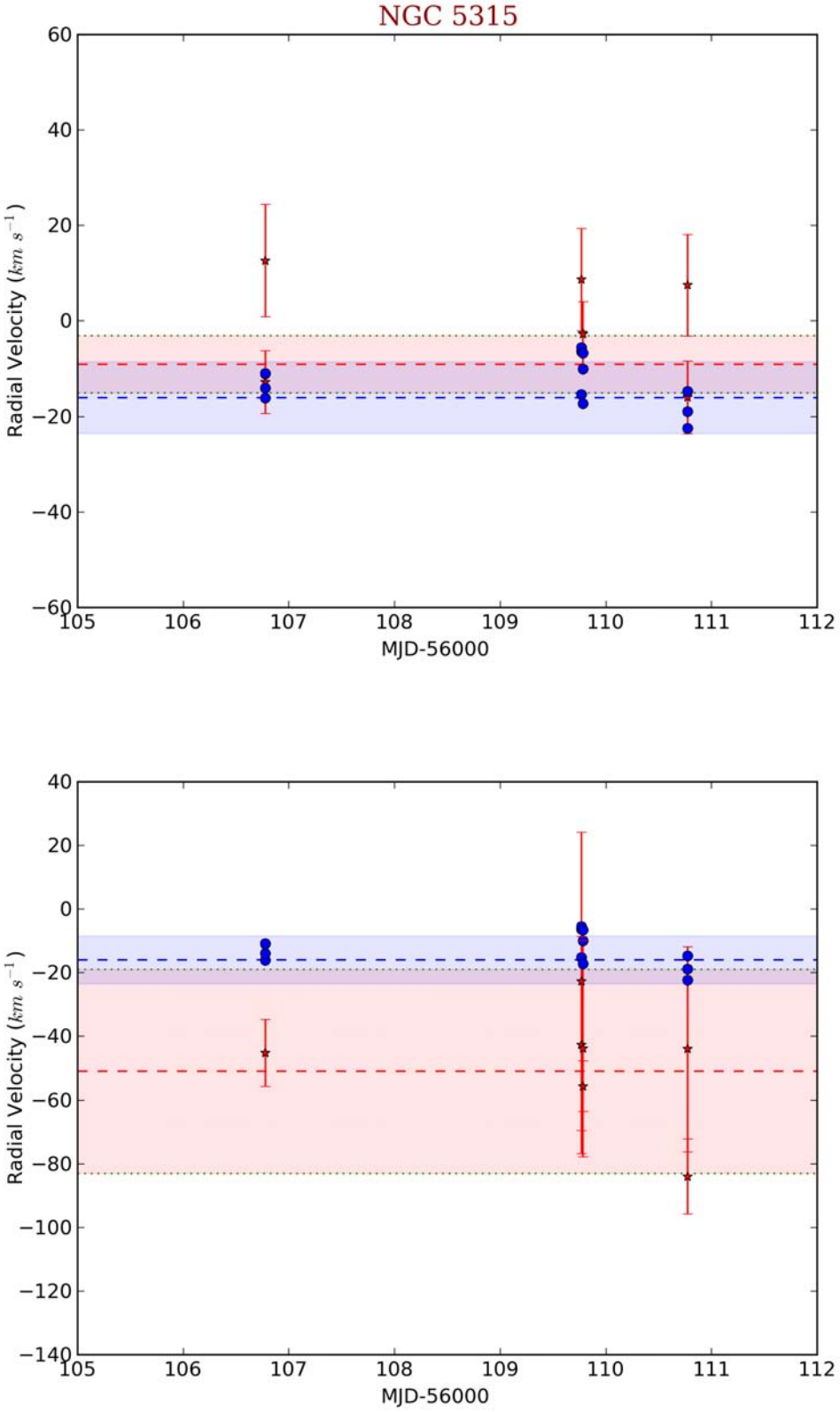

Figure 3.6: **Top**: NGC5315 xcsao results. **Bottom**: NGC5315 fxcor results. The stellar results for NGC5315 show a lot of uncertainties. This is the only object in the sample which contains very broad emission C lines due to very strong stellar winds. There also seem to be a significant difference between the offset between stellar and nebular means, as output by **xcsao** and **fxcor**. The stellar lines show $\sim$ 15-20 km s^{-1} scatter about the weighted mean.

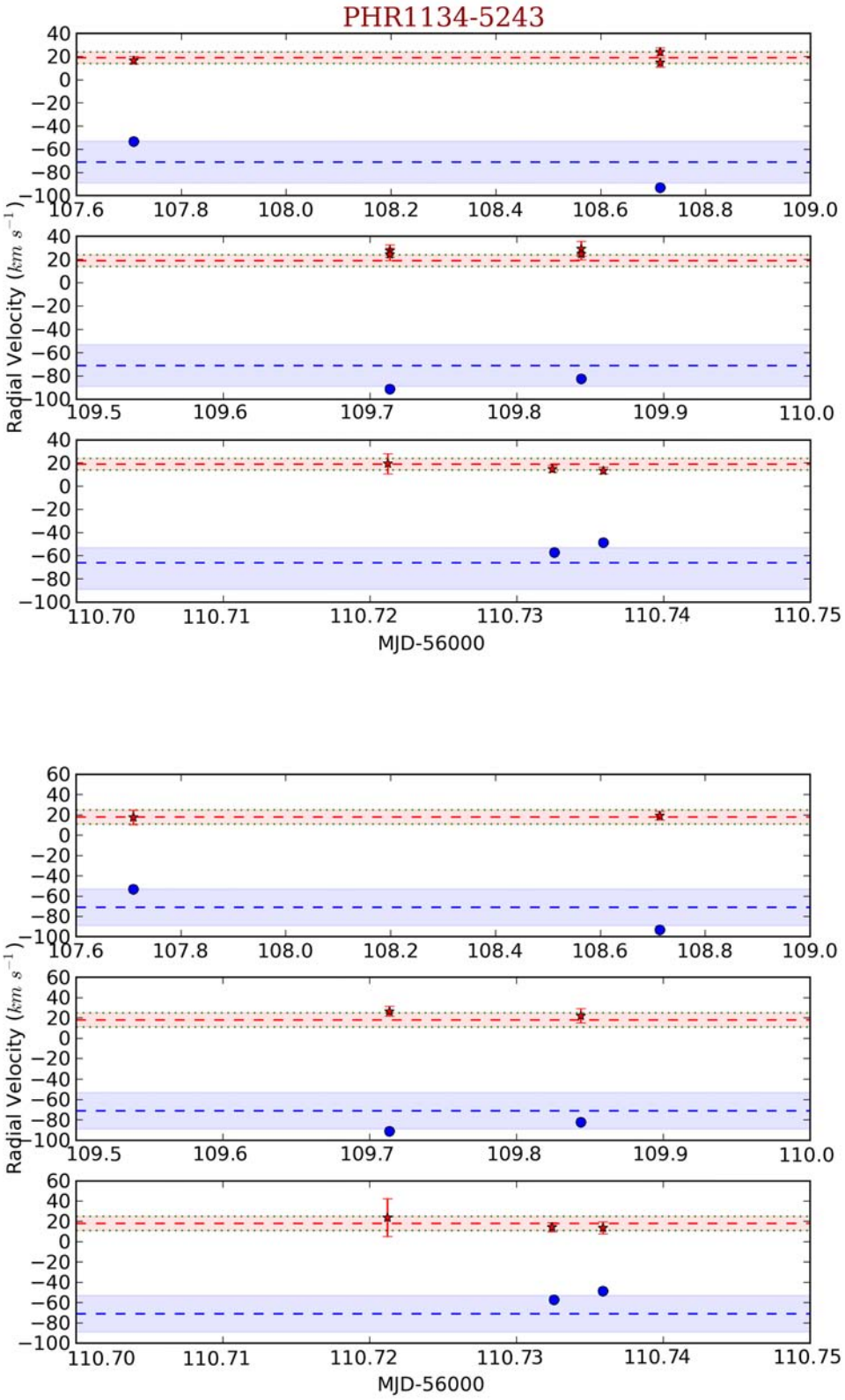

Figure 3.7: **Top**: PHR1134-5243 xcsao results. **Bottom**: PHR1134-5243 fxcor results. One other object showing very little variation in the stellar velocities is PHR1134-5432. The nebular mean and stellar mean show an offset of $\sim$ 50 km s^{-1}. The variations in the stellar RVs are of the order of $\sim$ 5-10 km s^{-1} and seem to be least of the sample.

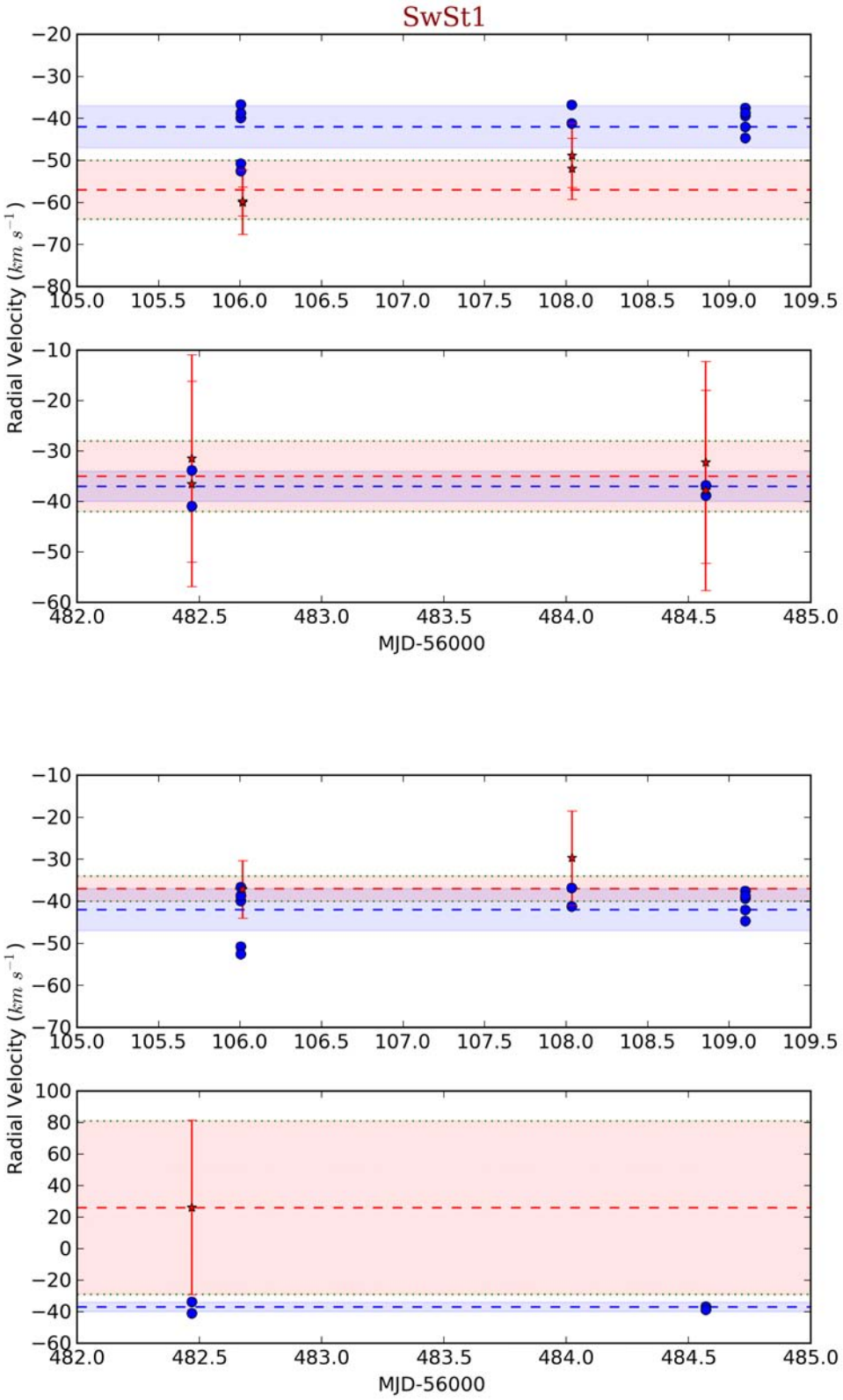

Figure 3.8: **Top**: SwSt1 xcsao results. **Bottom**: SwSt1 fxcor results. This is the only object that I had to include July 2013 data due to very little epochs in 2012. Based on the **xcsao** results (upper two panels) the stellar and nebular offsets seem to be $\sim$ 20 and 5 km s^{-1} in both epochs respectively. However, the scatter in the stellar velocities in July 2013 seem quite high and might be due to the quality of the spectra. The stellar RV shifts are of the order of $\sim$ 10-20 km s^{-1}.

Chapter 4

Review Of Individual Objects & Discussion

There have been many theoretical models which have been proposed to explain the shapes of PNe, e.g. Balick & Frank (2002). Most of the models try to reproduce the velocity fields of the circumstellar material involved in building the general shapes of these PNe, including axisymmetric and more complex ones. The formation of such structures require a binary companion, rotation and/or magnetic fields. This section deals with the different aspects and characteristics of the objects in my sample. In this section, a review of the morphology, type and any other aspect connected to binarity based on previous studies are presented. I also discuss how my results are in accordance with these previous studies.

4.1 Hen2-113

4.1.1 Morphology

Lagadec et al. (2005) reports high-spatial resolution infrared observations of Hen2-113 done with different instruments at ESO and NACO, MIDI, ISAAC, TIMMI in Chile. These observations have revealed new nebular morphologies of Hen2-113.

Hen2-113 is more generally classified as a bipolar shaped nebula with ring structures according to HST observations. This result was confirmed by NACO with more morphological details. The diffuse lobes extend about 2" spatially. It is composed of 2 coaxial rings, with a well defined second ring (ring 2) slightly fainter than ring 1 and incomplete. The central star (CS) is a [WC] type and seems to be slightly offset from the geometrical centers of the rings and also offset from the midpoint of the axis connecting the rings. Moreoever, it appears also to be offset from the midpoint of the line joining the tips of the main NW-SE lobes of the nebula. A small circular region (a hole) is observed at 0.5" to the south-east of the CS, with a diameter of 0.3". Its direction coincides nearly with the orientation of the bipolar nebula surrounding the two rings. hence, geometrical models explain the structure

as being a diabolo-like one (see Figure 4.1) with an inclination of i =37°, PA $\sim$ 65°, n=0.9 and $\frac{a}{c} = \frac{3}{2}$. Where n, a and c are variables of the diabolo given by Equation 4.1.

$$x = a(1+u^2)^n \cos v \tag{4.1}$$

$$y = a(1+u^2)^n \cos v \tag{4.2}$$

$$z = cu \tag{4.3}$$

with $-\frac{\pi}{2} \leq u \leq -\frac{\pi}{2}$ and $-\pi \leq v \leq \pi$.

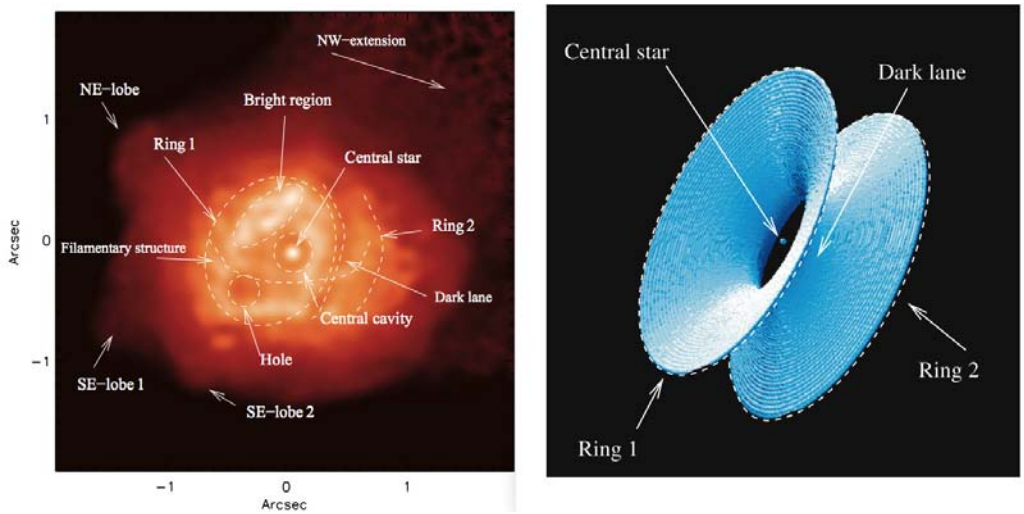

Figure 4.1: **Left:** Infrared image of Hen2-113 with main structures labelled. **Right:**The diabolo structure of Hen2-113 (Lagadec et al. 2005).

Where a controls the radius of the diabolo, c is the height and n is the opening angle. Quite interesting, there have been observations of a few filamentary structures too (Figure 4.1 left), which might be an indication of a possible central binary system or a merged system.

4.1.2 Infrared excess

The observed flux from the CS in the NACO L$^{'}$ (green) and M$^{'}$ (red) bands is about $\sim$ 300 and $\sim$ 800 times more, respectively, than that we should be expecting from a modelled CS. The Infrared excess is best explained by dust emission very close to the CS. For this kind of emission, we theoretically need temperatures of $\sim$ 900-1000 K with a mass of $\sim 10^{-9} M_{\odot}$.

4.1.3 PAHs

From the Infrared observations, Lagadec et al. (2005) studied the spatial distribution of Polycyclic Aromatic Hydrocarbon (PAH) in the system, since the main nebula of Hen2-113 is known for displaying PAH features. Observations from ISAAC shows that PAHs seem

to have broader spatial distribution than the grains producing the continuum emission and therefore, Lagadec et al. (2005) believe that the PAHs have formed before the dust grains. Moreover, the presence of a dual chemistry (which might be a result of mergers) in this system is still being debated. Longer wavelength observations (>15 μm), where O-rich dust will be detected is needed to compare the PAHs and O-rich dust distribution. The mass fractions found in the CS of H:He:C:O are 0:34:54:13 (De Marco & Crowther 1998). The presence of C-O together might make this object a suspectful binary candidate, whereas, my results only show a 40% probability of it being variable.

4.2 Hen2-99

4.2.1 Overview

Hen2-99 is a PN with a size of $\sim$ 15" and with a CS classified as [WO4] by Leuenhagen et al. (1996) and as a [WC9] by Acker & Neiner (2003b). It is at a Shklovsky distance of 2.4 kpc (Pottasch & Zijlstra 1992) and the CS temperature is $\sim$ 49 kK. The velocity derived from the broadening of the emission lines are 1000-2000 $km\ s^{-1}$ and 700-1000 $km\ s^{-1}$ in the UV and optical, respectively.

4.2.2 X-ray morphology

The X-ray luminosity of this object is found to be the smallest of all known PNe detected in X-rays (Soker & Kastner 2003a;b). The non detection of X-rays would suggest that the fast wind from the central star has yet to collide with the ionized ejecta or the X-ray emission produced from shocks might be faded away (Montez et al. 2005). However, the X-ray morphology suggests that the former interpretation might be more plausible, due to a lack of well defined inner rims.

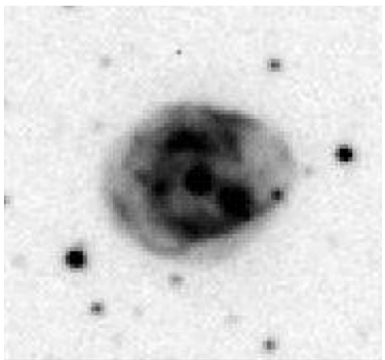

Figure 4.2: Hen2-99, observed at the 1.0m telescope in Sutherland. Image Credit: B. Miszalski.

4.2.3 Discussion

According to the results obtained in this thesis, the variability of Hen2-99 is $\sim$ 35% probable. Based on some periodic variations seen in the RV plot for Hen2-99 we can't rule out completely a non-binary CS. However, the errors in the RVs are larger than expected and higher resolution spectra will divulge more about this object.

4.3 Hen3-1333

4.3.1 Overview

Hen3-1333 is classified as a [WC10] type CS by Acker & Neiner (2003a). De Marco & Crowther (1998) reports a temperature of T_{eff} = 30 kK, v_{∞} = 225 $km\ s^{-1}$ and a high mass-loss rate of $\dot{M} = 4 \times 10^{-6}\ M_{\odot}\ yr^{-1}$. Its mass fractions of H:He:C:O are 0:34:52:14 (De Marco & Crowther 1998).

A dusty disk with inner radius of 97 $\pm$ 11 AU is reported from VLTI observations by De Marco et al. (2002), Chesneau et al. (2006). One of the clues for it being a merged system if not a binary, might be the presence of a dust disk composed of a dual dust chemistry (C and O rich) (Cohen et al. 2002). The dual dust might be the case of the merging of C-O white-dwarf pair.

4.3.2 Morphology

The most prominent structure of Hen3-1333 is the North lobe which seems to be composed of three distinct ejections (Fig. 4.3). It is more of a multilobal structure with a complex filamentary extension at PA of 170°. Chesneau et al. (2006) has described two dark internal structures as lanes, forming a conical structure. These lanes might be part of a globally bipolar shape of Hen3-1333, since these two delimits two areas. Chesneau et al. (2006) have reported bow shock structures as well located $\sim$ 0.5" east from the CSPN, which might be results of wind interaction with the ejecta.

For an assumed period of $\sim$ 5 years for the CS, a primary of mass 0.6 $M_{\odot}$ and secondary of mass 0.4 $M_{\odot}$ would have a maximum orbital separation of $\sim$ 13 $\pm$ 2 AU (Miszalski et al. 2011c). This object shows obscuring events with a lack of strong periodic repeatability and the latter radius is far too small to explain the fading events, as argued by Miszalski et al. (2011c). Based on the above arguments and my result with a 41% chance of Hen3-1333 being a close-binary, we cannot rule out completely a binary CS of Hen3-1333.

Another possibility is that both of the relatively similar objects in the sample, i.e. Hen2-113 and Hen3-1333 contain a wide binary CS. It could be that a close binary does not allow for a disk to form or be stable enough to last. In addition to this, the detection of an edge-on disk near the CS of Hen2-113 reported by De Marco et al. (2002), together with a low percentage variability CS for both of the above mentioned objects, gives more evidence of a wide binary CS.

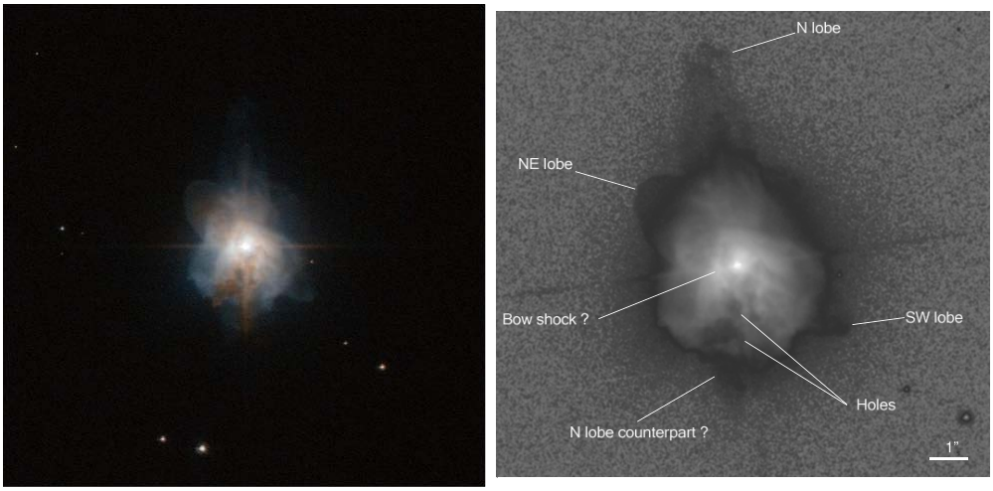

Figure 4.3: **left**: HST image of Hen3-1333 from the PNIC catalogue by Balick (2007). **Right**: Sketch of the HST nebula showing the remarkable structures (Chesneau et al. 2006).

4.4 M1-26

4.4.1 Overview

M1-26 is a PN that is comprised of a bright round shell surrounded by many loops and arcs (Fig. 4.4). M1-26 is believed to be a proto-planetary nebula. The intensity ratio of [OIII] $\lambda 5007/H_\beta$ is found to be ~ 0.1 in 1968-70 by Vorontsov-Veliaminov et al. (1975) and later in 1977-78 it was found to be ~ 0.4 by Kohoutek & Martin (1981). Interestingly, this PN seems to have a CS which is in an evolutionary stage, based on the secular increase in the [OIII] flux between these two period of times. Such an increase is very likely produced by an increased excitation in the central star of M1-26 (Hutsemekers & Surdej 1985).

My results shows a $\sim 38\%$ probability of its CS being variable. Looking at the overall aspherical morphology, including filament like structures, one might suggest a possible binary or merged system.

4.5 PHR1134-5243

4.5.1 Overview

PHR1134-5243 also designated as PMR 2 by Morgan et al. (2001) has a late type [WC] central star which is either an intermediate class between [WC9] and [WC10] or more of a [WC10] class. Based on the CIV 5808/CIII 5696 ratio which is - 0.8 places it nearer to [WC10], while the ratio of CIV 5808/CII 4267, which is - 0.13 places it nearer to the [WC9] class. Its CS differs with others in the sense that it is the earliest of the late [WC] types to show nitrogen lines in its spectrum. The derived distance according to the absolute magnitude is 15 kpc which gives a diameter of 2.2 pc, but these numbers are still quite

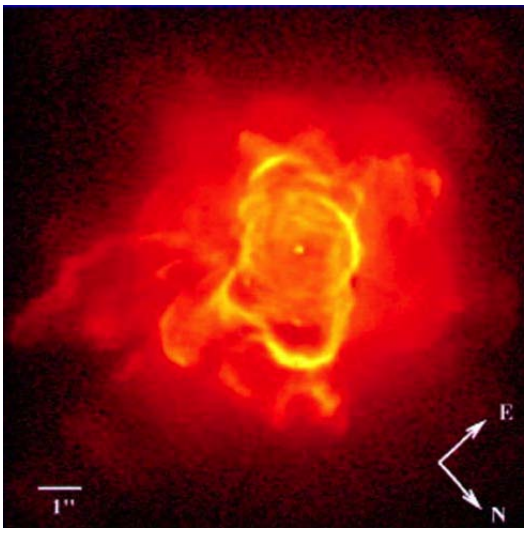

Figure 4.4: M1-26 showing multiple loops and arc structures (Sahai et al. 2011).

uncertain as pointed out by (Morgan et al. 2001).

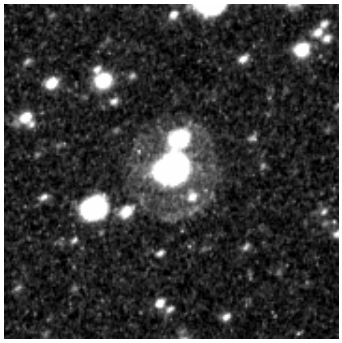

Figure 4.5: Image of Central star of PHR1134-5243 and the surrounding faint circular nebula. Image credit: SuperCOSMOS H_α survey (Parker et al. 2005).

RV studies of 10 spectra of this object showed no significant variation in the stellar velocities and a probability of $\sim 35\%$ of variability was obtained via χ^2. This low probability would most probably rule out a central binary star of PHR-1134-5243 for the moment based on the quality of my data. Higher resolution data are required before any further judgements can be made regarding the binary status of the CS of PHR1134-5243.

4.6 NGC5315

4.6.1 Overview

NGC5315 is classified as a [WC4] central star by Crowther et al. (1998b). The PN is a compact one almost spherical (slightly elliptical) and with diameter of ~ 4" (Fig. 4.6). The

terminal velocity obtained by Feibelman (1998) via the P Cygni profile is 3600 $km\ s^{-1}$ and a temperature of $T_* = 80000$ K. However, Pottasch et al. (2002) obtained a temperature of 66000 K for the CS. The heliocentric radial velocities derived for this object based on the He I 4471 line was - 12 ± 7 $km\ s^{-1}$ from **xcsao** and - 51 ± 32 $km\ s^{-1}$ from **fxcor**. On the other hand, Peimbert et al. (2004) derived a heliocentric radial velocity of 39 ± 0.1 $km\ s^{-1}$ based on the same line. The discrepancy might be due to our data quality due to the fact that I got quite large uncertainties for the RVs for this object.

Figure 4.6: An HST image of NGC5315 showing a rather complex nebular morphology with broken ring structures (Image credit: NASA, ESA and The Hubble Heritage Team (STScI/AURA)).

4.6.2 Discussion

Based on 8 spectra for this object we found that the RV variability is only ∼ 33%. This is the only object in which **xcsao** and **fxcor** outputs showed quite different values for the stellar RVs. The only difference I can think of between NGC5315 and the other objects studied is that the stellar emission lines are relatively broader in NGC5315. It might be that the cross-correlation softwares had difficulties in dealing with the broad stellar lines and therefore introducing extra errors in the RV. Definitely, higher SNR data and more epochs are needed to be really able to run a proper cross-correlation analysis on this object.

4.7 SwSt1

4.7.1 Overview

The CS of SwSt1 is classified as [WC9] by both Acker & Neiner (2003a) and Leuenhagen (1997). The adopted distance by De Marco et al. (2001) to this PN is 2 kpc. The temperature of the CS is $T_{eff} \leq$ 40000K. Guerrero & De Marco (2013) report variations in the P Cygni profile. Several CSPNe that have similar stellar and wind properties as those having variable

P Cygni profiles, do not show much variability (Guerrero & De Marco 2013). According to my results from only 4 spectra for this object, the CS has $\sim$ 26% chance of being variable, which is very low and in fact the lowest in my sample.

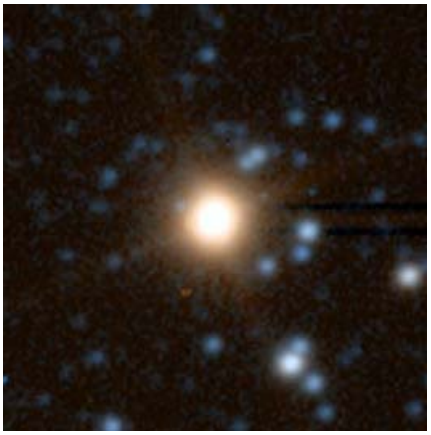

Figure 4.7: An image of SwSt1 taken from the PNIC catalogue by Balick (2007).

The CS appears to have not changed significantly over the last 100 years. However, De Marco et al. (2001) suggests that the CS of SwSt1 has recently transited to the AGB and that the H-deficiency in this object has occurred in the last century.

4.8 Possible explanations

4.8.1 Magnetic fields

Magnetic fields are often overlooked when it comes to global shaping of the PN. Soker (2006) provides argument with physical demonstration, which explains why large scale magnetic fields cannot play a dominant role in global shaping of PNe. However, they might still shape the PN at local physical scales which is much shorter than the PN size itself. Moreover, Nordhaus & Blackman (2006) argue that the launching and shaping of the outflow could occur close to the central core and therefore, the action of magnetic fields at large scales are very less significant. In order that large scale structure are shaped by magnetic fields, it requires that the magnetic fields act at large scales.

Using the fact that single AGB stars cannot sustain large scale magnetic fields for long enough to globally shape the PNe (Soker 2006), it requires that the CSPNe are binaries to be able to explain the more complex PNe shapes. We notice that many nebulae around [WR] CSPNe show jets and filament like structures which is undoubtedly due to a companion as mentioned in section 1.5.1 or a combination of a companion and magnetic fields.

4.8.2 Mergers

One of the other explanation might be that mergers are the main reasons behind producing these [WR] CSPNe. To complement the latter statement, a recent work by Soker (2013) describes a merger scenario being a common outcome of the CE evolution of AGB and red supergiants stars with an envelope to secondary mass ratio of $M_{env}/M_2 \geq 5$ (M_{env} = mass of the envelope at the beginning of the CE phase). Ivanova & Podsiadlowski (2003) mention the types of mergers in a close binary system after the CE, namely the quiet merger, the moderate merger and the explosive merger. Ivanova & Podsiadlowski (2003) also discuss that the resulting envelope composition of a given type of merger strongly depends on the type of merger. It might be that [WR] CSPNe mergers form part of one of these types and the resultant composition is determined by the compositions of the primary and secondary. hypothesis

On the other hand, Soker (2013) describes some observations which might be explained by mergers at the termination of the CE phase which include:

- The core degenerate scenario for Type Ia supernovae (e.g, Sparks & Stecher (1974)).
- R Coronae Borealis stars with a massive expanding shell (e.g, Clayton et al. (2011)).
- The bright end of the PN luminosity function (e.g, Ciardullo (2012)).
- The formation of single sDB stars (e.g, Geier et al. (2011)).
- Ultraluminous core collapse SNe (e.g, Chomiuk et al. (2011)).
- Complicated nebular morphologies of PNe. Soker (2013) especially mentions NGC 5189 here which has a [WO1] type CS (e.g, Sabin et al. (2012)).
- Missing long-orbital period post-CE binaries (e.g, Rebassa-Mansergas et al. (2012))

One other phenomenon can be added to the above presented list which is [WR] CSPNe (Private discussion with Prof. Noam Soker). De Marco & Soker (2002) reviewed the formation of a [WR] CSPN. The argument in De Marco & Soker (2002) is that the main requirement for any [WC] CS scenario, which is to turn an O-rich AGB star into a C-rich star and then into a H-deficient post-AGB star (a [WC] CS) in a relatively short period of time, is extra mixing between the core and envelope material. In this manner, the O-rich dust is still contained close to the [WC] CS. According to De Marco & Soker (2002) this sequence can be triggered by two processes,

1. Either, a low mass companion to the AGB star loses angular momentum, enters its envelope and eventually spirals in.
2. Or, extra mixing of intershell material with the envelope material.

De Marco & Soker (2002) propose the merging of a low mass companion (low mass; higher chance of merging (De Marco 2009)), $0.001 M_{\odot} \leq M_2 \leq 0.1 M_{\odot}$ and the core to produce the

[WC] CS. The companion enhances mass loss rate, then gets destroyed as its dense material collides with the core and forms an accretion disk. Similar to the nova scenario of Rosner et al. (2001), the accretion disk causes extra mixing between the core and envelope turning the star to a C-rich and the H-deficient, giving the central star a [WC] signature. The best target to study and subsequently test the binary status via RV variability would probably be NGC 5189 (Sabin et al. 2012). Future works related to this topic on NGC5189 are discussed in section 6.

4.8.3 Wide binaries

Nevertheless, another possibility could be that the CS contain a system of three components where two are very close to each other and the third is a wide binary, for e.g, A 63 (De Marco 2009). In such a case, we need much better resolution than presented in this thesis to be able to detect the very small orbital motions for the wider component. It is to be noted that, a merger hypothesis is being postulated to be responsible for producing these [WR] CSPNe and there might be other preferred explanations to the [WR] phenomenon in CSPNe. A better confirmation of the merger hypothesis will be with higher resolution data and modelling as part of the future work related to this thesis.

Chapter 5

Conclusion

A sample of 7 [WR] CSPNe are studied in this thesis to investigate their binary status via RV monitoring for the first time. The spectra were gathered mostly in May and June 2012, with some of them in July 2013 at the SAAO 1.9m Telescope in Sutherland. A cross-correlation method was used for the analysis as described by Foellmi et al. (2003a) and radial velocity shifts were computed using the IRAF task **xcsao**.

None of the CS showed high enough amplitude RV variations for them to be classified as a close-binary system. Moreover, none of them display a periodic variability in the RV. However, Hen2-99 could possibly exhibit coherent RV variability and therefore this object could be tagged as one which needs more in-depth studies in search of a close-binary CS. It might also be that the RV sensitivity presented in this thesis is not good enough and there is a need of more epochs to better probe the binary status of Hen2-99.

Still, it can be argued that if there was a close-binary companion in any of the systems, a high enough RV amplitude would have been detected, given the SNR in the spectra. Some of the possible explanations of what these systems might be composed of, are given in section 4.8 of this thesis, where possible factors like magnetic fields, mergers and wide binaries have been discussed. Mergers might still be the preferred mechanism in producing these [WR] CSPNe, but it is difficult to prove this statement. The reason is that we do not know currently what are the features or signatures to look at in these systems if they were to be produced by mergers.

Moreover, another possibility can be that the systems have very eccentric orbits with periods of the order of 10 to 20 days and we managed to observe them over a fraction of the full phase. Therefore, it is essential for the future of this work to have high SNR and higher resolution data monitored over a longer time period with e.g. the High Resolution Spectrograph (HRS) on SALT. Higher resolution data would also be useful in case these systems contain wide binaries, where the companion will have a long orbital period and better spectral resolution would be required to track the slow kinematics of the orbital companion.

Undoubtedly, the sample needs to be increased considerably if we want to improve the

statistics regarding the close-binary fraction of about 10% to 20% and it might be hard to put constraints on what fraction of these are actually [WR] CSPNe because the latter are very rare objects.

Several promising objects are available (e.g NGC5189), but they are quite faint and would need larger telescope data for follow-ups. Furthermore, the RV study of systems showing jets and filament-like structures (e.g NGC5189), which are believed to be strongly connected to a binary CS should be pursued.

Chapter 6

Future outlook

6.1 Higher resolution spectra

The objects in my sample are to date not very well constrained as far as the binary properties are concerned. Spectroscopic analysis and RV monitoring carried out in this thesis can be used as a first step toward a more in depth [WR] CSPNe binary search. For a better census of binaries we undoubtedly rely on bigger samples of [WR] CSPNe where high resolution RV monitoring is conducted.

There are two of the very interesting [WR] CSPN, namely PHR0654-1045 (Hajduk et al. 2010) and NGC 5189 (Sabin et al. 2012), which are thought to be possible binaries. An extension of this thesis is conducting high resolution RV monitoring of these two objects via SALT spectroscopy. These are already in the observing queue as part of our 2014 observing programs and we hope to better constrain their binary status.

6.2 Radio observations

It would be very helpful to observe the objects presented in this thesis at radio wavelengths to measure the strength of the non-thermal synchrotron emission (e.g, section 1.3.1). A radio spectral energy distribution (SED) can be fit and depending on the spectral indices mentioned by, for e.g. Dougherty & Williams (2000), we would be able to infer the type of radio emission (Thermal, Non-thermal or a combination of both). However, one of the problems at present is the angular resolution we need to be able to probe the CS of the order of $\sim$ 0.3" - 1.0". We rely on VLBI observations of these objects to achieve such resolutions. Upcoming instruments like MeerKAT would not be able to achieve sub-arcsecond resolution, but from the spectral index of the SED we would still be able to distinguish non-thermal from thermal emission even if the [WR] CS is not resolved.

The radio emission from these systems could be a mixture of that of the nebula and the central star. Therefore, dissociating the central star flux from the nebula could be another challenge, keeping in mind that the flux from the nebula itself might be a mixture

of thermal and non-thermal. A 20GHz survey carried out by Chhetri et al. (2013), with angular resolution of ~ 0.5", contained a total of 33 PNe having a rather flat SED with α between -0.39 and $+1.6$. Clearly, the results from this study shows that these are thermal sources. A follow-up of sources with steeper spectral indices ($\alpha \leq -0.5$) would reveal non-thermal emission and such detections might suggest interesting phenomena like shocks between hot fast moving winds from the CS and cooler slow moving gas from the nebula. These CSs could therefore be tagged and studied more in depth in search of a binary system.

Futhermore, one other advantage of radio observations is that in the case of wide binaries, they have a greater chance to be detected in the radio simultaneously, whereas in the optical, high resolution RV studies are needed on different epochs throughout the year(s).

Radio observations would certainly facilitate this survey a lot (for a bigger sample) by flagging those objects which show non-thermal emission and subsequently carrying out a RV monitoring especially on the suspected binary candidates.

6.3 X-ray observations

Guerrero (2012) discussed how X-ray observations of [WR] CSPNe can be used in the search for binaries. The stellar winds in a binary CS can produce shocks and produce shock-heated plasma. The X-ray emission from such systems is described as hard X-rays, with high plasma temperatures $\sim 10^7$ K. Strong variability on orbital period time scales is observed in the X-ray emission (Gosset et al. 2009). Kastner et al. (2012) describes that hard X-ray excess in CSPNe might suggest a binary CS. The Chandra Planetary Nebulae Survey (ChanPlaNs) is a good tool which can be used for the detection of hard X-ray excess in these [WR] CSPNe. Kastner et al. (2012) argue that hard X-ray point sources like NGC 7293 and PG 1159 stars might be strong binary candidates in analogy to symbiotic binaries and cataclysmic variables. Moreover, accretion of material onto a compact object is a very powerful mechanism to produce hard X-rays (Kastner et al. 2003). These objects can be studied in the X-ray and a search for stellar wind accretion can be done.

6.4 Modelling

6.4.1 Orbital modelling

Other additional work that can be done in this field is binary orbit modelling as outlined by Wilson (1979), where binary star velocity curves including effects of eccentricity and nonsynchronous rotation are computed. A close-binary model for e.g β Lyr, V356 Sgr and U Cep is also mentioned by them. These models can be extended to any close-binary system (if found via higher resolution data) in the sample presented in this thesis.

If any close-binary system is found in these systems of [WR] CSPNe, orbital modelling will allow us to find the mass of the components and thereafter understand the nucleosynthetic history of the PNe. Notably, no previous Keplerian mass estimates of [WR] CSPNe

have been carried out and presented in the literature. Keplerian orbits can be fitted to any close-binaries found, as described by Joergens et al. (2010), where they derive orbital solutions for Cha Hα and obtain mass estimates of the binary stars via RV monitoring.

6.4.2 Nebular kinematic modelling

Detailed spatio-kinematical models, e.g Huckvale et al. (2013), could be carried out, modelling the [OIII]5007 Å emission line to obtain nebular structure around the [WR] CSPNe. Additionaly, searching for any kind of bipolar structures in the systems and how aligned are the nebular shells to the binary orbital inclinations. If they are strongly aligned that would give a strong indication of binarity (Huckvale et al. 2013). Another similar work by Jones et al. (2011) shows how the morphologies of PNe can be modelled and see whether the nebular axis of symmetry and the binary orbital plane are perpendicular to each other. Jones et al. (2011) claim that all the objects in their sample have satisfied this expectation which implies that the nebula around the CS has been shaped/ejected due to a central binary star system.

Appendix A

Appendix

Table A.1: Table for reading off the probability ($P(\chi^2_{obs} \geq \chi^2_{n-1})$) of variation, given the number of degrees of freedom $n-1$ and the χ^2. Column 1 showing the number of degrees of freedom and the rest of the columns are the probabilities for a given χ^2 value.

d.f.	0.995	0.99	0.975	0.95	0.9	0.75	0.5	0.25	0.1	0.05	0.025	0.01	0.005
1	0	0.0002	0.001	0.0039	0.0158	0.1015	0.4549	1.3233	2.7055	3.8415	5.0239	6.6349	7.8794
2	0.01	0.0201	0.0506	0.1026	0.2107	0.5754	1.3863	2.7726	4.6052	5.9915	7.3778	9.2104	10.5965
3	0.0717	0.1148	0.2158	0.3518	0.5844	1.2125	2.366	4.1083	6.2514	7.8147	9.3484	11.3449	12.8381
4	0.207	0.2971	0.4844	0.7107	1.0636	1.9226	3.3567	5.3853	7.7794	9.4877	11.1433	13.2767	14.8602
5	0.4118	0.5543	0.8312	1.1455	1.6103	2.6746	4.3515	6.6257	9.2363	11.0705	12.8325	15.0863	16.7496
6	0.6757	0.8721	1.2373	1.6354	2.2041	3.4546	5.3481	7.8408	10.6446	12.5916	14.4494	16.8119	18.5475
7	0.9893	1.239	1.6899	2.1673	2.8331	4.2549	6.3458	9.0371	12.017	14.0671	16.0128	18.4753	20.2777
8	1.3444	1.6465	2.1797	2.7326	3.4895	5.0706	7.3441	10.2189	13.3616	15.5073	17.5345	20.0902	21.9549
9	1.7349	2.0879	2.7004	3.3251	4.1682	5.8988	8.3428	11.3887	14.6837	16.919	19.0228	21.666	23.5893
10	2.156	2.558	3.247	3.94	4.865	6.737	9.342	12.549	15.987	18.307	20.483	23.209	25.188
11	2.603	3.053	3.816	4.575	5.578	7.584	10.341	13.701	17.275	19.675	21.92	24.725	26.757
12	3.074	3.571	4.404	5.226	6.304	8.438	11.34	14.845	18.549	21.026	23.337	26.217	28.3
13	3.565	4.107	5.009	5.892	7.041	9.299	12.34	15.984	19.812	22.362	24.736	27.688	29.819
14	4.075	4.66	5.629	6.571	7.79	10.165	13.339	17.117	21.064	23.685	26.119	29.141	31.319
15	4.601	5.229	6.262	7.261	8.547	11.037	14.339	18.245	22.307	24.996	27.488	30.578	32.801
16	5.142	5.812	6.908	7.962	9.312	11.912	15.338	19.369	23.542	26.296	28.845	32	34.267
17	5.697	6.408	7.564	8.672	10.085	12.792	16.338	20.489	24.769	27.587	30.191	33.409	35.718
18	6.265	7.015	8.231	9.39	10.865	13.675	17.338	21.605	25.989	28.869	31.526	34.805	37.156
19	6.844	7.633	8.907	10.117	11.651	14.562	18.338	22.718	27.204	30.144	32.852	36.191	38.582
20	7.434	8.26	9.591	10.851	12.443	15.452	19.337	23.828	28.412	31.41	34.17	37.566	39.997
21	8.034	8.897	10.283	11.591	13.24	16.344	20.337	24.935	29.615	32.671	35.479	38.932	41.401
22	8.643	9.542	10.982	12.338	14.041	17.24	21.337	26.039	30.813	33.924	36.781	40.289	42.796
23	9.26	10.196	11.689	13.091	14.848	18.137	22.337	27.141	32.007	35.172	38.076	41.638	44.181
24	9.886	10.856	12.401	13.848	15.659	19.037	23.337	28.241	33.196	36.415	39.364	42.98	45.558
25	10.52	11.524	13.12	14.611	16.473	19.939	24.337	29.339	34.382	37.652	40.646	44.314	46.928
26	11.16	12.198	13.844	15.379	17.292	20.843	25.336	30.435	35.563	38.885	41.923	45.642	48.29

Table A.2: Log of observations. Note that the "-" in the SNR column refers to the spectra which had an average S/N $\lesssim$ 20 and were not included in the template construction, but still used as a spectrum for cross-correlation. The MJD-OBS is given as mid-exposure value.

Object	MJD-OBS (Mid-exposure)	Date	Exposure (s)	Grating	Wavelength (Å)	Dispersion (Åpix^{-1})	⟨SNR⟩	xcsao/fxcor region (Å)	Resolution (FWHM) Å
Hen2-113	56063.82035	05/16/2012	300	4	4260-5115	0.49	25	4477-4705	1.5
	56063.83688	05/16/2012	900	4	4257-5115	0.49	50	4477-4705	1.1
	56063.86802	05/16/2012	900	4	4257-5115	0.49	28	4477-4705	1.1
	56064.01707	05/16/2012	1200	4	4257-5115	0.49	48	4477-4705	1.3
	56064.11372	05/17/2012	30	4	4257-5115	0.49	-	4477-4705	1.3
	56064.78409	05/17/2012	1500	4	4257-5115	0.49	31	4477-4705	1.3
	56064.79268	05/17/2012	30	4	4257-5116	0.49	-	4477-4705	1.3
	56069.99648	05/17/2012	1500	4	4257-5117	0.49	30	4477-4705	1.3
	56105.89113	05/22/2012	1500	6	4025-5936	1.10	40	4477-4705	2.8
	56106.80105	06/27/2012	1500	6	4055-5965	1.10	80	4477-4705	1.3
	56106.823	06/28/2012	1500	6	4036-5950	1.10	-	4477-4705	2.6
	56108.9251	06/28/2012	1500	6	4036-5950	1.10	83	4477-4705	2.7
	56108.91805	06/30/2012	60	6	5722-7565	1.06	25	6064-6372 & 6736-7050	2.4
	56109.81434	07/01/2012	1800	6	5722-7565	1.06	79	6064-6372 & 6736-7050	2.4
	56109.80479	07/01/2012	30	6	5722-7566	1.06	-	6064-6372 & 6736-7050	2.5
	56111.03099	07/01/2012	1500	6	5722-7567	1.06	53	4477-4705 & 5050-5500	2.5
Hen2-99	56068.82089	05/21/2012	1800	6	4025-5937	1.10	43	4500-5740	2.7
	56106.7442	06/28/2012	1800	6	4036-5947	1.10	45	4500-5740	2.7
	56107.74513	06/29/2012	1800	6	4036-5950	1.10	25	4500-5740	2.7
	56108.86666	06/30/2012	2400	6	5722-7565	1.06	29	6630-7300 & 6000-6490	2.5
	56109.7475	07/01/2012	2400	6	5721-7565	1.06	23	6630-7300 & 6000-6490	2.5
	56110.97645	07/02/2012	2400	6	4034-5948	1.10	38	4500-5740	2.6
	56111.82174	07/03/2012	860	6	4033-5947	1.10	25	4500-5740	2.7
Hen3-1333	56106.92787	06/28/2012	1200	6	4036-5947	1.10	61	4500-4720 / 4785-5420	2.6
	56108.10932	06/30/2012	1800	6	4032-5940	1.10	46	4500-4720 / 4785-5420	2.7
	56108.88771	06/30/2012	60	6	5722-7565	1.06	-	6000-6288 / 6734-7057	2.4
	56108.89933	06/30/2012	1800	6	5722-7566	1.06	28	6000-6288 / 6734-7057	2.4
	56108.89933	06/30/2012	1800	6	5722-7567	1.06	34	6000-6288 / 6734-7057	2.4
	56109.11611	07/01/2012	60	6	5722-7568	1.06	-	6000-6288 / 6734-7057	2.4
	56109.11735	07/01/2012	60	6	5722-7569	1.06	-	6000-6288 / 6734-7057	2.4
	56109.13193	07/01/2012	2400	6	5722-7570	1.06	50	6000-6288 / 6734-7057	2.4

	56109.86424	07/01/2012	30	6	5722-7571	1.06	-	6000-6288 / 6734-7057	2.4
	56109.8734	07/01/2012	1500	6	5722-7572	1.06	50	6000-6288 / 6734-7057	2.4
Table A.2 – (continued)									
	56109.98714	07/01/2012	30	6	4029-5948	1.10	10	4500-4720 / 4785-5420	2.7
	56109.99635	07/01/2012	1500	6	4035-5948	1.10	64	4500-4720 / 4785-5420	2.7
	56111.05714	07/03/2012	1500	6	4029-5948	1.10	89	4500-4720 / 4785-5420	2.6
M1-26	56064.00127	05/16/2012	300	4	4257-5115	0.49	39	4477-4800	1.3
	56064.07030	05/17/2012	1800	4	4257-5115	0.49	45	4477-4800	1.1
	56064.17349	05/17/2012	1500	4	4257-5115	0.49	48	4477-4800	1.3
	56065.01637	05/18/2012	900	4	4257-5115	0.49	24	4477-4800	1.3
	56068.94747	05/21/2012	1200	6	4026-5937	1.10	62	4477-4800	2.4
	56070.04148	05/23/2012	1500	6	4026-5937	1.10	35	4477-4800	2.9
NGC5315	56068.8487	05/21/2012	1500	6	4025-5939	1.10	30	4477-4705 & 5050-5500	2.7
	56068.85801	05/21/2012	10	6	4025-5939	1.10	-	4477-4705 & 5050-5500	2.7
	56106.77705	06/28/2012	1500	6	4036-5947	1.10	24	4477-4705 & 5050-5500	2.7
	56108.73527	06/30/2012	60	6	5722-7565	1.06	-	6000-6250 & 7241-7295	2.5
	56108.73649	06/30/2012	30	6	5722-7565	1.06	-	6000-6250 & 7241-7295	2.5
	56108.74957	06/30/2012	2100	6	5722-7565	1.06	32	6000-6250 & 7241-7295	2.5
	56109.76839	07/01/2012	30	6	4033-5944	1.10	-	4477-4705 & 5050-5500	2.7
	56109.78276	07/01/2012	2400	6	4033-5944	1.10	24	4477-4705 & 5050-5500	2.7
	56110.7738	07/02/2012	2400	6	4014-5929	1.10	23	4477-4705 & 5050-5500	2.7
PHR1134-52	56110.73243	06/28/2012	1800	6	4036-5948	1.10	37	4477-5400	2.7
	56107.70924	06/29/2012	1800	6	4036-5948	1.10	27	4477-5400	2.6
	56108.71313	06/30/2012	2400	6	5722-7565	1.06	40	6321-6536 & 6838-7055	2.5
	56109.69883	07/01/2012	60	6	5722-7565	1.06	-	6321-6536 & 6838-7055	2.4
	56109.71351	07/01/2012	2400	6	5722-7565	1.06	30	6321-6536 & 6838-7055	2.4
	56109.84384	07/01/2012	2400	6	5722-7565	1.06	15	6321-6536 & 6838-7055	2.6
	56110.72121	07/02/2012	90	6	4015-5927	1.10	-	4477-5400	2.7
	56110.7359	07/02/2012	2400	6	4015-5927	1.10	36	4477-5400	2.7
SwSt1	56106.00453	06/28/2012	60	6	4050-5966	1.10	-	4400-4800 & 4477-4705	2.7
	56106.01586	06/28/2012	1800	6	4050-5966	1.10	60	4400-4800 & 4477-4705	2.7
	56108.03572	06/30/2012	1200	6	4036-5948	1.10	34	4400-4800 & 4477-4705	2.7
	56109.0797	07/01/2012	30	6	5723-7558	1.06	-	-	2.4
	56109.09747	07/01/2012	1800	6	5723-7558	1.06	-	-	2.4
	56480.09556	07/07/2013	240	6	4050-5966	1.1	26	4400-4800 & 4477-4705	2.6
	56480.10446	07/07/2013	1200	6	4050-5966	1.1	69	4400-4800 & 4477-4705	2.6

	56481.95551	08/07/2013	2400	6	4050-5966	1.1	103	4400-4800 & 4477-4705	2.6

Bibliography

2013, National Institute of Standard and Technology (NIST), [Online; accessed in 2013]

Acker, A., Cuisinier, F., Stenholm, B., & Terzan, A. 1992a, A&A, 264, 217

Acker, A., Gesicki, K., Grosdidier, Y., & Durand, S. 2002, A&A, 384, 620

Acker, A., Gorny, S. K., & Cuisinier, F. 1996, A&A, 305, 944

Acker, A., Marcout, J., Ochsenbein, F., et al. 1992b, The Strasbourg-ESO Catalogue of Galactic Planetary Nebulae. Parts I, II.

Acker, A., & Neiner, C. 2003a, VizieR Online Data Catalog, 340, 30659

—. 2003b, A&A, 403, 659

Acker, A., & Ochsenbein, F. 1993, in IAU Symposium, Vol. 155, Planetary Nebulae, ed. R. Weinberger & A. Acker, 33

Balick, B. 2007, in Asymmetrical Planetary Nebulae IV, `http://www.astro.washington.edu/users/balick/PNIC/`

Balick, B., & Frank, A. 2002, ARA&A, 40, 439

Barniske, A., Hamann, W.-R., & Gräfener, G. 2006, in Astronomical Society of the Pacific Conference Series, Vol. 353, Stellar Evolution at Low Metallicity: Mass Loss, Explosions, Cosmology, ed. H. J. G. L. M. Lamers, N. Langer, T. Nugis, & K. Annuk, 243

Billings, D. E. 1966, A guide to the solar corona, New York: Academic Press, |c1966

Blöcker, T. 2001, Ap&SS, 275, 1

Boffin, H. M. J., Miszalski, B., Rauch, T., et al. 2012, Science, 338, 773

Bohannan, B., & Walborn, N. R. 1989, PASP, 101, 520

Bonanos, A. Z., Stanek, K. Z., Udalski, A., et al. 2004, ApJ, 611, L33

Bond, H. E. 2000, in Astronomical Society of the Pacific Conference Series, Vol. 199, Asymmetrical Planetary Nebulae II: From Origins to Microstructures, ed. J. H. Kastner, N. Soker, & S. Rappaport, 115

Bryce, M., Bains, I., López, J. A., & Redman, M. P. 2004, in Astronomical Society of the Pacific Conference Series, Vol. 313, Asymmetrical Planetary Nebulae III: Winds, Structure and the Thunderbird, ed. M. Meixner, J. H. Kastner, B. Balick, & N. Soker, 104

Carroll, B. W., & Ostlie, D. A. 2006, An introduction to modern astrophysics and cosmology

Chesneau, O., Collioud, A., De Marco, O., et al. 2006, A&A, 455, 1009

Chhetri, R., Ekers, R. D., Jones, P. A., & Ricci, R. 2013, MNRAS, 434, 956

Chomiuk, L., Chornock, R., Soderberg, A. M., et al. 2011, ApJ, 743, 114

Chu, Y.-H., Treffers, R. R., & Kwitter, K. B. 1983, ApJS, 53, 937

Ciardullo, R. 2012, Ap&SS, 341, 151

Ciardullo, R., & Bond, H. E. 1996, AJ, 111, 2332

Clayton, G. C., Sugerman, B. E. K., Stanford, S. A., et al. 2011, ApJ, 743, 44

Cliffe, J. A., Frank, A., Livio, M., & Jones, T. W. 1995, ApJ, 447, L49

Cohen, M., Barlow, M. J., Liu, X.-W., & Jones, A. F. 2002, MNRAS, 332, 879

Conti, P. S., & Massey, P. 1989, ApJ, 337, 251

Corradi, R. L. M., Sabin, L., Miszalski, B., et al. 2011, MNRAS, 410, 1349

Crowther, P. 2013, in Massive Stars: From alpha to Omega

Crowther, P. A. 1997, MNRAS, 290, L59

—. 2007, ARA&A, 45, 177

Crowther, P. A. 2008, in Astronomical Society of the Pacific Conference Series, Vol. 391, Hydrogen-Deficient Stars, ed. A. Werner & T. Rauch, 83

Crowther, P. A., Abbott, J. B., Hillier, D. J., & De Marco, O. 2003, in IAU Symposium, Vol. 209, Planetary Nebulae: Their Evolution and Role in the Universe, ed. S. Kwok, M. Dopita, & R. Sutherland, 243

Crowther, P. A., Bohannan, B., & Pasquali, A. 1998a, in Astronomical Society of the Pacific Conference Series, Vol. 131, Properties of Hot Luminous Stars, ed. I. Howarth, 38

Crowther, P. A., De Marco, O., & Barlow, M. J. 1998b, MNRAS, 296, 367

Crowther, P. A., Dessart, L., Hillier, D. J., Abbott, J. B., & Fullerton, A. W. 2002, A&A, 392, 653

Crowther, P. A., & Hadfield, L. J. 2006, A&A, 449, 711

Crowther, P. A., & Walborn, N. R. 2011, MNRAS, 416, 1311

Davis, P. J., Kolb, U., & Knigge, C. 2012, MNRAS, 419, 287

Dayal, A., Sahai, R., Watson, A. M., et al. 2000, AJ, 119, 315

De Marco, O. 2008, in Astronomical Society of the Pacific Conference Series, Vol. 391, Hydrogen-Deficient Stars, ed. A. Werner & T. Rauch, 209

De Marco, O. 2009, PASP, 121, 316

De Marco, O., Barlow, M. J., & Cohen, M. 2002, ApJ, 574, L83

De Marco, O., Bond, H. E., Harmer, D., & Fleming, A. J. 2004, ApJ, 602, L93

De Marco, O., & Crowther, P. A. 1998, MNRAS, 296, 419

De Marco, O., Crowther, P. A., Barlow, M. J., Clayton, G. C., & de Koter, A. 2001, MNRAS, 328, 527

De Marco, O., Hillwig, T. C., & Smith, A. J. 2008, AJ, 136, 323

De Marco, O., & Soker, N. 2002, PASP, 114, 602

Depew, K., Parker, Q. A., Miszalski, B., et al. 2011, MNRAS, 414, 2812

Dopita, M. A., Bell, J. F., Chu, Y.-H., & Lozinskaya, T. A. 1994, ApJS, 93, 455

Dougherty, S. M., & Williams, P. M. 2000, MNRAS, 319, 1005

Drew, J. E., Barlow, M. J., Unruh, Y. C., et al. 2004, MNRAS, 351, 206

Eichler, D., & Usov, V. 1993, ApJ, 402, 271

Feibelman, W. A. 1998, ApJ, 506, 773

Figer, D. F. 2005, Nature, 434, 192

Foellmi, C., Moffat, A. F. J., & Guerrero, M. A. 2003a, MNRAS, 338, 360

—. 2003b, MNRAS, 338, 1025

Frank, A. 2000, in Astronomical Society of the Pacific Conference Series, Vol. 199, Asymmetrical Planetary Nebulae II: From Origins to Microstructures, ed. J. H. Kastner, N. Soker, & S. Rappaport, 225

García-Rojas, J., Peña, M., Morisset, C., et al. 2013, A&A, 558, A122

García-Segura, G., Langer, N., Różyczka, M., & Franco, J. 1999, ApJ, 517, 767

Geier, S., Classen, L., & Heber, U. 2011, ApJ, 733, L13

Girard, P., Köppen, J., & Acker, A. 2007, A&A, 463, 265

Górny, S. K. 2008, in Astronomical Society of the Pacific Conference Series, Vol. 391, Hydrogen-Deficient Stars, ed. A. Werner & T. Rauch, 165

Górny, S. K., Chiappini, C., Stasińska, G., & Cuisinier, F. 2009, A&A, 500, 1089

Gorny, S. K., & Stasińska, G. 1995, VizieR Online Data Catalog, 330, 30893

Górny, S. K., Stasińska, G., Escudero, A. V., & Costa, R. D. D. 2004, A&A, 427, 231

Górny, S. K., & Tylenda, R. 2000, A&A, 362, 1008

Gosset, E., Nazé, Y., Sana, H., Rauw, G., & Vreux, J.-M. 2009, A&A, 508, 805

Grosdidier, Y., Acker, A., & Moffat, A. F. J. 2000, A&A, 364, 597

Guerrero, M. A. 2012, in IAU Symposium, Vol. 283, IAU Symposium, 204–210

Guerrero, M. A., & De Marco, O. 2013, A&A, 553, A126

Guerrero, M. A., & Miranda, L. F. 2012, A&A, 539, A47

Guerrero, M. A., Miranda, L. F., Riera, A., et al. 2008, ApJ, 683, 272

Hajduk, M., Zijlstra, A. A., & Gesicki, K. 2010, MNRAS, 406, 626

Hamann, W.-R., Koesterke, L., & Wessolowski, U. 1995, A&A, 299, 151

Herald, J. E., Hillier, D. J., & Schulte-Ladbeck, R. E. 2001, apj, 548, 932

Herwig, F. 2001, Ap&SS, 275, 15

—. 2005, ARA&A, 43, 435

Hillier, D. J., & Miller, D. L. 1998, ApJ, 496, 407

Huckvale, L., Prouse, B., Jones, D., et al. 2013, MNRAS, 434, 1505

Hutsemekers, D., & Surdej, J. 1985, A&A, 153, 245

Iben, Jr., I., & Livio, M. 1993, PASP, 105, 1373

Iben, Jr., I., & MacDonald, J. 1986, ApJ, 301, 164

Iben, Jr., I., & MacDonald, J. 1995, in Lecture Notes in Physics, Berlin Springer Verlag, Vol. 443, White Dwarfs, ed. D. Koester & K. Werner, 48

Ivanova, N., Justham, S., Avendano Nandez, J. L., & Lombardi, J. C. 2013, Science, 339, 433

Ivanova, N., & Podsiadlowski, P. 2003, in Astronomical Society of the Pacific Conference Series, Vol. 304, CNO in the Universe, ed. C. Charbonnel, D. Schaerer, & G. Meynet, 339

Joergens, V., Müller, A., & Reffert, S. 2010, A&A, 521, A24

Jones, D., Tyndall, A. A., Huckvale, L., Prouse, B., & Lloyd, M. 2011, in Astronomical Society of the Pacific Conference Series, Vol. 447, Evolution of Compact Binaries, ed. L. Schmidtobreick, M. R. Schreiber, & C. Tappert, 165

Kastner, J. H., Balick, B., Blackman, E. G., et al. 2003, ApJ, 591, L37

Kastner, J. H., Montez, Jr., R., Balick, B., et al. 2012, AJ, 144, 58

Kingsburgh, R. L., Barlow, M. J., & Storey, P. J. 1995, A&A, 295, 75

Koesterke, L. 2001, Ap&SS, 275, 41

Koesterke, L., & Hamann, W.-R. 1995, A&A, 299, 503

Koesterke, L., & Hamann, W.-R. 1997a, in IAU Symposium, Vol. 180, Planetary Nebulae, ed. H. J. Habing & H. J. G. L. M. Lamers, 114

—. 1997b, A&A, 320, 91

Kohoutek, L., & Martin, W. 1981, A&A, 94, 365

Kurtz, M. J., & Mink, D. J. 1998, PASP, 110, 934

Lagadec, E., Chesneau, O., Matsuura, M., et al. 2005, in American Institute of Physics Conference Series, Vol. 804, Planetary Nebulae as Astronomical Tools, ed. R. Szczerba, G. Stasińska, & S. K. Gorny, 210–210

Lau, H. H. B., De Marco, O., & Liu, X.-W. 2011, MNRAS, 410, 1870

Lawlor, T. M., & MacDonald, J. 2002, in Astronomical Society of the Pacific Conference Series, Vol. 279, Exotic Stars as Challenges to Evolution, ed. C. A. Tout & W. van Hamme, 193

Leitherer, C., Chapman, J. M., & Koribalski, B. 1997, ApJ, 481, 898

Leuenhagen, U. 1997, in IAU Symposium, Vol. 180, Planetary Nebulae, ed. H. J. Habing & H. J. G. L. M. Lamers, 118

Leuenhagen, U., Hamann, W.-R., & Jeffery, C. S. 1996, A&A, 312, 167

Lopez, J. A., Steffen, W., & Meaburn, J. 1997, ApJ, 485, 697

Méndez, R. H. 1989, in IAU Symposium, Vol. 131, Planetary Nebulae, ed. S. Torres-Peimbert, 261–272

Méndez, R. H., Forte, J. C., & López, R. H. 1986, RMxAA, 13, 119

Mendez, R. H., Herrero, A., & Manchado, A. 1990, A&A, 229, 152

Miller Bertolami, M. M., & Althaus, L. G. 2006, A&A, 454, 845

Miller Bertolami, M. M., Althaus, L. G., Olano, C., & Jiménez, N. 2011, MNRAS, 415, 1396

Miszalski, B., Acker, A., Moffat, A. F. J., Parker, Q. A., & Udalski, A. 2009a, A&A, 496, 813

Miszalski, B., Acker, A., Ochsenbein, F., & Parker, Q. A. 2012a, in IAU Symposium, Vol. 283, IAU Symposium, 442–443

Miszalski, B., Acker, A., Parker, Q. A., & Moffat, A. F. J. 2009b, A&A, 505, 249

Miszalski, B., Boffin, H. M. J., & Corradi, R. L. M. 2013, MNRAS, 428, L39

Miszalski, B., Corradi, R. L. M., Boffin, H. M. J., et al. 2011a, MNRAS, 413, 1264

Miszalski, B., Crowther, P. A., De Marco, O., et al. 2012b, MNRAS, 423, 934

Miszalski, B., Crowther, P. A., & Moffat, A. F. J. 2012c, Gemini Focus Newsletter, 44, 17

Miszalski, B., Jones, D., Rodríguez-Gil, P., et al. 2011b, A&A, 531, A158

Miszalski, B., Mikołajewska, J., Köppen, J., et al. 2011c, A&A, 528, A39

Mitchell, D. L., Pollacco, D., O'Brien, T. J., et al. 2007, MNRAS, 374, 1404

Moffat, A. F. J. 1982, in IAU Symposium, Vol. 99, Wolf-Rayet Stars: Observations, Physics, Evolution, ed. C. W. H. De Loore & A. J. Willis, 515–519

Moffat, A. F. J. 2008, in IAU Symposium, Vol. 250, IAU Symposium, ed. F. Bresolin, P. A. Crowther, & J. Puls, 119–132

Moffat, A. F. J., & Piirola, V. 1993, ApJ, 413, 724

Monteiro, H., Schwarz, H. E., Gruenwald, R., & Heathcote, S. 2004, ApJ, 609, 194

Montez, Jr., R., Kastner, J. H., De Marco, O., & Soker, N. 2005, ApJ, 635, 381

Morgan, D. H., Parker, Q. A., & Russeil, D. 2001, MNRAS, 322, 877

Nordhaus, J., & Blackman, E. G. 2006, MNRAS, 370, 2004

Osuna, P., Barbarisi, I., Salgado, J., & Arviset, C. 2005, in Astronomical Society of the Pacific Conference Series, Vol. 347, Astronomical Data Analysis Software and Systems XIV, ed. P. Shopbell, M. Britton, & R. Ebert, 198

Parker, Q. A., Phillipps, S., Pierce, M. J., et al. 2005, MNRAS, 362, 689

Peimbert, M., Peimbert, A., Ruiz, M. T., & Esteban, C. 2004, ApJS, 150, 431

Pena, M. 1994, in IUE Proposal, 4825

Pena, M. 1997, in HST Proposal, 7482

Phillips, J. P., & Reay, N. K. 1983, A&A, 117, 33

Pottasch, S. R., Beintema, D. A., Bernard Salas, J., Koornneef, J., & Feibelman, W. A. 2002, A&A, 393, 285

Pottasch, S. R., & Zijlstra, A. A. 1992, A&A, 256, 251

Prinja, R. K., Barlow, M. J., & Howarth, I. D. 1990a, ApJ, 361, 607

Prinja, R. K., Barlow, M. J., & Howarth, I. D. 1990b, in Astronomical Society of the Pacific Conference Series, Vol. 7, Properties of Hot Luminous Stars, ed. C. D. Garmany, 275–277

Raga, A. C., Esquivel, A., Velázquez, P. F., et al. 2009, ApJ, 707, L6

Raga, A. C., & Noriega-Crespo, A. 1993, RMxAA, 25, 149

Rebassa-Mansergas, A., Zorotovic, M., Schreiber, M. R., et al. 2012, MNRAS, 423, 320

Reindl, N., Rauch, T., Werner, K., & Kruk, J. W. 2013, in Astronomical Society of the Pacific Conference Series, Vol. 469, 18th European White Dwarf Workshop., ed. Krzesiń, J. ski, G. Stachowski, P. Moskalik, & K. Bajan, 143

Robert, C. 1992, PhD thesis, UNIVERSITE DE MONTREAL (CANADA).

Rosner, R., Alexakis, A., Young, Y.-N., Truran, J. W., & Hillebrandt, W. 2001, ApJ, 562, L177

Rudy, R. J. 1977, PhD thesis, Oregon Univ., Eugene.

Rudy, R. J., & Kemp, J. C. 1976, ApJ, 207, L125

Sabin, L., Vázquez, R., López, J. A., García-Díaz, M. T., & Ramos-Larios, G. 2012, RMxAA, 48, 165

Sahai, R., Morris, M. R., & Villar, G. G. 2011, AJ, 141, 134

Saio, H., & Jeffery, C. S. 2002, MNRAS, 333, 121

Sander, A., Hamann, W.-R., & Todt, H. 2012, A&A, 540, A144

Schoenberner, D. 1979, A&A, 79, 108

Smith, L. F. 1968, MNRAS, 138, 109

Smith, L. F., Shara, M. M., & Moffat, A. F. J. 1996, MNRAS, 281, 163

Smith, L. J., Crowther, P. A., & Prinja, R. K. 1994, A&A, 281, 833

Soker, N. 1996, ApJ, 469, 734

—. 2006, PASP, 118, 260

—. 2013, NewA, 18, 18

Soker, N., & Kastner, J. H. 2003a, ApJ, 592, 498

—. 2003b, ApJ, 583, 368

Soker, N., & Livio, M. 1994, ApJ, 421, 219

Sparks, W. M., & Stecher, T. P. 1974, ApJ, 188, 149

St-Louis, N. 2013, ApJ, 777, 9

St.-Louis, N., Drissen, L., Moffat, A. F. J., Bastien, P., & Tapia, S. 1987, ApJ, 322, 870

Stevens, I. R., Blondin, J. M., & Pollock, A. M. T. 1992, ApJ, 386, 265

Stock, D. J., & Barlow, M. J. 2010, MNRAS, 409, 1429

Tocknell, J., De Marco, O., & Wardle, M. 2013, ArXiv e-prints

Todt, H., Gräfener, G., & Hamann, W.-R. 2006, in IAU Symposium, Vol. 234, Planetary Nebulae in our Galaxy and Beyond, ed. M. J. Barlow & R. H. Méndez, 127–130

Todt, H., Peña, M., Hamann, W.-R., & Gräfener, G. 2010, A&A, 515, A83

Todt, H., Kniazev, A. Y., Gvaramadze, V. V., et al. 2013, MNRAS, 430, 2302

Tonry, J., & Davis, M. 1979, AJ, 84, 1511

Trumpler, R. J., & Weaver, H. F. 1953, Statistical astronomy

Tuthill, P. G., Monnier, J. D., & Danchi, W. C. 1999, Nature, 398, 487

Tuthill, P. G., Monnier, J. D., Lawrance, N., et al. 2008, ApJ, 675, 698

Usov, V. V. 1991, MNRAS, 252, 49

van Altena, W. F., Lee, J. T., & Hoffleit, E. D. 1995, The general catalogue of trigonometric [stellar] parallaxes

van der Hucht, K. A., Conti, P. S., Lundstrom, I., & Stenholm, B. 1981, Space Sci. Rev., 28, 227

van Dokkum, P. G. 2001, PASP, 113, 1420

Vorontsov-Veliaminov, B. A., Kostiakova, E. B., Dokuchaeva, O. D., & Arkhipova, V. P. 1975, Soviet Ast., 19, 163

Werner, K., & Herwig, F. 2006, PASP, 118, 183

Werner, K., & Koesterke, L. 1992, in Lecture Notes in Physics, Berlin Springer Verlag, Vol. 401, The Atmospheres of Early-Type Stars, ed. U. Heber & C. S. Jeffery, 288

Williams, P. M. 1995, in IAU Symposium, Vol. 163, Wolf-Rayet Stars: Binaries; Colliding Winds; Evolution, ed. K. A. van der Hucht & P. M. Williams, 335

Williams, P. M., van der Hucht, K. A., Pollock, A. M. T., et al. 1990a, MNRAS, 243, 662

Williams, P. M., van der Hucht, K. A., The, P. S., & Bouchet, P. 1990b, MNRAS, 247, 18P

Wilson, R. E. 1979, ApJ, 234, 1054

Zhang, X., & Jeffery, C. S. 2012, MNRAS, 426, L81